

77 10418
CR 111101

J-910900-2

Experimental Investigations of
Simulated-Fuel Containment in
R-F Heated and Unheated
Two-Component Vortexes

NASA Contract No. SNPC-70



**CASE FILE
COPY**

United Aircraft Research Laboratories

EAST HARTFORD, CONNECTICUT

United Aircraft Research Laboratories



EAST HARTFORD, CONNECTICUT

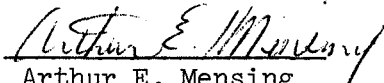
J-910900-2

Experimental Investigations of
Simulated-Fuel Containment in
R-F Heated and Unheated
Two-Component Vortexes

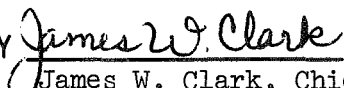
NASA Contract No. SNPC-70

REPORTED BY


Jerome F. Jaminet


Arthur E. Mensing

APPROVED BY


James W. Clark, Chief
Fluid and Systems Dynamics

DATE September 1970

NO. OF PAGES 108

COPY NO. 28

FOREWORD

An exploratory experimental and theoretical investigation of gaseous nuclear rocket technology is being conducted by the United Aircraft Research Laboratories under Contract SNPC-70 with the joint AEC-NASA Space Nuclear Propulsion Office. The Technical Supervisor of the Contract for NASA is Captain C. E. Franklin (USAF). Results of portions of the investigation conducted during the period between September 16, 1969 and September 15, 1970 are described in the following eight reports (including the present report) which comprise the required first Interim Summary Technical Report under the Contract:

1. Klein, J. F. and W. C. Roman: Results of Experiments to Simulate Radiant Heating of Propellant in a Nuclear Light Bulb Engine Using a D-C Arc Radiant Energy Source. United Aircraft Research Laboratories Report J-910900-1, September 1970.
2. Jaminet, J. F. and A. E. Mensing: Experimental Investigation of Simulated-Fuel Containment in R-F Heated and Unheated Two-Component Vortexes. United Aircraft Research Laboratories Report J-910900-2, September 1970. (present report)
3. Vogt, P. G.: Development and Tests of Small Fused Silica Models of Transparent Walls for the Nuclear Light Bulb Engine. United Aircraft Research Laboratories Report J-910900-3, September 1970.
4. Roman, W. C.: Experimental Investigation of a High-Intensity R-F Radiant Energy Source to Simulate the Thermal Environment in a Nuclear Light Bulb Engine. United Aircraft Research Laboratories Report J-910900-4, September 1970.
5. Bauer, H. E., R. J. Rodgers and T. S. Latham: Analytical Studies of Start-Up and Dynamic Response Characteristics of the Nuclear Light Bulb Engine. United Aircraft Research Laboratories Report J-910900-5, September 1970.
6. Latham, T. S. and H. E. Bauer: Analytical Studies of In-Reactor Tests of a Nuclear Light Bulb Unit Cell. United Aircraft Research Laboratories Report J-910900-6, September 1970.
7. Palma, G. E. and R. M. Gagosz: Optical Absorption in Transparent Materials During 1.5 Mev Electron Irradiation. United Aircraft Research Laboratories Report J-990929-1, September 1970.
8. Krascella, N. L.: Analytical Study of the Spectral Radiant Flux Emitted from the Fuel Region of a Nuclear Light Bulb Engine. United Aircraft Research Laboratories Report J-910904-1, September 1970.

Report J-910900-2

Experimental Investigations of Simulated-Fuel Containment
in R-F Heated and Unheated Two-Component Vortexes

TABLE OF CONTENTS

	<u>Page</u>
SUMMARY	1
RESULTS AND CONCLUSIONS	3
INTRODUCTION.	5
TEST EQUIPMENT AND PROCEDURES	6
Heated Vortex Tests.	6
Unheated Vortex Tests with 10-in.-Dia Vortex Tube.	9
Unheated Vortex Tests with 1.26-in.-Dia Vortex Tube.	14
DISCUSSION OF RESULTS	16
Heated Vortex Tests.	16
Unheated Vortex Tests with 10-in.-Dia Vortex Tube.	22
Unheated Vortex Tests with 1.26-in.-Dia Vortex Tube.	27
Comparison of Vortex Containment Experiments	28
REFERENCES.	32
LIST OF SYMBOLS	35
APPENDIX A - CALIBRATION AND USE OF OPTICAL SYSTEM FOR DETERMINATION OF PLASMA TEMPERATURE AND XENON PARTIAL PRESSURE.	40
APPENDIX B - DETERMINATION OF BROMINE ABSORPTION CONSTANTS.	44
APPENDIX C - NONSTEADY-STATE TESTS WITH 10-IN.-DIA VORTEX TUBE.	47

TABLE OF CONTENTS (Continued)

	<u>Page</u>
APPENDIX D - TESTS OF VORTEX-TUBE CONFIGURATION WITH REFLECTING PERIPHERAL WALL	55
TABLES	56
FIGURES	64

Report J-910900-2

Experimental Investigations of Simulated-Fuel Containment in R-F Heated and Unheated Two-Component Vortexes

SUMMARY

Experiments were conducted to determine the containment characteristics of radial-inflow vortexes for application to the nuclear light bulb engine. In these investigations, the amount of simulated fuel contained in two-component vortexes was measured for both heated and unheated (isothermal) vortex flows.

In the vortex flows with heat addition, power was added to the flow by r-f induction heating of the gas within 1.26-in.-dia by 2.8- or 3.5-in.-long chambers. The simulated buffer gas, argon, was injected in a tangential (circumferential) direction either from the end walls or from the peripheral wall. The flow rate, plasma diameter, and power addition were such as to provide radial gradients of temperature of approximately 70,000 deg R/in. (15,000 deg K/cm) near the outer edge of the plasma. Xenon was employed as the simulated fuel and was injected into the vortex at several different locations. Spectroscopic techniques were used to determine the temperature distributions and the simulated-fuel partial pressures within the plasma.

Most of the tests conducted with unheated vortex flows employed a 10.0-in.-dia by 30.0-in.-long vortex tube. This vortex tube was much larger than, but was approximately similar to, the vortex tube used in the heated tests. Air or sulfur hexafluoride was used as the simulated buffer gas and mixtures of iodine with helium and iodine with nitrogen were used as simulated fuels. Several different simulated-fuel injection configurations were used, and the injection velocity of the simulated fuel was varied. In most of the tests, axial bypass flow was withdrawn through ports located around the periphery at each end of the vortex tube.

Additional tests were conducted with unheated vortex flows employing the same small vortex tube used in the heated tests. Argon was used as the simulated buffer gas and a mixture of argon and bromine was used as the simulated fuel. These tests were conducted using simulated-fuel injection configurations and flow conditions similar to those used in the heated tests and in the previously mentioned unheated

tests in the 10-in.-dia vortex tube. In most of the tests, axial bypass flow was withdrawn through an annulus located at the peripheral wall at each end of the vortex tube. For all of the unheated tests, the volume-averaged partial pressures of the simulated fuel within the vortexes were determined, as were the radial distributions of the simulated-fuel partial pressures.

Comparisons were made of the simulated-fuel partial pressures in the heated and unheated flows. For the same geometries and the same buffer-gas weight flows, the heated vortexes had larger values of local simulated-fuel partial pressure in the central regions of the vortex, but lower values near the peripheral wall. For the same flow conditions and geometries, the volume-averaged simulated-fuel partial pressures were also greater in heated tests than in unheated tests. Measurements also indicated that radial gradients of static pressure in the high-temperature region of heated vortexes were much less than in unheated vortexes having the same flow rates.

Supporting research included isothermal tests in which the amount of simulated fuel stored in the vortex was measured during transient conditions. R-F plasma tests in which a reflecting peripheral wall was used to increase the local radiant energy flux were also conducted.

RESULTS AND CONCLUSIONS

Experiments were conducted to determine the amount and distribution of simulated fuel contained within radial-inflow vortexes. Tests were conducted with a 10-in.-dia unheated (isothermal) vortex, a 1.26-in.-dia unheated (isothermal) vortex, and a 1.26-in.-dia heated vortex. The length-to-diameter ratios of the vortex tubes ranged from 2.2 to 3.0. In the heated tests, energy was added to the central region of the vortex by means of r-f induction heating and resulted in gas temperatures of approximately 17,000 R occurring within approximately 50 percent of the vortex volume (plasma region). The temperature gradient present at the edge of the plasma region was approximately 70,000 deg R/in. The primary results of the fuel-containment tests are:

1. In unheated tests in the 10-in.-dia vortex, a volume-averaged simulated-fuel partial pressure ratio greater than 0.25 (approximate minimum for the nuclear light bulb reference engine) was obtained with end-wall simulated-fuel injection. For this test, the ratio of the peak simulated-fuel partial pressure to the simulated-fuel partial pressure at the peripheral wall of the vortex tube was approximately 30. Corresponding values in the 1.26-in.-dia heated vortex were 0.08 and 3000, respectively.

2. In the unheated tests, both the volume-averaged simulated-fuel partial pressure and the radial distribution of simulated fuel are affected by changes in the simulated-fuel-to-buffer injection velocity ratio, the location of the simulated-fuel injection, and the bypass ratio of the buffer gas.

- a. Decreasing the injection velocity ratio (fuel-to-buffer) from 1.2 to 0.2 increased the volume-averaged simulated-fuel partial pressure ratio from 0.13 to 0.19 (46 percent) when the simulated fuel was injected from the end wall at $r/r_1 = 0.8$.

- b. Simulated-fuel injection from the peripheral wall and from the end wall at $r/r_1 = 0.8$ resulted in higher volume-averaged simulated-fuel partial pressures, but more simulated fuel near the peripheral wall, than did injection from the centerline or from the end wall at $r/r_1 = 0.5$.

- c. Increasing the buffer-gas bypass flow from 0 percent to a maximum of 96 percent resulted in about a twofold increase in volume-averaged simulated-fuel partial pressure for peripheral-wall and end-wall ($r/r_1 = 0.8$) simulated-fuel injection and a tenfold increase in volume-averaged simulated-fuel partial pressure for centerline and end-wall ($r/r_1 = 0.5$) simulated-fuel injection. However, this increased bypass flow also resulted in approximately a fivefold increase in the amount of simulated fuel present at the peripheral wall with all four injection methods.

3. Unheated tests in the 10-in.-dia and 1.26-in.-dia vortex tubes resulted in similar simulated-fuel radial distributions for similar test conditions, except when the simulated fuel was injected at the centerline. Centerline injection in the small vortex tube resulted in a volume-averaged simulated-fuel partial pressure ratio approximately 20 times that of the large vortex tube for similar flow conditions.

4. Unheated tests with a positive radial density variation ($d\rho/dr \geq 0$) using a buffer gas approximately 32 times heavier than the simulated fuel resulted in an average simulated-fuel partial pressure approximately twice that obtained with constant density throughout the vortex flow under the same test conditions. The amount of simulated fuel present at the peripheral wall was unchanged.

5. Simulated-fuel injection configurations (such as from the peripheral wall and from the end wall) which resulted in the greatest volume-averaged simulated-fuel partial pressure in unheated tests could not be employed successfully in heated tests. With end-wall simulated-fuel injection the simulated fuel could not be made to enter the plasma, while with peripheral-wall simulated-fuel injection, the plasma could not be confined away from the peripheral wall.

6. In heated tests, the method for injecting the buffer gas (either from the end wall or from the peripheral wall) resulted in no significant difference in the simulated-fuel containment.

7. Heated tests in which the simulated fuel had a lower ionization potential than the buffer gas resulted in energy being deposited only in the region of the vortex containing the simulated fuel.

8. In heated tests, the presence of a low-ionization-potential simulated fuel in the plasma region resulted in a decrease of approximately 15 percent in local temperature and approximately 40 percent in the plasma impedance.

9. Heated tests using a 1.0-percent mixture of tungsten hexafluoride in argon as a simulated fuel resulted in deposition of particles on the peripheral wall. This is apparently due to centrifuging of the small particles as a result of the high tangential velocities in the 1.26-in.-dia vortex tube.

10. Volume-averaged simulated-fuel partial pressures were about three times greater in a heated test than in an unheated test when these tests were conducted in the same vortex tube with the same flow conditions.

INTRODUCTION

An experimental and theoretical investigation of gaseous nuclear rocket technology is being conducted by the United Aircraft Research Laboratories under Contract SNPC-70 administered by the joint AEC-NASA Space Nuclear Propulsion Office. The research performed under this contract is primarily applicable to the vortex-stabilized nuclear light bulb rocket concept described in Ref. 1 and illustrated in Fig. 1(a). In this concept, hydrogen propellant seeded with a small amount of tungsten particles is heated by thermal radiation passing through an internally cooled transparent wall located between gaseous uranium fuel and the propellant. A transparent buffer gas (neon) is injected circumferentially at the inner surface of the transparent wall to establish a vortex flow which is utilized to isolate the gaseous nuclear fuel from the transparent wall. An operational nuclear light bulb engine would consist of a number of unit cavities similar to that shown in Figs. 1(a) and 1(b).

A requirement for the operation of any gaseous nuclear rocket is the containment of sufficient nuclear fuel to maintain criticality. In the case of the nuclear light bulb, an additional requirement is that little or no fuel reach the transparent wall since this would cause the wall to lose transparency.

A number of experimental investigations have been conducted to determine the containment characteristics of two-component gas vortexes (e.g., Refs. 2 through 6). In these investigations, a light buffer gas was used to drive the vortex and a heavy simulated fuel was injected separately to simulate gaseous nuclear fuel. Most of the previous two-component gas tests were conducted with vortex flows in which no temperature gradient was present.

The experiments conducted in the present investigations had two primary purposes: (1) to determine the configurations and flow conditions necessary to obtain a desired high volume-averaged fuel partial pressure with as little simulated fuel as possible near the peripheral wall in both heated and unheated vortex flows, and (2) to compare similarities and differences obtained in the results of heated and unheated experiments and the results of tests with different-sized vortex tubes. To facilitate these comparisons, two vortex tube sizes were employed, a 1.26-in.-ID tube for both heated and unheated (isothermal) tests, and a 10-in.-ID tube for unheated (isothermal) tests (shown in Figs. 1(c) and 1(d), respectively).

The main body of this report describes the equipment used and results obtained in heated and unheated vortex tests. Four appendixes are also included in this report. Appendixes A and B contain information on the optical measurement techniques employed. Appendix C describes some experimental results obtained in nonsteady-state tests of an unheated vortex flow. In Appendix D, some results obtained with a reflecting wall located around an r-f heated plasma discharge are presented.

TEST EQUIPMENT AND PROCEDURES

The two-component vortex tests in this program employed two different facilities. The heated tests were conducted using the UARL 80-kw r-f induction heater while most of the unheated vortex tests were conducted using the high Reynolds number test facility constructed at UARL under Contract NASw-847. Several additional unheated tests were made using the same vortex tube as in the heated tests (no test facility required).

Heated Vortex Tests

In the two-component heated vortex tests, power was added to the gas within the vortex by r-f induction heating. The UARL 80-kw r-f induction heater described in Refs. 7 and 8 was used in these tests. In this heater, the output of the 80-kw power amplifier is connected to a 2 1/2-turn, 2.7-in.-dia work coil through a pi-coupling network. The coil turns are spaced approximately 1.0 in. apart and the vortex chamber assembly is installed within the work coil. The operating frequency of the heater for these tests was approximately 7.25 MHz and the power deposited in the plasma ranged from 7.2 to 12.5 kw.

Buffer-Gas Injection Systems

Two vortex tubes employing different buffer-gas injection geometries (Fig. 2) were used in the tests. These vortex tubes were the same as those described in Ref. 7.

The vortex tube shown in Fig. 2(a) employed end-wall buffer-gas injection. The buffer gas (argon) was injected in a tangential direction through eight injectors, four located on each end wall. The injectors consisted of 0.044-in.-ID by 0.062-in.-OD (1.1-mm-ID by 1.5-mm-OD) stainless steel tubing soldered to the end wall at a radius of 0.5 in. With this buffer-gas injection system, the end walls were spaced 2.8 in. apart. The buffer-gas injection area for this configuration was 0.012 sq in. and the scaling parameter, $dL/A_{B,j}$, had a value of 295 (see later discussion).

The second vortex tube, shown in Fig. 2(b), employed peripheral-wall buffer-gas injection. With this system, the buffer gas (also argon) was injected through two rows of 0.013-in.-dia holes, 65 holes in each row. The holes were drilled in copper injector assemblies mounted on the fused silica tube that formed the peripheral wall of the vortex tube. Slots were cut out of the fused silica tube so that the injector assemblies and fused silica tube formed a smooth surface (see Fig. 2(b)). The

injector assemblies were fixed to the fused silica tube with a silicone rubber adhesive sealant to provide a leak-proof seal. The buffer gas was injected at an angle of about 20 deg to the tangent of the inner surface. The same end walls discussed previously were used, but the end-wall injectors were removed to provide smooth end-wall surfaces. The end walls were spaced 3.5 in. apart (see Fig. 2(b)) to prevent arcing from the injector assemblies to the end walls. For this system, the buffer-gas injection area was 0.0172 sq in. and the scaling parameter, $dL/A_{B,j}$, was 255.

Simulated-Fuel Injection Systems

For most tests, the simulated fuel was injected directly into the plasma region through two injectors located on the vortex centerline (see Fig. 2). The injectors consisted of two 0.18-in.-OD tubes having 0.066-in.-ID ports at the center. The large difference between the injector inner and outer diameters was necessary to provide space for water cooling passages in the injectors. The injectors protruded through the end-wall thru-flow ports into the vortex a distance of approximately 0.38 in. Xenon was chosen as the simulated fuel because it has a high molecular weight and can be detected by spectroscopic techniques in a plasma that consists primarily of argon.

A few tests were conducted with simulated-fuel injection through the peripheral wall of the vortex. In these tests, four 0.04-in.-dia fused silica ducts were fused into the peripheral wall. The flow of simulated fuel was directed radially inward. This configuration was designed to inject the simulated fuel at a velocity approximately 0.2 times the buffer-gas injection velocity -- a combination of geometry and velocity ratio that had provided improved simulated-fuel containment in unheated tests.

One test was also made in which the simulated fuel was mixed with the buffer gas far upstream of the buffer-gas injection location. This injection method was employed to determine the value of the calibration constant used in the data reduction.

For all tests, both the xenon and argon flow rates were measured using calibrated flowmeters. The xenon and argon weight flow rates and injection velocities used in the tests are listed in Table I; the r-f power conditions are also listed.

Optical Equipment

Spectroscopic techniques were used to obtain the necessary measurements from which both the plasma temperature and the xenon partial pressure within the plasma could be determined. The optical system was identical to that previously described in Ref. 7. The major difference between the system employed in this study and that of Ref. 7 was that the output signal of the photomultiplier was fed through an amplifier into a strip chart recorder instead of into a visicorder. The strip chart recorder does not have the rapid response of the visicorder, but does provide much better traces than the visicorder.

Xenon Reclamation System

Due to the large flow rates of xenon employed, it was necessary for economic reasons to separate the xenon from the argon and reuse the xenon. A cold trap was designed and built to freeze the xenon and allow the gaseous argon to flow through the cold trap. A schematic diagram of the cold trap system is shown in Fig. 3. The argon-xenon mixture flowed into the first of two coils, each immersed in liquid argon. The first coil consisted of 0.375-in.-OD by 0.305-in.-ID copper tubing and was designed to remove most of the xenon from the mixture. The temperature of the gas leaving this coil was approximately -175 C. The flow then entered the second coil (0.250-in.-OD by 0.180-in.-ID copper tubing) and the remaining xenon was removed from the mixture. The larger diameter of the first coil was necessary to prevent solid xenon from plugging the coil, whereas the smaller diameter of the second coil allowed the xenon temperature to be lowered to -185 C (1 deg above the liquid argon temperature). The vapor pressure of xenon at -185 C is approximately 0.1 mm Hg.

Following a test, the coils were evacuated to a pressure of approximately 5 mm Hg and the entrance and exit valves were closed. The valve leading to the xenon storage cylinder was opened and the two coils removed from the liquid argon. As the coil temperature rose, the condensed xenon vaporized and the pressure within the coil increased. The xenon storage cylinder was immersed in liquid argon and the xenon within the coils was cryopumped into the xenon storage cylinder. When the pressure in the coils was reduced to less than 0.1 atm, the valve on the xenon storage cylinder was closed and the cylinder removed from the liquid argon. As the cylinder came to ambient temperature, the vaporized xenon increased the pressure in the cylinder to several hundred psi (depending upon the quantity of xenon in the cylinder). Approximately 90 to 95 percent of the xenon was recovered in the cold trap, and the purity of the recovered xenon was greater than 98 percent.

Test Procedures

Basically the same procedures as described in Ref. 7 were used in the tests reported herein. A low pressure (approximately 5 mm Hg) plasma was initiated, and the r-f power, vortex pressure, and argon flow rate were increased simultaneously. Xenon was injected after the desired operating conditions were established in a pure argon plasma. Spectral emission data were obtained by scanning the monochromator across the plasma image at the four axial stations indicated in Fig. 2 (the exact locations of these stations varied slightly from test to test).

For each of the test conditions listed in Table I, total radiation measurements, heat balance measurements, and spectral emission measurements were made. The total radiation measurements were made with a Reeder RBL-500 thermopile having a quartz window. The heat balance measurements were made by measuring the temperature rises and flow rates of the water used to cool the end walls, the injection probe, and the fused silica peripheral wall. Spectral emission data were obtained by traversing the monochromator across the plasma image at each of the four axial positions (see Fig. 2). Emission data of the following portions of the spectra were obtained: (1) the ArI 6965 Å line, (2) the XeI 4671 Å line, and (3) the continuum at approximately 4660 Å. The reasons for choosing these particular portions of the spectrum and their use in determining the temperature and simulated-fuel (i.e., xenon) partial pressure are described in Appendix A.

Unheated Vortex Tests with 10-in.-Dia Vortex Tube

Most of the equipment employed in the present investigation was used in preceding work under Contract NASw-847 and has been described in detail in Refs. 2, 3, 4, and 7. The essential features of this equipment and recent modifications are discussed herein.

High Reynolds Number Test Facility

The flow system (see Fig. 4 of Ref. 7) of the high Reynolds number test facility consists of three parts: the buffer-gas supply system, the simulated-fuel supply system, and the test section. The buffer-gas supply system provides a metered weight flow of atmospheric air (or, with slight modification, any other gas) heated by a steam heat exchanger and electric heaters to approximately 300 F. This temperature is required to prevent condensation of the iodine vapor, a component of the simulated fuel. (The term "unheated", however, is used to differentiate these tests from the r-f heated tests in which energy was deposited directly in the vortex using the 80-kw r-f induction heater.)

A measured weight flow of simulated fuel heated to approximately 300 F is provided by the simulated-fuel supply system (see Fig. 4 of Ref. 7). The simulated fuel is a mixture of a carrier gas (usually nitrogen) and iodine vapor. The iodine vapor is used only in sufficient quantities (generally 5 to 30 percent by weight of the simulated fuel) to permit its detection by optical methods. The molecular weight of the simulated-fuel mixture may be substantially altered by changing the carrier gas. The desired carrier gas is supplied under pressure to the carrier gas heater, which consists of a coil of copper tubing in a 325 F oven. Some carrier gas is then bypassed through specially constructed iodine boilers located within the same oven. At 325 F the iodine boilers contain liquid iodine at a vapor pressure of 0.568 atm. The amount of gaseous iodine in the simulated fuel is controlled by varying the amount of carrier gas bypassed through the boilers. Measurement of the amount of iodine in the mixture is accomplished as the simulated fuel passes through the iodine inlet absorptometer or "light box" (discussed in a following section).

The test section in which the vortex tube is mounted (Fig. 4) consists of a 20-in.-ID by 30-in.-long cylindrical shell with end flanges. The buffer gas flows directly into a 4.5-in.-wide annular plenum that is created when the vortex tube is installed.

The flow is exhausted from the vortex tube by two means: bypass flow and thru-flow. A separate bypass flow system is installed in the plenum chamber at each end of the vortex tube. Each bypass flow system consists of a 0.43-in.-ID manifold connected to the vortex tube by 15 equally spaced 0.094-in.-ID tubes (see Fig. 5(a) of Ref. 7). The bypass flow is ducted through the test section end flange to flow-meters. Because the bypass tubes are located very close to the end walls, the resulting flow is approximately equivalent to the annular axial-bypass configuration used in previous investigations (Ref. 4).

Thru-flow is removed through 1-in.-dia ports at the centers of the end walls (Fig. 4) and is ducted to flow meters. Both bypass flow and thru-flow were exhausted through a common header to the laboratory vacuum system.

Vortex Tube and Flow Configurations

The 10-in.-ID by 30-in.-long directed-wall-jet vortex tube used in previous investigations (Refs. 2, 3, 4, and 7) was employed in these tests. Only peripheral-wall buffer-gas injection was used. Sketches of the peripheral-wall buffer-gas injection geometry are shown in Fig. 5 of Ref. 7. Up to 900 directed-wall-jet inserts (see Fig. 5(b) of Ref. 7) can be installed in the vortex tube. For the tests described herein, two axial rows of 28 inserts each, 180 deg apart, were used (see Fig. 5(a) of Ref. 7). The slot height of the inserts was 0.030 in. The total injection area, $A_{B,j}$, was 0.84 sq in. and the scaling parameter, $dL/A_{B,j}$, had a value of 357.

Four simulated-fuel injection configurations were utilized in these tests: peripheral-wall injection (directed radially inward), end-wall injection (directed axially) at two different radial locations ($r/r_1 = 0.8$ and $r/r_1 = 0.5$), and centerline injection (directed axially) at $r/r_1 = 0$. For all four simulated-fuel injection configurations, the injector tubes have a length-to-diameter ratio greater than 6. Sketches of the simulated-fuel injection configurations are presented in Figs. 4 and 5.

The peripheral-wall simulated-fuel injection configuration consists of a 0.43-in.-ID manifold connected to the vortex tube by 12 injector tubes (0.31-in.-ID) near the axial midplane of the vortex tube (see Fig. 4(a)). The injector tubes are located around the periphery of the vortex tube approximately as shown in Fig. 4(a) and are installed flush with the inner surface of the vortex tube. As shown in the sketch, these tubes were not equally spaced around the periphery due to the necessity of avoiding the existing electrical heaters and duct work in the plenum.

The two end-wall simulated-fuel injection configurations are identical except for radial location. End-wall injection configurations for $r/r_1 = 0.8$ and $r/r_1 = 0.5$ are shown in Figs. 5(a) and 5(b), respectively. Each configuration consisted of 8 injector tubes (0.43-in.-ID) installed flush with the inner surface of the end wall. The injector tubes were located symmetrically, two in each quadrant, as shown in Fig. 5.

For tests having centerline simulated-fuel injection, two injector tubes (0.43-in.-ID, 0.5-in.-OD) were installed at the center of the thru-flow ducts (see Fig. 4(b)). The injectors protruded slightly into the flow (1 in. from the inner surface of the end-walls).

Optical Absorption Measurement System

The density of the iodine in the inlet simulated-fuel mixture was determined by means of an iodine absorptometer or "light box" (see Fig. 4 of Ref. 7). This absorptometer measured the inlet iodine density by alternately sampling (30 times per sec) the intensity of a test light beam which passed through windows in the simulated-fuel inlet duct and a reference light beam which bypassed the inlet duct. The logarithm of the ratio of the two intensities is proportional to the average iodine density in the duct. A complete discussion of the absorption technique is presented in Appendix I of Ref. 5 and Appendix III of Ref. 4.

In addition to the inlet absorptometer, two other optical absorption systems were used to determine the containment of the simulated fuel within the vortex tube. As shown schematically in Fig. 8 of Ref. 7, these systems consisted of a scanning axial light beam, and a fixed centerline light beam.

The axial light-beam absorption system was used to determine the radial distribution of the simulated fuel as well as the amount of the simulated fuel contained in the vortex tube. The amount of light absorbed by the iodine at a given radius of the vortex tube is related to the axially-averaged iodine density (see Appendix I of Ref. 9). The average simulated-fuel density was calculated from the average iodine density by assuming that the iodine vapor and the carrier gas are fully mixed, and that the volume flow rate of the simulated-fuel mixture is equal to that of the iodine alone. Thus, the simulated-fuel density may be determined from the relation

$$\rho_F = \rho_I \frac{W_F}{W_I} \quad (1)$$

To determine the radial distribution of simulated fuel, a scanning light beam was traversed along the upper half of the vertical diameter of the vortex tube from $r/r_1 = 0.2$ to $r/r_1 = 1.0$. A second light beam was then traversed along the lower half of the vertical diameter in the same manner. The amount of iodine in the volume scanned by the light beam was determined by electronically integrating the logarithm of the light beam intensity during each traverse. The radial distribution and the amount of simulated fuel in the volume scanned was then calculated from these data. Further details of the absorptometer and a discussion of the principles of operation are presented in Appendix III of Ref. 4.

The amount of simulated fuel in the core volume not covered by the scanning light beam (i.e., $0 < r/r_1 < 0.2$) was measured using the centerline light-beam system which passes a fixed light beam along the axis of the vortex tube. Fiber optics are utilized as the source and receiver for this light beam (see Fig. 8 of Ref. 7). To avoid interference with the scanning light system, the centerline light beam was operated by a shutter which opened only during the time when the lower- and upper-traversing light beams were off. This system could not be used in tests employing the centerline simulated-fuel injection configuration.

Test and Data-Reduction Procedures

Tests to determine the amount of simulated fuel contained in the vortex were conducted in the following manner. For a given simulated-fuel and buffer-gas molecular weight, both the simulated-fuel and buffer-gas weight flow rates were set. After steady-state conditions were obtained, pressures, temperatures, and flow rates were measured. At the same time, a number of traverses (usually 5) of the scanning axial light beam were recorded, as were the outputs of the electronic integrators, centerline light beam, and inlet iodine absorptometer. Steady-state conditions were verified during this time by monitoring the recorders. The time required for a

complete scanning cycle was approximately 15 sec, which is several times the average residence time of the simulated fuel within the vortex tube. These procedures were repeated for each flow condition during a given series of tests. To provide the required baseline data on the optical systems, several reference test runs were conducted before and after each series of tests. Reference tests were made with both the buffer gas and carrier gas flowing, but with no iodine flow.

The total amount of simulated fuel contained in the vortex chamber was determined by averaging data obtained from upper and lower traverses of the scanning light beam. For most tests reported herein, the average value of simulated fuel stored differed from the value determined from the individual upper-or lower-traverse by less than 15 percent.

Steady-state isothermal vortex test series were conducted by varying the simulated-fuel injection velocity at four different flow conditions (four different bypass ratios) with a constant buffer-gas flow rate. The simulated-fuel injection velocity was varied by changing the number of simulated-fuel injection ports while maintaining a constant simulated-fuel flow rate. A series of these tests was conducted with each of the simulated-fuel injection configurations, except for the centerline injection configuration. With centerline simulated-fuel injection, tests were conducted at only one simulated-fuel injection velocity for each of the four flow conditions (bypass ratios) because the number of injection ports could not be varied.

In addition, some tests were conducted with two different buffer-gas and simulated-fuel molecular weights. In these tests, the buffer gases and mixtures used for the simulated fuel were, respectively: air ($m_B = 29$) and nitrogen/iodine ($m_F \approx 30$); and sulfur-hexafluoride ($m_B = 146$) and helium/iodine ($m_F \approx 6$).

For all of the tests described herein, the buffer-gas and simulated-fuel injection temperatures were constant at approximately 300 F and the static pressure in the vortex tube was between 0.9 and 1.0 atm. Equal amounts of thru-flow (and bypass flow) were removed from each end of the vortex tube. A summary of configurations and operating conditions used in isothermal tests in the 10-in.-dia vortex tube is presented in Tables II through V.

A small portion of the program was directed toward measurements of the transient behavior of vortices following changes in simulated-fuel flow rate and vortex-tube static pressure. The test and data reduction procedures, and the test results, are presented in Appendix C.

Unheated Vortex Tests with 1.26-in.-Dia Vortex Tube

Most of the equipment used in the unheated tests with the 1.26-in.-dia vortex tube is the same as that used in the heated vortex tests. The test equipment used and modifications required are described here.

Vortex Tube and Flow Configurations

The 1.26-in.-dia vortex tube used in the heated tests was also used for the unheated tests employing a bromine/argon mixture as the simulated fuel. Buffer-gas injection was from the peripheral wall (see Fig. 2(b)). The flow system employed is shown schematically in Fig. 6(a). A common argon supply provided both the buffer gas and the carrier gas, under pressure, to the vortex tube. The carrier gas could be bypassed through a teflon container partly filled with bromine. The bromine container and all test equipment were at room temperature (about 70 deg F). Since the vapor pressure of bromine at 70 F is 0.236 atm, no additional heating was necessary to provide the amount of bromine vapor required for optical detection in the simulated-fuel mixture.

The simulated fuel was injected using one of three methods: centerline injection, end-wall injection at $r/r_1 = 0.8$, and end-wall injection at $r/r_1 = 0.5$. The centerline injection configuration was identical to that used in heated tests and is shown in Fig. 2(b). The end-wall simulated-fuel injection configurations are shown in Fig. 6(b). At each radius ratio, four 0.040-in.-ID end-wall injectors are symmetrically located, one in each quadrant. The injectors are directed axially and located flush with the inner surface of the end walls. The end-wall injectors were located on only one end wall, and the two configurations shown in Fig. 6(b) were not used concurrently.

Provision for axial bypass flow through an annulus at each end of the vortex tube at the peripheral wall was incorporated in the test assembly (only one bypass flow exhaust is shown in Fig. 6(a)). The bypass flow and the thru-flow were connected to a common exhaust, through a bromine absorptometer, and were bubbled through an alkaline water solution to the atmosphere. The alkaline water solution removed the bromine from the exhaust mixture, preventing bromine pollution of the atmosphere.

Optical Absorption Measurement Systems

The density of the bromine within the vortex tube was also determined by optical absorption techniques. A light source (1000-w tungsten filament lamp) was located behind the horizontal vortex tube. The light from this source passed through the vortex tube chordwise onto the face of a monochromator. The entrance slit of the monochromator was 25 microns by 0.25 in. and was horizontal. The monochromator was

set at the wavelength at which bromine has maximum absorption, 4300 \AA (see Appendix B). The monochromator was scanned vertically across the image of the vortex tube at each of four axial positions (see Fig. 6(a) for scanning positions). The output of the monochromator photomultiplier tube was amplified and recorded giving a continuous trace of the light intensity transmitted chordwise through the vortex tube. Data were recorded both with (I) and without (I_0) bromine injection, and the ratio I/I_0 was determined as a function of chordal location. The radial distribution of partial pressure was then calculated from these data using the Abel inversion technique.

A bromine absorptometer, similar to the iodine absorptometer already discussed, was located in the common exhaust from the vortex tube. This absorptometer was necessary to determine the fraction of bromine in the simulated fuel from which the containment of simulated fuel in the vortex was determined. The absorptometer consisted of a 100-w, 6-v d-c light source, fiber optics, a photomultiplier tube and an interference filter with a transmission band (bandwidth of 40 \AA) centered at 4600 \AA . Light from the source was transmitted by the fiber optics through windows in the exhaust tube, through the interference filter, to the photomultiplier tube. A 4600 \AA interference filter was used since it was readily available and the light absorption of bromine at 4600 \AA is only 31.7 percent less than the maximum absorption at 4300 \AA (see Appendix B).

Test Procedures

A total of seven unheated test runs were conducted. Each test run consisted of eight chordal scans, two at each of the axial positions shown in Fig. 6(a). The first scan at each position was a reference scan with argon buffer gas flowing but no simulated fuel. The second scan at each position was conducted with simulated fuel injected. The simulated fuel consisted of bromine mixed with argon carrier gas. During each of these scans, the exhaust absorptometer data were recorded. The data obtained at each axial position were arithmetically averaged to produce one average radial-distribution per test run. Each average radial-distribution was then numerically integrated to give the volume-averaged simulated-fuel partial pressure. The method of calculating these simulated-fuel partial pressures is explained in Appendix B. A summary of configurations and operating conditions used for all isothermal tests in the 1.26-in.-ID vortex tube is presented in Table VI.

DISCUSSION OF RESULTS

The primary purpose of the heated and unheated (isothermal) tests was to determine the effects of several geometric and flow variables on the amount of simulated fuel stored and its radial distribution in two-component vortexes. In the heated tests, it was also of interest to determine if the confined plasma could be maintained when sufficient simulated fuel was present to provide the primary source of electrical conduction. The unheated tests were conducted to investigate the effects of simulated-fuel injection location and velocity and the effects of buffer-gas bypass flow on containment. The following three sections contain separate discussions of the results obtained in the heated and unheated vortex tests. The next section then discusses some comparisons between heated and isothermal vortex flows, and between vortex flows in different-sized vortex tubes.

Heated Vortex Tests

Tests with Argon Buffer Gas Only

Initial experiments were conducted with no simulated-fuel injection in the two vortex tubes shown in Fig. 2. The flow and power conditions employed in these tests are shown in columns 1 and 4 of Table I. The power deposited into the plasma region was less for the peripheral-wall injection configuration (see Fig. 2(b)) to avoid damage to the seal between the copper injectors and the fused silica tube located under the r-f coil and to prevent arcing between the injector and the end walls.

The chordal variation of the peak intensity of the ArI 6965 Å line was measured at each of the axial positions shown in Fig. 2 and was used to calculate the temperature distributions. The resultant radial distributions of temperature are presented in Fig. 7. The presence of an axial gradient of temperature in the plasma region is evident by comparing the temperatures near the axial midplane with those near the end walls. In Fig. 7(a), the complete radial temperature profile could not be obtained at the axial positions nearest the end walls because the simulated-fuel injection probes (see Fig. 2) blocked the emitted light (these probes were in position even though they were not used in this set of tests). This blockage did not occur in tests with the peripheral-wall buffer-gas injection configuration since the end walls were spaced farther apart (compare Fig. 2(a) and 2(b)). The lower temperatures obtained in tests with peripheral-wall buffer-gas injection (compare Figs. 7(a) and 7(b)) were the result of the lower power deposition for this injection configuration (9.6 kw, compared with 12.5 kw). The temperature distributions shown in Fig. 7 are typical of those of an r-f plasma; the peak temperature occurs off-axis, approximately midway between the center and edge of the plasma. The peak temperature

is between 200 and 400 K greater than the centerline temperature. The plasma region was confined well away from the peripheral wall of the vortex chamber. At the axial midplane, the plasma extended to approximately 70 percent of the vortex tube radius in tests with the end-wall injection configuration, and to approximately 60 percent of the tube radius in tests with the peripheral-wall injection configuration. The difference in diameter may be due to different buffer-gas flow rates or to the difference in power deposited. Both of these factors can influence the plasma diameter.

A test was conducted in which a reflecting surface was positioned in the water cooling annulus between the two fused silica tubes. The objective of this test was to demonstrate that a reflecting surface could be employed around an r-f heated plasma to increase the radiation flux at the vortex peripheral wall. This test is further described in Appendix D.

Tests with Buffer Gas and Simulated Fuel Premixed

A test was conducted employing the end-wall buffer-gas injection configuration (see Figs. 2(a)) in which the xenon was premixed with the argon prior to injection into the vortex chamber. The xenon and argon weight flow rates were measured; thus the xenon partial pressure within the vortex was known. This test was necessary to determine the relationship between the intensity of the XeI 4671 Å line and the xenon partial pressure. A similar test was described in Ref. 7; however, the additional calibration techniques and different readout equipment used made it advisable to repeat this test for the conditions of this study. The flow and power conditions for the new test are given in the second column of Table I.

Since the xenon and argon were premixed prior to injection, the xenon partial pressure within the vortex was assumed to remain at the premixed value, 0.0071 atm. It was assumed that no separation of the xenon and argon occurred within the vortex. Line intensity data were obtained at axial position $x/L = 0.32$. Measurements of the ArI 4300 Å line intensity were used to obtain the temperature distribution shown in Fig. 8(a). From the measured intensity of the XeI 4671 Å line, the radial distribution of temperature (from Fig. 8(a)), and the known xenon partial pressures, the constant relating the peak intensity to the xenon partial pressure was determined (see Appendix A for the method used). Ideally, the constant should be independent of radial position. However, determination of this constant at various radial positions resulted in the distribution shown in Fig. 8(b). The small variation in the central regions of the vortex is probably due to errors in making the measurements. An arithmetic average of the constant was computed (see Fig. 8(b)), and this average value was used in succeeding xenon tests.

Tests with Peripheral-Wall Simulated-Fuel Injection

A few tests were conducted with the simulated fuel (xenon) injected radially inward through four ducts located on the peripheral wall at the axial midplane. Attempts were made to inject the simulated fuel into the vortex at a low velocity (approximately 0.2 times the buffer-gas injection velocity), a technique that resulted in good simulated fuel containment in unheated tests (see following subsection). However, heated tests with this configuration were not successful because little or no xenon entered the plasma region under these test conditions. When higher xenon flow rates were used (greater than approximately 10 percent of the argon flow rate), the plasma region did not remain confined, but suddenly expanded and filled the entire vortex chamber. A possible explanation for this is that gas breakdown occurred near the peripheral wall of the vortex tube due to the presence of a relatively large amount of xenon which has a lower ionization potential than argon. The expanded plasma caused excessive heating of the peripheral wall. It was concluded that peripheral-wall simulated-fuel injection was not suitable for use in further heated vortex tests.

Tests with Simulated-Fuel Injection at the Vortex Centerline

Tests with Xenon as Simulated Fuel

Tests were conducted in which the simulated fuel (xenon) was injected into the plasma region through probes on the vortex centerline (see Fig. 2). Both the end-wall buffer-gas injection configuration and the peripheral-wall buffer-gas injection configuration were employed in these tests. Chordal measurements of the peak intensity (see Appendix A for definition of peak intensity) of the ArI 6965 Å line, the XeI 4671 Å line and the continuum at 4660 Å were made. The flow and power conditions are listed in the third and fifth columns of Table I.

In these tests, the xenon partial pressures were substantially greater than those described in Ref. 7 or in the premixed tests described previously. Because of this, the temperature of the gas could not be directly determined from the radial distribution of intensity of the ArI 6965 Å line since the argon partial pressure was unknown. An iteration method described in Appendix A was developed. The temperatures and simulated-fuel (xenon) partial pressures that resulted from these tests are presented in Figs. 9 and 10. Figure 9(a) shows the radial distribution of temperature at the four axial positions for the end-wall buffer-gas injection configuration (Fig. 2(a)). The data near the centerline region at axial positions $x/L = 0.07$ and 0.93 are incomplete due to blockage by the injector probes. Comparison of Figs. 9(a) and 7(a) shows that the injection of xenon caused a substantial decrease in the plasma temperature (approximately 15 percent or 1500 K) at all positions. However, the percent of power deposited that is radiated remains nearly the same -- approximately

25 percent with and without xenon injection (see Table I). Thus, the presence of the xenon obviously increased the radiative properties of the plasma. The reflected impedance of the plasma decreased approximately 40 percent with the presence of xenon even though the temperature decreased (in a one-component plasma, a decrease in temperature should result in an increased reflected impedance). The large decrease in temperature near the centerline of the plasma may be caused by the injection of the xenon near this region, or may be due to shielding of the central regions of the plasma by the increased conductivity at larger radii.

The radial variation of the xenon simulated-fuel partial pressure is presented in Fig. 9(b). The data are nondimensionalized by the vortex static pressure at the peripheral wall, P_1 (1.3 atm). The simulated-fuel partial pressure was assumed to be composed of three constituents: neutral xenon atoms, singly ionized xenon atoms (doubly ionized atoms are negligible), and electrons coming from the xenon. Electron pressure due to ionized argon is not included. Since the doubly ionized atoms are negligible, the electron pressure from the xenon is equal to the singly ionized xenon atom pressure. Thus, the partial pressure of the simulated fuel is

$$P_F = P_{Xe^0} + 2P_{Xe^+} \quad (2)$$

Simulated-fuel partial pressure ratios between 0.2 and 0.3 occurred within the central region of the plasma, and decreased near the plasma boundary. Included on Fig. 9(b) are the volume-averaged simulated-fuel partial pressure ratio, \bar{P}_F/P_1 , and the value of the partial pressure ratio that would occur if the simulated fuel had been premixed with the buffer gas, $\bar{P}_F/P_1|_{MIX}$. The volume-averaged simulated-fuel partial pressure ($\bar{P}_F/P_1 = 0.08$) is substantially lower than the peak local values, primarily because the plasma occupies less than 60 percent of the total chamber volume. If the volume-averaged simulated-fuel partial pressure had been based only on the volume of the plasma, \bar{P}_F/P_1 would be increased by approximately 70 percent to a value of 0.134. Gas samples were withdrawn from the peripheral wall at the axial midplane (see Fig. 2) and analyzed for xenon content. For the data presented in Fig. 9, the simulated-fuel peripheral-wall partial pressure ratio was 7.5×10^{-5} . Thus, the simulated-fuel partial pressure at the peripheral wall is approximately 1/3000 of the value at $r/r_1 = 0.5$, a radial distance of 0.32 in. from the peripheral wall.

Figure 10 presents the temperatures and simulated-fuel partial pressures for tests with the vortex configuration having peripheral-wall buffer-gas injection. Again, the presence of the xenon decreased the centerline temperature approximately 1500 K (compare Figs. 10(a) and 7(b)), while decreasing the reflected impedance.

The pronounced decrease in the temperature near the centerline at axial positions $x/L = 0.14$ and 0.86 may also be explained by the reasons cited above. The radial variations of the simulated-fuel partial pressure ratios (Fig. 10(b)) are similar to those of Fig. 9(b) except for a pronounced increase in the values near the injection probes (with this configuration the probes did not block the emitted light). Injection of xenon increased the diameter of the plasma about 30 percent (compare Figs. 10(a) and 7(b)). Also shown in Fig. 10(b) is the volume-averaged simulated-fuel partial pressure ratio (based on entire chamber volume) and the value of simulated-fuel partial pressures that would occur if the xenon and argon were completely mixed.

Wall samples taken at the peripheral wall at the axial midplane resulted in a simulated-fuel partial pressure ratio at the wall of 4.2×10^{-5} , again, more than three orders of magnitude smaller than the simulated fuel partial pressure 0.32 in. away from the wall (i.e., at $r/r_1 = 0.5$).

The values of the simulated-fuel partial pressures shown in Figs. 9(b) and 10(b) may be smaller than the actual values. As discussed in the section entitled TEST EQUIPMENT AND PROCEDURES, the intensity of the XeI 4671 \AA line was determined by setting the monochromator on the peak intensity and then scanning the monochromator across the plasma image. Because of the relatively high xenon flow rate it was necessary to minimize the time required for obtaining the data. Thus, recording the peak line intensities as a function of position appeared to be the most practical method for obtaining the desired data. However, for this procedure to be accurate, it must be assumed that the value of the peak intensity is directly proportional to the total line emission. In general, this is usually true since the measured half-width of emission lines is usually set by the broadening due to the monochromator. However, the XeI 4671 \AA line is very intense, and at xenon partial pressures on the order of 0.2 atm, some broadening of the line was observed (a few separate measurements were made of the line shape). The line half-width was approximately 25 percent greater at the large partial pressure. The usual changes of line broadening are due to pressure or self-absorption. However, it is not believed that the pressure was great enough to affect the line shape and there were no indications of self-absorption. Thus, the reasons for the apparent line broadening are unknown.

A significant feature of the tests in which xenon partial pressure exceeded approximately 0.1 atm is that the r-f energy is added primarily only to those regions where xenon is present. In Figs. 11 and 12, the variation with temperature of the composition of an xenon-argon mixture is shown for xenon mole fractions of 1 and 10 percent, respectively. These curves were obtained from calculations described in Ref. 10. At a mole fraction of 1 percent and at temperatures between 8000 and $10,000$ K, the electron partial pressure is approximately equally contributed to by argon and xenon (see Fig. 11). However, at a xenon mole fraction of 10 percent, the

argon contribution to the electron pressure is small. Hence, most of the electrons are being supplied by the xenon. Induction heating of a gas occurs only by addition of energy to electrons (the electrons then give up energy to the atoms by collisions). If the primary electron donor is the xenon (or simulated fuel), then r-f energy is added to the gas only in the "fuel region." The data presented in Figs. 9(b) and 10(b) show that the fuel region was confined away from the peripheral wall of the vortex chamber even though the fuel region created the electrons which permitted the energy addition. At the low simulated-fuel partial pressures reported in Ref. 7, the simulated fuel did not contribute appreciably to the electron pressure of the plasma region. Thus the data obtained in the present study not only shows that greater simulated-fuel partial pressures can be obtained, but also that good containment exists when the energy is added directly to the simulated fuel.

Tests with Tungsten Hexafluoride and Argon as Simulated Fuel

Tests using xenon as a simulated fuel resulted in small values of simulated-fuel partial pressure at the peripheral wall. Hence, it was considered desirable to test a simulated fuel that would condense if it reached the peripheral wall. A test was conducted using the end-wall buffer-gas injection configuration (see Fig. 2(a)) with centerline simulated-fuel injection and using a mixture of tungsten hexafluoride (WF_6) and argon as the simulated fuel. The mixture consisted of one percent WF_6 in argon. The argon weight flow rate was 7.5×10^{-4} lb/sec. This flow gave approximately the same volume flow rate as had been used in the tests with xenon as the simulated fuel. The buffer-gas flow conditions were the same as those listed in column 3 of Table I. The WF_6 flow rate for this test was 7.5×10^{-6} lb/sec. The presence of tungsten in the plasma was quite evident from spectral emission data.

After a 6-minute test period, the fused silica tube that formed the peripheral wall of the vortex tube was removed. A photograph of the tube after the test is shown in Fig. 13. Some tungsten was deposited on the peripheral wall. The tube was weighed, then washed and weighed again. It was determined that approximately 3.3×10^{-5} lb of tungsten was deposited on the fused silica tube. This represented 2 percent of the total injected tungsten. However, the tungsten deposit was easily washed from the tube indicating that it consisted of small particles and not plating such as would occur if tungsten vapor had been condensed on the fused silica tube. The fact that particles were deposited on the peripheral wall of the vortex is not surprising since the high tangential velocity (approximately 400 ft/sec) in a 1.26-in.-ID tube results in radial accelerations of approximately 10^5 g. For the gaseous part of the flow this radial acceleration is balanced by the radial pressure gradient. However, particles are centrifuged outward at a very rapid rate. Accelerations of this magnitude provide no chance for the particles to move axially to the thru-flow port prior to being centrifuged to the peripheral wall. The magnitude of radial accelerations encountered in these tests is much greater than

would exist in either a full-scale nuclear light bulb engine or in an in-reactor test. (It is estimated that the maximum radial acceleration in the reference nuclear light bulb engine is approximately 3 g.) Further tests employing a condensible vapor as a simulated fuel should not be conducted until the radial accelerations within the vortex are more like those which would exist in in-reactor or full-scale tests. To accomplish this, the injection velocities in the models employing r-f tests must be substantially reduced. Thus, the injection area must be substantially increased so that sufficient buffer-gas weight flow can be injected to maintain confinement of the plasma. It is also expected that larger vortex tube diameters and/or higher vortex pressures would be helpful in reducing the centrifuge effect.

Unheated Vortex Tests with 10-in.-Dia Vortex Tube

The unheated two-component vortex tests were conducted using two sizes of vortex tubes --- a 10-in.-ID and a 1.26-in.-ID vortex tube. These tests employed several different simulated-fuel injection configurations. Peripheral-wall buffer-gas injection was used in all tests. Tests were conducted at several bypass flow ratios and simulated-fuel injection velocities with approximately constant buffer-gas and simulated-fuel weight flow rates. The data from these tests are presented with the simulated-fuel partial pressure (either volume-averaged or local) considered as the primary dependent variable. The simulated-fuel partial pressure was non-dimensionalized by the static pressure at the peripheral wall of the vortex chamber.

Results of Tests Using Different Simulated-Fuel Injection Configurations

Several series of tests were conducted in the 10-in.-ID vortex tube with four different simulated-fuel injection configurations. The four configurations were: peripheral-wall injection, end-wall injection at $r/r_1 = 0.8$, end-wall injection at $r/r_1 = 0.5$, and centerline injection (see Figs. 4 and 5). Each simulated-fuel injection configuration was tested at four bypass flow ratios. At each bypass ratio and with each simulated-fuel injection configuration, except centerline injection, the simulated-fuel injection velocity was varied. With centerline injection, only one simulated-fuel injection velocity was employed since the number of injection ports could not be varied (to maintain the flow rate constant). In all tests, the buffer-gas flow rate and the simulated-fuel flow rate were maintained approximately constant. A summary of all flow conditions tested and configurations employed is presented in Tables II through V. The results obtained from these tests are presented in Figs. 14 through 23.

Tests with Peripheral-Wall Simulated-Fuel Injection

Results obtained from tests with peripheral-wall simulated-fuel injection are presented in Figs. 14 and 15. Figure 14 presents radial distributions of simulated-fuel partial pressure at 48 percent bypass for three fuel-to-buffer injection velocity ratios (v_F/v_j). The dashed lines indicate the volume-averaged simulated-fuel partial pressure, \bar{P}_F/P_1 , for each of the three tests shown. The solid line indicates the volume-averaged simulated-fuel partial pressure that would be obtained if the simulated fuel and buffer gas were mixed prior to injection, $\bar{P}_F/P_1|_{\text{MIX}}$. It represents a minimum desired level of containment of simulated fuel. The data in Fig. 14 show that the average simulated-fuel partial pressure was 20 percent greater at an injection velocity ratio of 0.22 than at a ratio of 1.1. This result is probably due to the reduced level of turbulence caused by the simulated-fuel injection at the lower injection velocity ratio. Also, the value of simulated-fuel partial pressure at the peripheral-wall is practically unaffected by changes in injection velocity ratio.

The effects of changes in the bypass ratio at a constant injection velocity ratio, ($v_F/v_j = \text{constant}$) are shown in Fig. 15. Here also the average simulated-fuel partial pressure varied, increasing almost twofold when the bypass ratio was increased from 0 to 96 percent. Also, Fig. 15 shows that bypass ratio is one of the factors controlling the location of the maximum radial gradient of simulated-fuel partial pressure and the amount of simulated-fuel present at the peripheral-wall. The location of this gradient moved radially outward and the amount of simulated fuel at the peripheral wall increased threefold as bypass was increased from 0 to 96 percent.

Tests with End-Wall ($r/r_1 = 0.8$) Simulated-Fuel Injection

Results with end-wall simulated-fuel injection at $r/r_1 = 0.8$ are presented in Figs. 16 and 17. Radial distributions of simulated-fuel partial pressure for these simulated-fuel injection velocities at 48 percent bypass are presented in Fig. 16. These data exhibit the same characteristics as the data for peripheral-wall simulated-fuel injection described above. The lowest fuel-to-buffer injection velocity ratio (0.2) resulted in the largest average simulated-fuel partial pressure ratio (0.19). However, at all injection velocity ratios and at comparable bypass ratios (Fig. 17), there was less simulated fuel at the peripheral wall with end-wall injection at $r/r_1 = 0.8$ than with peripheral-wall injection. Note also that the peak simulated-fuel partial pressures are greater for end-wall injection at $r/r_1 = 0.8$ than for peripheral-wall injection.

Tests with End-Wall ($r/r_1 = 0.5$) Simulated-Fuel Injection

Results obtained with end-wall simulated-fuel injection at $r/r_1 = 0.5$ are presented in Figs. 18 and 19. Radial distributions of simulated-fuel partial pressure for several simulated-fuel injection velocities are shown in Fig. 18. These results exhibit characteristics similar to the results obtained with simulated-fuel injection from the peripheral wall and from the end wall at $r/r_1 = 0.8$ except for the location of the maximum radial gradient of simulated-fuel partial pressure. In this case the location of this gradient is well away from the peripheral wall, approximately at the radius of simulated-fuel injection.

The average simulated-fuel partial pressures are considerably less for this injection configuration than for the other two injection configurations discussed, except at the highest percent bypass ratio (see Fig. 19). At 48 percent bypass, for example, the average simulated-fuel partial pressures for all three injection velocities (Fig. 18) are less than the fully-mixed value ($\bar{P}_F/P_1|_{MX}$). This indicates that some of the simulated fuel was "short-circuited" out of the vortex. The amount of simulated fuel present at the peripheral wall was as much as 24 times less with this injection configuration than it was with either end-wall injection at $r/r_1 = 0.8$ or peripheral-wall injection.

Tests with Centerline Simulated-Fuel Injection

The results of tests at four bypass ratios with centerline simulated-fuel injection are presented in Fig. 20. The simulated-fuel injection velocity was approximately constant in these tests. It is apparent from Fig. 20 that little simulated-fuel was contained in the vortex flow. Even at the highest bypass ratio tested (95 percent), the average simulated-fuel partial pressure ratio is well below the fully-mixed value. It is obvious that centerline simulated fuel injection, in unheated tests with the 10-in.-ID vortex tube, resulted in extensive short-circuiting of simulated fuel. This result is probably due to the high axial velocities present in the central region of the vortex flow. As expected with such low average partial pressures, there was very little simulated fuel at the peripheral wall -- less than can be accurately measured by the optical methods used. The minimum detectable value of simulated-fuel partial pressure is approximately 0.001.

Summary of Results of Tests with Various Configurations

Results of tests employing the four simulated-fuel injection configurations are summarized in Figs. 21 through 23. Typical radial distributions of simulated-fuel partial pressures for the four simulated-fuel injection configurations tested is presented in Fig. 21. The data show, in general, that increasing the radius at which simulated fuel is injected increases the average simulated-fuel partial pressure. However, the amount of simulated fuel present at the peripheral wall is also increased.

Note also that the simulated fuel tends to be confined primarily within the radius of injection, regardless of the bypass ratio (see Figs. 17 and 19), at least for the end-wall injection cases. For the given flow conditions, it appears that end-wall injection at a radius ratio between 0.8 and 0.5 might result in a high average partial pressure similar to that with injection at $r/r_1 = 0.8$, while maintaining a low amount of simulated fuel at the peripheral wall, similar to that with injection at $r/r_1 = 0.5$. For end-wall simulated-fuel injection at $r/r_1 = 0.5$, an average simulated-fuel partial pressure ratio greater than 0.25 (approximate minimum for the nuclear light bulb reference engine) was obtained while maintaining a value of the ratio of the peak simulated-fuel partial pressure to the partial pressure at the peripheral wall of the vortex tube greater than approximately 30 (see Fig. 19).

Figures 22 and 23 present a summary of the simulated-fuel containment at the injection velocity ratios and bypass ratios tested. The variations of average partial pressure with injection-velocity ratio are presented in Figs. 22(a), 22(b), and 22(c) for three bypass ratios, 0, 48, and 83 percent, respectively. With one exception, the same trend is evident at all three bypass ratios for the three configurations. The average simulated-fuel partial pressure increases with decreasing injection velocity ratio until a minimum injection velocity ratio was reached ($v_F/v_B \approx 0.2$) below which the average partial pressure may decrease significantly. This result is probably due to short-circuiting of the simulated fuel, since it may be carried away by the boundary layer flow when injected with too low a velocity. This reason probably also accounts for the one exception -- the increase in average partial pressure with increasing injection velocity ratio for end-wall ($r/r_1 = 0.5$) injection at 0 percent bypass (Fig. 22(a)). Also shown in Figs. 22(a), (b), and (c) are the greater average partial pressures obtained with simulated-fuel injection from the peripheral wall and from the end wall at $r/r_1 = 0.8$ compared with end-wall injection at $r/r_1 = 0.5$. The data from tests in the 1.26-in.-ID vortex tube shown in Figs. 22 and 23 will be discussed in a following section.

The variation of average simulated-fuel partial pressure with percent bypass for the four configurations tested is presented in Fig. 23. The injection velocity ratio is approximately constant at 0.55. As expected from past data (see Fig. 29 of Ref. 7), the average simulated-fuel partial pressure increases with increasing bypass ratio. From Fig. 23, it is evident that simulated-fuel injection from the peripheral wall and from the end wall at $r/r_1 = 0.8$ resulted in the highest average simulated-fuel partial pressures.

Figures 15 and 17 show that increasing the percentage of buffer-gas bypass flow from 0 percent to a maximum of 96 percent resulted in about a twofold increase in average simulated-fuel partial pressure for peripheral-wall and end-wall ($r/r_1 = 0.8$) simulated-fuel injection. Correspondingly, this increase in bypass flow resulted in a tenfold increase in average simulated-fuel partial pressure for centerline and end-wall ($r/r_1 = 0.5$) simulated-fuel injection (see Figs. 19 and 20). However, this

increased bypass flow also resulted in approximately a fivefold increase in the amount of simulated fuel present at the peripheral wall with all four injection methods (see Figs. 15, 17, 19, and 20). It should be noted, however, that an average simulated-fuel partial pressure greater than the minimum required for the reference nuclear light bulb engine (≈ 0.25) can be obtained with end-wall injection at $r/r_1 = 0.5$ by properly choosing the flow parameters (e.g., Fig. 19). Also, this injection method has the advantage of resulting in much less simulated fuel at the peripheral wall than the peripheral-wall or end-wall at $r/r_1 = 0.8$ injection configurations.

Results of Tests Employing Different Molecular Weight Ratios

A test was conducted using sulfur-hexafluoride as the buffer gas and a mixture of helium and iodine as the simulated fuel. The resulting radial distribution of simulated-fuel partial pressure is presented in Fig. 24. For comparison, the radial distribution from a test in which the buffer gas was air and the simulated fuel was a mixture of nitrogen and iodine with approximately equal flow conditions is also shown. The simulated fuel was injected from the end wall at $r/r_1 = 0.8$. The purpose of this test was to simulate isothermally the conditions that would exist in a nuclear light bulb engine, i.e., a (hot) low-density fuel region surrounded by a (cold) high-density buffer gas.

These data indicate that a vortex flow having a large value of buffer-to-simulated-fuel density ratio ($\rho_B/\rho_F = 32.6$) result in a large simulated-fuel partial pressure gradient and in an average simulated-fuel partial pressure approximately twice as great as a vortex flow having a small value of buffer-to-simulated-fuel density ratio ($\rho_B/\rho_F = 1.0$). The peak simulated-fuel partial pressure indicated at the large radius ratio (upper and lower) is typical of high-bypass-ratio, low-tangential-velocity test results. The amount of simulated fuel at the peripheral wall was nearly the same in the two tests.

The radial distribution of simulated-fuel partial pressure roughly corresponds to the idealized radial distribution for the reference nuclear light bulb engine (see Ref. 11). The major difference between the two distributions is in the values of the partial pressure at the peripheral wall. No maximum allowable fuel partial pressure has been defined for the nuclear light bulb engine. However, it is desirable that the fuel partial pressure be as close to zero as possible to preserve the transmission characteristics of the transparent peripheral wall.

Unheated Vortex Tests with 1.26-in.-Dia Vortex Tube

Unheated tests were conducted using the 1.26-in.-ID vortex tube with vortex configurations having a peripheral-wall buffer-gas injection (see Fig. 2(b)) and three different simulated-fuel injection configurations. The purpose of these tests was to provide data for comparison with results of tests using the geometrically similar 10-in.-ID vortex tube. The simulated-fuel injection configurations for which quantitative data were obtained (1) end wall at $r/r_1 = 0.5$ and (2) centerline injection (see Figs. 2(b) and 6(b)). In addition, a configuration having end-wall injection at $r/r_1 = 0.8$ was tested; a partial set of data were obtained for this configuration. Tests were conducted at three bypass ratios. The buffer-gas flow rate and the simulated-fuel flow rate were maintained approximately constant. The buffer gas was argon, and the simulated fuel was a mixture of argon and bromine. A summary of flow conditions and configurations employed is given in Table VI. The test results are presented in Figs. 25 and 26.

Tests with End-Wall ($r/r_1 = 0.8$) Simulated-Fuel Injection

No quantitative results are presented for this injection configuration. The light being scanned by the monochromator (see section entitled TEST EQUIPMENT AND PROCEDURES) was blocked by the peripheral-wall buffer-gas injectors at a radius ratio of approximately 0.8, thus eliminating acquisition of data beyond a radius ratio of 0.8. The accuracy of the simulated-fuel radial distribution is grossly affected by data taken at large radius ratios if significant amounts of simulated fuel are present at these radius ratios. It was observed that there was a significant amount of simulated fuel both inside and outside of the 0.8 radius ratio.

Tests with End-Wall ($r/r_1 = 0.5$) Simulated-Fuel Injection

The results of tests with end-wall simulated-fuel injection at $r/r_1 = 0.5$ are presented in Fig. 25. Tests were conducted at two bypass ratios, 44 and 69 percent. The same light blockage at radius ratio greater than 0.8 mentioned above was encountered with this configuration, but the error involved in extrapolating the data to a radius ratio of 1.0 is not considered significant since there was very little simulated fuel in this region. This extrapolation is indicated by the dashed lines at the ends of the curves in Fig. 25.

The data in Fig. 25 indicate that increasing the amount of bypass flow significantly increases the average simulated-fuel partial pressure and the volume that the simulated fuel occupies. No conclusions can be reached regarding the amount of simulated fuel at the peripheral wall due to the absence of data. In general, these results for the 1.26-in.-ID vortex tube tests are quite similar to those for the 10-in.-ID vortex tube tests (see Figs. 22 and 23).

Tests with Centerline Simulated-Fuel Injection

Figure 26 presents the results of tests in the 1.26-in.-ID vortex tube with centerline simulated-fuel injection. Tests were conducted at three bypass ratios, 0, 44, and 69 percent. The light blockage at radius ratios greater than 0.8 again introduces some error in average simulated-fuel partial pressure and the value at the peripheral wall, especially for the data at 69 percent bypass. Extrapolated portions of the curves are again indicated by the dashed lines.

The data of Fig. 26 also indicate an increase in the volume occupied by the simulated fuel and in the average simulated-fuel partial pressure with increasing bypass flow. This is similar to the previous results for the two vortex tube sizes tested -- 1.26-in.-ID and 10-in.-ID. However, the average simulated-fuel partial pressure obtained with centerline injection in the 1.26-in.-ID tube was significantly greater than that obtained with centerline injection in the 10-in.-ID tube (see Fig. 27). The values obtained were approximately equal to the partial pressures obtained with end-wall simulated-fuel injection at $r/r_1 = 0.5$ in the 10-in.-ID vortex tube (see Figs. 22, 23, and 27).

Comparison of Vortex Containment Experiments

Results of several series of tests in which the amount and distribution of simulated fuel contained within a vortex flow were measured were described in the preceding sections. These tests were conducted in a 10-in.-dia and a 1.26-in.-dia vortex tube in which the flow is at constant temperature (unheated tests), and in the 1.26-in.-dia vortex tube in which a large temperature gradient was imposed upon the flow (heated tests). In these tests, efforts were made to maintain, when possible, similar vortex tube geometries and similar flows (compare Figs. 2(b), 5, and 6).

Figure 27 presents the radial distributions of simulated-fuel partial pressure for the two different-sized vortex tubes but with approximately similar (unheated) flow conditions (i.e., the injection and radial Reynolds number and the percent bypass flow are approximately equal for the two vortex tubes). Data are presented for simulated-fuel injection at $r/r_1 = 0.5$ and on the centerline. As noted previously (see Fig. 21), results from the 10-in.-dia vortex tube tests showed large differences in simulated-fuel containment as the simulated-fuel injection location was changed (compare triangle and diamond data points in Fig. 27). In the 1.26-in.-dia vortex tube, the simulated-fuel injection location had no appreciable effect on the contained simulated fuel (compare circle and square data points in Fig. 27).

For similar flow conditions (Re_j , Re_r , and percent bypass), the radial distributions of simulated-fuel partial pressure obtained in the two different-sized vortex tubes agreed reasonably well when the simulated-fuel injector was at $r/r_1 = 0.5$ (compare circle and triangle data points in Fig. 27). The difference in simulated-fuel partial pressures in the central region of the vortex are not considered significant because the amount of simulated fuel stored in this region is small compared with that stored at larger radii.

Large differences occurred in the radial distribution of simulated-fuel partial pressures obtained with centerline simulated-fuel injection (compare square and diamond data points in Fig. 27). Centerline injection in the small vortex tube results in an average simulated-fuel partial pressure ratio approximately 20 times that of the large vortex tube for similar flow conditions. In comparing the data obtained with centerline simulated-fuel injection, it should be noted that the through-flow port geometries were not identical in the two vortex tubes. Figure 28 presents sketches of the two vortex tubes used with centerline simulated-fuel injection. The geometrical differences shown may account for the large differences in containment characteristics.

Although the injection and radial Reynolds numbers were approximately the same, the flow patterns within the vortices may have been quite different. End wall static pressure measurements made in the two vortex tubes operating at similar flow conditions are presented in dimensionless form in Fig. 29 (data from both heated and unheated tests obtained in the 1.26-in.-dia vortex tube are included in Fig. 29). The radial momentum equation for a constant temperature vortex permits the tangential velocity to be evaluated from the radial derivative of the static pressure (see Ref. 12):

$$\frac{dP}{d(r/r_1)} = \frac{\rho}{g} \frac{v_\phi^2}{(r/r_1)} \quad (3)$$

Figure 30 presents the radial distributions of tangential velocity for the unheated vortex flows. For comparison, the tangential velocity distribution for a free vortex is also shown. The large difference in the tangential velocity distributions between the two vortex tubes is indicative of differences in vortex flow patterns. A possible explanation for the difference shown in Fig. 30 is that the turbulence level in the small-diameter vortex tube was greater than in the larger tube. The close similarity of the simulated-fuel distribution obtained with the two injection locations in the 1.26-in.-dia tube (see Fig. 27) may also be indicative of a higher turbulence level in the smaller vortex tube.

It is possible that the difference in buffer-gas injection configurations (compare Fig. 2(b) with Fig. 5(a) of Ref. 7) could cause a difference in turbulence level, or it may be that a small vortex is simply more turbulent. That is, the mechanisms of a vortex flow (such as circulation gradients or accelerating flow within the end-wall boundary layers) that apparently damp out turbulence due to injection may not be present in a small tube, or, if present, are of insufficient magnitude or occur over an insufficient time to successfully remove this turbulence.

Differences in the simulated-fuel containment were noted in heated and unheated tests in the same size (1.26-in.-dia) vortex tube operating at similar flow conditions (see Fig. 31). However, with centerline simulated-fuel injection, the differences between the heated and unheated test data were much less than the corresponding differences between unheated test data obtained in different-sized vortex tubes (compare Figs. 27 and 31). (The axially-averaged simulated-fuel partial pressures shown in Figs. 27 and 31 for the tests in the 1.26-in.-dia vortex tube were obtained by averaging the local partial pressures at each of the four axial positions.)

In discussing differences between heated and unheated tests, it is well to bear in mind the restrictions on the flow conditions that exist in an r-f heated vortex. In the unheated tests, the simulated-fuel injection location could be placed at any of several positions on the end wall and reasonable simulated-fuel containment could be obtained. While one location may result in a greater amount of simulated fuel contained than another location, the difference is relatively small. Conversely, in heated tests it was determined that only simulated-fuel injection along the vortex centerline would give satisfactory results (see Ref. 7). As discussed in Ref. 7, very little simulated fuel entered the plasma region of the flow when injected from any end-wall position other than at the centerline. The reason for this is believed to be that axial velocities along the boundary of the plasma sweep the simulated fuel away from the plasma region (the plasmas that have been generated in the laboratory all have been approximately ellipsoidal in shape (see Refs. 7, 13, and 14)). Thus, it has not been possible to inject simulated fuel into the plasma region from the end wall without crossing the large temperature gradient, except within the thru-flow port diameter.

In tests conducted with unheated flows, there is relative freedom of selection of the radial Reynolds number. Adjustment of the radial Reynolds number can be made over a fairly large range of values (for a given buffer-gas injection condition) to obtain satisfactory simulated-fuel distributions. In heated flows, no such freedom exists. The value of the radial Reynolds number required to maintain the desired plasma size is established to a large extent by the amount of power that must be convected away from the plasma. It was shown theoretically in Ref. 15 that, for a confined plasma to exist in a vortex flow, a heat sink must be present at the edge of the plasma region. It was experimentally determined in Refs. 13 and 14 (for a one-component plasma) that an increase in radial Reynolds number generally was

required for increased power into the plasma. The vortex similarity parameter, β_T , developed in Ref. 12 for unheated vortex flows shows that, for similar geometries, only the ratio of the 0.8 power of the tangential injection Reynolds number to radial Reynolds number need be maintained for similar flow patterns to exist. However, even if the radial and injection Reynolds numbers are the same in heated and unheated flows, the flow patterns within the vortex may not be similar. The presence of the temperature gradient may severely alter the radial and axial velocities within the vortex. Thus, it may be tentatively concluded that: (1) even if the injection and radial Reynolds numbers are the same, the flows in small vortex tubes may not be similar to the flows in large vortex tubes because of small but significant differences in the buffer-gas injectors, thru-flow port geometry, etc. (these differences may lead to higher turbulence levels in the small tubes); and (2) even if the Reynolds number in the unheated portions of the flows are matched, the flow patterns in the high temperature region of a heated vortex may be different from the flow patterns in the corresponding region of an unheated vortex because the local Reynolds numbers are different.

REFERENCES

1. McLafferty, G. H. and H. E. Bauer: Studies of Specific Nuclear Light Bulb and Open-Cycle Vortex-Stabilized Gaseous Nuclear Rocket Engines. United Aircraft Research Laboratories Report F-910093-37, prepared under Contract NASw-847, September 1967. Also issued as NASA CR-1030, 1968.
2. Kendall, J. S., W. C. Roman, and P. G. Vogt: Initial Radio-Frequency Gas Heating Experiments to Simulate the Thermal Environment in a Nuclear Light Bulb Reactor. United Aircraft Research Laboratories Report G-910091-17, prepared under Contract NASw-847, September 1968. Also issued as NASA CR-1311.
3. Kendall, J. S.: Experimental Investigation of Heavy-Gas Containment in Constant Temperature Radial-Inflow Vortexes. United Aircraft Research Laboratories Report F-910091-15, prepared under Contract NASw-847, September 1967.
4. Kendall, J. S., A. E. Mensing, and B. V. Johnson: Containment Experiments in Vortex Tubes with Radial Outflow and Large Superimposed Axial Flows. United Aircraft Research Laboratories Report F-910091-12, prepared under Contract NASw-847, May 1967. Also issued as NASA CR-993.
5. Mensing, A. E. and J. S. Kendall: Experimental Investigation of Containment of a Heavy Gas in a Jet-Driven Light-Gas Vortex. United Aircraft Research Laboratories Report D-910091-4, prepared under Contract NASw-847, March 1965.
6. Mensing, A. E. and J. S. Kendall: Experimental Investigation of the Effect of Heavy- to Light-Gas Density Ratio on Two-Component Vortex Tube Containment Characteristics. United Aircraft Research Laboratories Report D-910091-9, prepared under Contract NASw-847, September 1965.
7. Mensing, A. E. and J. F. Jaminet: Experimental Investigations of Heavy-Gas Containment in R-F Heated and Unheated Two-Component Vortexes. United Aircraft Research Laboratories Report H-910091-20, prepared under Contract NASw-847, September 1969.
8. Marteney, P. J., A. E. Mensing, and N. L. Krascella: Experimental Investigation of the Spectral Emission Characteristics of Argon-Tungsten and Argon-Uranium Induction Heated Plasmas. United Aircraft Research Laboratories Report G-910092-11, prepared under Contract NASw-847, September 1968. Also issued as NASA CR-1314.

REFERENCES (Continued)

9. Mensing, A. E. and J. S. Kendall: Experimental Investigation of Containment of Gaseous Iodine in a Jet-Driven Vortex. Air Force Systems Command Report RTD-TDR-63-1093, prepared by United Aircraft Research Laboratories under Contract AF 04(611)-8189, November 1963.
10. McMahon, D. G. and R. Roback: Machine Computation of Chemical Equilibrium in Reacting Systems. In Kinetics, Equilibria, and Performance of High Temperature Systems. Proceedings of the First Conference Western States section of the Combustion Institute, Los Angeles, California, November 1959; edited by G. S. Bahn and E. E. Zukoski, Butterworths, Washington, 1960.
11. Krascella, N. L.: Theoretical Investigation of the Radiant Emission Spectrum From the Fuel Region of a Nuclear Light Bulb Engine. United Aircraft Research Laboratories Report H-910092-12, prepared under Contract NASw-847, October 1969.
12. Anderson, O.: Theoretical Effect of Mach Number and Temperature Gradient on Primary and Secondary Flows in a Jet-Driven Vortex. Air Force Systems Command Report RTD-TDR-63-1098, prepared by United Aircraft Research Laboratories under Contract AF 04(611)-8189, November 1963.
13. Roman, W. C., J. F. Klein, and P. G. Vogt: Experimental Investigation to Simulate the Thermal Environment, Transparent Walls, and Propellant Heating in a Nuclear Light Bulb Engine. United Aircraft Research Laboratories Report H-910091-19, prepared under Contract NASw-847, September 1969.
14. Roman, W. C.: Experimental Investigation of a High-Intensity R-F Radiant Energy Source to Simulate the Thermal Environment in a Nuclear Light Bulb Engine. United Aircraft Research Laboratories Report J-910900-4, prepared under Contract SNPC-70, September 1970.
15. Mensing, A. E. and L. R. Boedeker: Theoretical Investigations of R-F Induction Heated Plasmas. United Aircraft Research Laboratories Report G-910091-18, prepared under Contract NASw-847, September 1968. Also issued as NASA CR-1312.
16. Herzberg, G.: Molecular Spectra and Molecular Structure, I - Spectra of Diatomic Molecules. D. Van Nostrand Co., Princeton, New Jersey, 1950.

REFERENCES (Continued)

17. Bauer, H. E., R. J. Rodgers, and T. S. Latham: Analytical Studies of Start-Up and Dynamic Response Characteristics of the Nuclear Light Bulb Engine. United Aircraft Research Laboratories Report J-910900-5, prepared under Contract SNPC-70, September 1970.
18. Nixon, F. E.: Principles of Automatic Controls. Prentice-Hall, Inc., Englewood Cliffs, New Jersey, 1953.

LIST OF SYMBOLS

a	Constant in transfer function (used in Appendix C)
$A_{B,j}$	Buffer-gas injection area, sq in.
$A_{F,j}$	Simulated-fuel injection area, sq in.
b, c	Constants in transfer function (used in Appendix C)
d	Diameter of vortex tube, in.
d	Constant in transfer function (used in Appendix C)
E_n	Upper energy level, ev
f	R-F frequency, Hz
g	Acceleration of gravity, 32.2 ft/sec. ²
\bar{g}	Gaunt factor, dimensionless
I/I_0	Light transmittance, dimensionless
I_c	Intensity of continuum radiation, w/cm ³ -nm
I_{LINE}	Intensity of radiation of a single line, w/cm ³
k	Boltzmann constant, 1.38×10^{-16} erg/deg K (used in Appendix A)
k	Indexing integer (used in Appendix B)
k	Constant in transfer function (used in Appendix C)
K_{LINE}	Constant used in Eq. (A-3)
l	Path length of light beam, ft.
L	Length of vortex chamber, in. or ft.
m_B	Molecular weight of buffer gas
m_C	Molecular weight of carrier gas
m_F	Molecular weight of simulated fuel

LIST OF SYMBOLS (Continued)

M	Total intervals in numerical integration (used in Appendix B)
N	Number density, cm^{-3}
N_e	Number density of electrons, cm^{-3}
N_+	Number density of singly ionized atoms, cm^{-3}
m	Indexing integer (used in Appendix B)
P	Static pressure, atm
P_F	Simulated-fuel partial pressure, atm
\bar{P}_F	Volume-averaged simulated-fuel partial pressure, atm
P_{xe}	Xenon partial pressure, atm
P_{xe^0}	Partial pressure of un-ionized xenon, atm
P_{xe^+}	Partial pressure of singly ionized xenon, atm.
P_l	Static pressure at vortex tube peripheral wall, atm
Q_{DC}	D-C power to r-f power amplifier, kw
Q_R	Power radiated, kw
Q_T	Total power deposited in plasma, kw
Q_F/Q_B	Simulated-fuel-to-buffer-gas volume flow rate ratio, dimensionless
r	Radius, in. or ft.
r_l	Radius of vortex chamber, in. or ft.
Re_j	Injection Reynolds number, dimensionless
Re_r	Radial Reynolds number, dimensionless
s	Laplace operator, d/dt
t	Time, sec. (used in Appendix C)

LIST OF SYMBOLS (Continued)

t_{\min}	Simulated-fuel time constant for fully mixed flow, sec
t_s	Time from switch actuation in transients tests, sec
T	Temperature, deg R or deg K
T	Time constant (see Fig. 44), sec.
T_e	Electron temperature, deg K
v_F	Injection velocity of simulated fuel, ft/sec
v_j	Injection velocity of buffer gas, ft/sec
v_ϕ	Tangential velocity, ft/sec
v_{ϕ_1}	Tangential velocity of buffer gas at peripheral wall, ft/sec
V	Volume of vortex chamber, ft ³
w_B	Weight flow of buffer gas, lb/sec
w_{Br}	Weight flow of bromine vapor, lb/sec
w_C	Weight flow of carrier gas, lb/sec
w_F	Weight flow of simulated-fuel, lb/sec
w_I	Weight flow of iodine vapor, lb/sec
w_x	Weight flow of xenon, lb/sec
\mathcal{W}_F	Total amount of simulated-fuel in vortex chamber, lb.
y	Perpendicular distance from chord line (used in Appendix B)
x	Axial distance measured from left end wall, in.
Z_{eff}	Effective ionic charge, dimensionless
Z_p	Reflected impedance, ohms

LIST OF SYMBOLS (Continued)

α	Absorption coefficient, ft^{-1}
δw_F	Instantaneous value of change in simulated-fuel flow rate, lb/sec
δW_F	Instantaneous value of change in amount of simulated-fuel stored, lb
$\Delta w_{F\infty}$	Steady-state change in simulated-fuel flow rate, lb/sec
$\Delta W_{F\infty}$	Steady-state change in amount of simulated-fuel stored, lb
Δw_{FOS}	Overshoot in change in simulated-fuel flow rate lb/sec
ΔW_{FOS}	Overshoot in change in amount of simulated-fuel stored, lb
ζ	Damping ratio, dimensionless
λ	Wavelength Å
λ_{Fo}	Fuel decay constant, sec^{-1} (used in Appendix C)
ρ	Density, lb/ft^3
ρ_B	Density of buffer gas, lb/ft^3
ρ_F	Density of simulated-fuel, lb/ft^3
ρ_{Br}	Density of bromine vapor, lb/ft^3
ρ_I	Density of iodine vapor, lb/ft^3
$\bar{\rho}_F$	Volume-averaged density of simulated fuel, lb/ft^3
ω_n	Natural frequency, rad/sec (used in Appendix C)
$(dW_F/dt)_0$	Initial slope of simulated-fuel-stored response, lb/sec

Subscripts

MIX	Refers to conditions where simulated fuel and buffer gas are fully mixed.
l	Refers to conditions at peripheral wall

LIST OF SYMBOLS (Continued)

4300	Denotes ArI 4300 Å line
4320	Denotes argon continuum at 4320 Å
4671	Denotes XeI 4671 Å line
6965	Denotes ArI 6965 Å line

APPENDIX A

CALIBRATION AND USE OF OPTICAL SYSTEM FOR DETERMINATION OF
PLASMA TEMPERATURE AND XENON PARTIAL PRESSURE

The optical system employed in the tests with the UARL 80-kw r-f induction heater has been discussed in Ref. 7. In this system, a lens located 40 in. from the plasma focuses the plasma image on the plane of the entrance slit of a one-quarter meter monochromator. The monochromator is fitted with an EMI 9558 photomultiplier tube whose output is fed to a strip-chart recorder. The monochromator traverses across the plasma image at constant speed (approximately 5 in./min). The entrance slit of the monochromator is 0.25-in. by 25 microns. The image size is 1.6 times the actual source size.

The monochromator (including slits and photomultiplier tube) was calibrated by comparing the photomultiplier tube output signal to a known light intensity obtained from an Eppley Laboratory Standard of Spectral Irradiance. The instrument was calibrated throughout the range from 4000 Å to 8000 Å. Once the calibration had been made no changes were made in the system (i.e., the driving voltage for the photomultiplier tube and the slit sizes were fixed). The lens system was calibrated by placing a 6 v-30 amp tungsten ribbon lamp at the position usually occupied by the plasma. The size of the ribbon was 0.14 in. by 0.64 in. The temperature and emissivity of the tungsten ribbon had been determined by comparing its irradiance to that of the Standard. Radiation from the tungsten ribbon lamp was focused through the lens onto the face of the monochromator in the same manner as the plasma radiation. From the known radiation of the tungsten ribbon (in watts/cm²-nm) determined from its temperature and emissivity, the output of the photomultiplier tube was then determined as a function of the source radiation. Once this calibration was made, no changes were made in any of the optical components. The use of the ribbon lamp was an additional calibration that was not done in Ref. 7, and it is believed the present method provides improved accuracy over that of Ref. 7. In addition, a strip-chart used for data recording in the tests gave a much better output record than did the visicorder used in Ref. 7. However, when wavelength scans were made of the plasma, the slow response (approximately 0.25-sec full-scale) of the strip-chart recorder necessitated scanning at 100 Å/min instead of the 1000 Å/min employed in Ref. 7.

Measurements along the diameter of the plasma were made by scanning the monochromator from 4000 Å to 8000 Å. The axial position located at $x/L = 0.32$ was used for these tests. From the measured diameter of the plasma at this axial position, an intensity-averaged plasma temperature was calculated from the measured radiation of the argon continuum at 4320 Å. The continuum at 4320 Å was chosen as a reference since it appears to be the best documented region of an argon plasma. According to

Ref. 8, the intensity of the argon continuum can be calculated from,

$$I_c = 2.03 \times 10^{-22} \bar{g} Z_{\text{eff}} \frac{N_e N_+}{T_e^{1/2}} \frac{1}{\lambda^2} \text{ watts/cm}^3 - \text{nm} \quad (\text{A-1})$$

In Eq. (A-1), N_e and N_+ are the electron and ion number-density, respectively, and are assumed equal for the pure argon plasma; T_e is the electron temperature, and is assumed equal to the gas temperature; Z_{eff} , is the effective-charge per ion and is assumed equal to 1.0, \bar{g} is the Gaunt factor which has a value of approximately 2.3 for argon near 4300 Å (Ref. 8); λ is the wavelength in Å. The plasma is assumed to be in thermodynamic equilibrium and in charge equilibrium (i.e., $N_e = N_+$). At a wavelength of 4320 Å, the radiated intensity of the argon continuum is

$$I_{4320} = 25.0 \times 10^{-33} \frac{N_e^2}{T_e^{1/2}} \text{ watts/cm}^3 - \text{nm} \quad (\text{A-2})$$

The measured intensity along a diameter can be related to the temperature once the electron number-density is determined as a function of temperature. The method of Ref. 10 was used to obtain this relationship. Figure 32 presents the variation of continuum intensity (in $\text{w/cm}^3 - \text{nm}$) with temperature for an argon plasma at 1.3 atm. An intensity-averaged temperature is then determined from the measured intensity and Fig. 32. Use of a continuous source for calibration (i.e., the tungsten ribbon lamp) and the argon continuum for a temperature reference avoids the difficulty of determining the bandwidth resolution of the monochromator.

Since the purpose of the experiments in this study was to determine the temperature and partial pressure of a seeded argon plasma, the continuum could not be used once the seed material was introduced into the plasma (a relationship similar to Eq. (A-2) does not exist for an argon plasma seeded with xenon). Thus, it was necessary to use line-intensity measurements for temperature and pressure determination of the seeded plasma. Both the ArI 4300 Å and ArI 6965 Å line were used for temperature determination. When small amounts of xenon (such as in the premixed tests) were in the plasma, the ArI 4300 Å line was used. However, at larger xenon partial pressures, the difference between the ArI 4300 Å line and the continuum was too small for accurate measurement, so the ArI 6965 Å line was used in these tests. All xenon data were obtained from the XeI 4671 Å line. The peak intensity of the lines was determined by the maximum output signal of the photomultiplier tube. The peak line intensity can be related to the pressure and temperature by

$$I_{\text{LINE}} = K_{\text{LINE}} \frac{P_0}{T} e^{-E_n/kT} \quad (\text{A-3})$$

where P_0 is the pressure of the neutral atoms in atm, E_n is the upper energy level in electron volts, and k is the Boltzmann constant. For argon, the constant, K_{LINE} , was determined for each line by measuring the peak recorded intensity of an argon-only plasma and the intensity-averaged temperature as determined from the argon continuum. Equation (A-3) was then solved for K_{LINE} . The measured peak intensity of the line is, of course, not the total line intensity since no account is taken of the width of the line which would be determined by instrument broadening. However, provided the half-width of the line as seen by the photomultiplier tube is constant, the total line intensity and measured peak intensity will be proportional. Self-absorption can broaden the line, but calculations have shown that for the temperatures and pressures discussed in this report, self-absorption should be negligible. In obtaining the data that allows the temperature of the seeded argon plasma to be determined, the wavelength position of the monochromator was adjusted until the output signal of the photomultiplier was a maximum for a given line, then the monochromator was scanned across the plasma image, and the variation of image peak line intensity was recorded as a function of chordal position. The continuum near the line was also scanned and recorded. The difference between the peak line intensity and the continuum intensity was then used as input to an inversion program that calculates the intensity as a function of radius. The variation with temperature of the peak intensity of the ArI 6965 Å line is shown in Fig. 33 for various argon pressures.

Similar techniques were used to calculate K_{LINE} for the XeI 4671 Å line. As described in the main text (see section entitled DISCUSSION OF RESULTS), a standard test with a known argon-xenon mixture was used to determine K_{LINE} for XeI 4671 Å. Again, only peak line intensities were recorded. In conducting the tests, the monochromator was positioned at the maximum value of the 4671 Å line and scanned across the plasma. The continuum at approximately 4660 Å was also recorded and the difference in the two measurements was used as the peak intensity of the line. Thus, in conducting tests, four scans of plasma were taken at each of the four axial positions. Figure 34 presents the variation with temperature of the peak-intensity per unit pressure (i.e., $I_{\text{LINE}}/P_{\text{Xe}^0}$) of the XeI 4671 Å line.

In tests having values of xenon partial pressure greater than approximately 0.1 atm, determination of the xenon partial pressure from measurements of the 4671 Å line (from Eq. (A-3) once I_{LINE} and T are known) does not account for all the xenon. An appreciable fraction of the xenon may be ionized and, therefore, not contribute to the 4671 Å line intensity (see Fig. 12). Figure 35 presents the variation of total xenon partial pressure (including electrons) as a function of the xenon neutral species partial pressure at various plasma temperatures. The method of Ref. 10, which assumes local thermodynamic equilibrium, was used to calculate the curves in Fig. 35.

As discussed in the section entitled DISCUSSION OF RESULTS, an iteration technique was employed for tests having a xenon partial pressure greater than 0.1 atm. This was necessary since the large xenon partial pressure causes a reduction in argon partial pressure (the total plasma pressure was known, but the species partial pressures were not). The following iteration procedure was used: (1) the argon pressure was assumed to be 1.3 atm and from the measured intensities of the ArI 6965 Å line the plasma temperature was determined from Fig. 33, (2) from this temperature and the measured intensities of the XeI 4671 Å line, the xenon neutral partial pressures were taken from Fig. 34, (3) the total xenon partial pressure was obtained from Fig. 35, (4) the xenon partial pressure was subtracted from the total plasma pressure (1.3 atm) and this value was used as the argon neutral partial pressure (the partial pressure of ionized argon was too small to be considered (see Figs. 11 and 12)), (5) a new temperature was then determined from Fig. 33 and the previous value of the ArI 6965 Å line intensity, and (6) from this new temperature and the XeI 4671 Å line intensity, a new xenon partial pressure was determined. This procedure was continued until the sum of the xenon partial pressures (including neutral atoms, ionized atoms, and electrons) and the argon partial pressure was equal to the measured plasma pressure, 1.3 atm.

In summary, the basic assumptions necessary to determine the temperature and xenon partial pressures within the plasma were; (1) local thermodynamic equilibrium exists between all species, (2) the spectral-line width is not affected by pressure, (3) no self-absorption of the line occurs, and (4) the total line strength is directly proportional to the recorded peak intensity of the line.

APPENDIX B

DETERMINATION OF BROMINE ABSORPTION CONSTANTS

To obtain data by light absorption techniques when using bromine in the 1.26-in.-dia vortex tube, it was necessary to determine the light absorption properties of bromine. This task was simplified greatly by previous work with iodine (see Ref. 9). In Ref. 9 it is shown that, at a given wavelength, the light absorption by iodine is proportional to the number of iodine molecules in the ground vibrational state (see Fig. 48 of Ref. 9). The number of molecules in the ground state is proportional to the temperature of the gas.

Because they are both halogens, iodine and bromine have similar light absorption properties. Thus, the same relation for the density of the gas, with different constants, may be used for both iodine and bromine. The differences in the two gases result in different values for the constant in the stimulated emission factor, the absorption coefficient, α , and the wavelength of maximum absorption. The constant in the stimulated emission factor for bromine was obtained from Ref. 16 and has a value of 830 (vs 553 for iodine).

The absorption coefficient and the wavelength of maximum absorption were determined from data obtained in a special test. In this test, light from a 1000-w tungsten filament lamp passed through a small fused silica test cell, 1-in.-long, to a monochromator. The light intensity transmitted through the test cell with bromine present (I) and without bromine present (I_0) was recorded throughout the spectrum from 3000 Å to 9000 Å. Since the bromine was in a saturated state (liquid and vapor phases in equilibrium) in the test cell and the temperature was measured, the partial pressure of the bromine vapor was known. From these data and the perfect gas law, the density of the bromine vapor was calculated. The wavelength of maximum absorption was obtained at the minimum value of the ratio of the two recorded intensities, I/I_0 . This wavelength was determined to be 4300 Å when the minimum intensity ratio was 0.0035.

The absorption coefficient at 4300 Å was determined to be 303.5 ft⁻¹ from the equation implied in Ref. 9:

$$\alpha = \frac{-\rho_{BrSTD}}{\rho_{Br} \ell} \frac{\ln \frac{I}{I_0}}{1 - e^{-\frac{830}{T}}} \quad (B-1)$$

where T is the absolute temperature of the bromine, l is the path length of the light through the bromine, and ρ_{BrSTD} is the density that gaseous bromine would have at standard conditions.

The radial distribution of bromine density in the vortex tube was calculated from the chordal scanning data by employing integration of a form of Eq. (B-1) over M small intervals of the chordal scan (see Ref. 5, Appendix II). For bromine at 4300 \AA , the numerical equation is

$$\rho_{Br, r=r_k} = -\frac{2M}{\pi r_l} \left(\frac{1}{303.5} \right) \left(\frac{\rho_{BrSTD}}{1 - e^{-\frac{830}{T}}} \right) \left[\frac{\ln I/I_0|_{y=y_k}}{\sqrt{2k+1}} + \sum_{m=k+1}^M \left\{ \frac{\sqrt{(m+1)^2 - k^2}}{2m+1} \right. \right. \\ \left. \left. + \frac{\sqrt{(m-1)^2 - k^2}}{2m-1} - \frac{4m\sqrt{m^2 - k^2}}{4m^2 - 1} \right\} \ln I/I_0|_{y=y_m} \right] \quad (B-2)$$

The radial distribution of simulated fuel was then calculated by the same methods used with iodine (see Ref. 7), i.e., by assuming that the bromine and argon carrier gas do not separate. If this is true, the density of the simulated fuel is related to the density of the bromine by:

$$\rho_F = \rho_{Br} \frac{w_F}{w_{Br}} \quad (B-3)$$

The molecular weight of the simulated fuel was determined from:

$$m_F = \frac{w_F}{\frac{w_{Br}}{159.8} + \frac{w_C}{39.9}} \quad (B-4)$$

The radial distribution of simulated-fuel partial pressure was then calculated from Eqs. (B-2), (B-3), (B-4), and the perfect gas law. The volume-averaged simulated-fuel partial pressure was computed by numerical integration by volume of the radial distribution of the simulated fuel.

As mentioned in the section entitled TEST EQUIPMENT AND PROCEDURES, an interference filter with a transmission bandwidth of 40 \AA centered at 4600 \AA was employed in the exhaust absorptometer. This filter was used because it was readily available. The value of the intensity ratio at 4600 \AA was found to be 0.00461 (31.7 percent less light absorption than at 4300 \AA). The absorption coefficient at 4600 \AA was also determined from Eq. (B-1) and has a value of 288.7 ft^{-1} . The bromine density was calculated from the data obtained from the exhaust absorptometer using Eq. (B-1).

APPENDIX C

NONSTEADY-STATE TESTS WITH 10-IN.-DIA VORTEX TUBE

This appendix describes isothermal nonsteady-state vortex tests conducted in the 10-in.-dia vortex tube. The purpose of these tests was to investigate the effect of perturbations in the simulated-fuel flow rate or the vortex static pressure on simulated-fuel containment.

Test Equipment and Procedures

The high Reynolds number test facility (described in the section entitled TEST EQUIPMENT AND PROCEDURES) was employed for these tests. The simulated-fuel supply system in the high Reynolds number test facility was modified by the addition of a control valve to vary the simulated-fuel injection flow rate. The valve is a solenoid-controlled, pneumatically operated ball valve, and was located approximately 2 ft upstream of the simulated-fuel injection ports. Using this valve, a 15 percent change in simulated-fuel flow rate could be produced within approximately 400 msec.

The thru-flow exhaust from the vortex tube was also modified by the addition of a control valve in one thru-flow duct to vary the static pressure in the vortex tube. The valve (also a solenoid-controlled, pneumatically operated ball valve) was located approximately 1.0 ft downstream of the thru-flow port. The valve actuation time was approximately 400 msec.

During the tests the radial position of the upper scanning light beam (described in the section entitled TEST EQUIPMENT AND PROCEDURES) was fixed. The appropriate flow or pressure was decreased until steady-state conditions were obtained, then increased until steady-state conditions were again obtained. All other flow settings were maintained constant. The light beam was then moved to a different radial location and the process repeated. In this way the time history of simulated-fuel density in the vortex was obtained at a number of radial locations. The data were numerically integrated over the total vortex tube volume at each (fixed) time to obtain the simulated-fuel contained as a function of time. Reference data were obtained before and after each set of test runs. For tests in which the simulated-fuel flow rate was varied, the time history of pressure in the simulated-fuel duct upstream of the control valve was also determined. In addition, the motion of the control valves was determined to be repeatable within approximately 5 percent. All tests were conducted with simulated-fuel injection from the end wall at $r/r_1 = 0.8$ and constant simulated-fuel injection area.

Two series of tests were conducted. For each series, tests were conducted at three flow conditions (three bypass ratios) with the buffer-gas flow rate approximately constant. In the first test series the simulated-fuel flow rate was increased and then decreased by approximately 15 percent. In the second test series the vortex static pressure was varied up to 2 percent by changing the amount of thru-flow exhausted from one thru-flow port. It should be noted that changing the vortex static pressure by varying the amount of thru-flow also changed other concomitant parameters, such as radial Reynolds number and, to a lesser extent, injection Reynolds number. These parameters would also vary in the full-scale engine if no feedback control loops were used.

During all tests, equal amounts of bypass flow were removed from each end of the vortex tube. During most of the tests, equal amounts of thru-flow were removed from each end of the vortex tube, at least for the initial flow setting. The only exception was for tests at 85 percent bypass involving a vortex-tube static pressure change. In this case, the weight flow in the thru-flow duct in which the control valve was installed was set at a weight flow approximately twice that of the other thru-flow duct. This setting was used to obtain a larger pressure change during the test than would be obtained otherwise.

A summary of the test configurations and operating conditions used for the tests is presented in Table VII.

Description of Test Results

The test results are presented in Figs. 36 through 43. In Fig. 36, the time history of the local partial pressure ratio is shown at 9 discrete radii for decreasing simulated-fuel weight flow (Fig. 36(a)) and for increasing simulated-fuel weight flow (Fig. 36(b)). The time histories of the volume-averaged simulated-fuel partial pressure (dashed lines) are also shown. In these tests the bypass ratio was constant at 46 percent. Figs. 37 through 39 present summaries of the time history of simulated-fuel containment at bypass ratios of 0, 46, and 85 percent. The average residence time, t_{\min} , of the buffer gas is shown in all figures.

The change in simulated-fuel flow rate resulting from control valve actuation is shown in the upper curves in Fig. 36. A step change in simulated-fuel flow rate was desired in these tests. However, the design of the simulated-fuel supply system in the high Reynolds number test facility is such that this was impossible. The simulated-fuel supply system has a relatively large volume and the carrier-gas supply system a relatively small flow rate; thus, when the control valve was partially closed (Fig. 36(a)) the simulated-fuel flow rate into the vortex tube decreased rapidly. However, the simulated-fuel duct pressure upstream of the control valve (initially at a low value, ~ 1.014 atm) increased slowly (to a final value, ~ 1.55 atm). This increased pressure caused an increase in simulated-fuel flow rate.

This increase was relatively slow because of the relatively long time-constant of the system.

When the control valve was actuated to a fully open position, as in Fig. 36(b), the pressure upstream of the control valve decreased rapidly. This caused an increase in the simulated-fuel flow rate followed by a slow decrease to the steady-state value as the duct pressure decreased to a new steady-state value.

The initial decrease in simulated-fuel partial pressure, or containment, when the simulated-fuel flow rate is increased (see Figs. 36(b), 37(b), 38(b) and 39(b)) is not fully understood. One possible explanation for the decrease may be that the rapid increase in simulated-fuel flow rate momentarily produces a significant disturbance in the vortex flow. This disturbance may cause more of the contained simulated-fuel to be lost than is gained by the increased inflow. Whatever the reason, it appears that the decrease in containment is accentuated with increasing bypass flow (compare Figs. 37(b), 38(b), and 39(b)).

Although the time history of simulated-fuel containment is similar for the three bypass ratios shown in Figs. 37, 38, and 39, there are differences in gain, initial response, and overshoot. These factors are discussed in more detail in the following subsection.

The response of the vortex flow to changes in vortex static pressure are shown in Figs. 40 through 43. The time history of the local simulated-fuel partial pressure for a bypass ratio of 46 percent is presented in Fig. 40. Again, the dashed lines in Fig. 40 indicate the time history of the volume-averaged simulated-fuel partial pressure. Figs. 41 through 43 present the integrated containment history for 0, 46, and 85 percent bypass, respectively.

In each case a nearly step-change in vortex static pressure was produced. The magnitude of the change in vortex static pressure depended on the amount of bypass flow; however, the rate of change (slope) of vortex static pressure was approximately the same. The initial response of the simulated-fuel containment ($d\%_F/dt$)₀ depends on the amount of bypass flow (compare Figs. 41, 42 and 43). It should also be noted that when there was an overshoot in the response of the vortex flow (e.g., Figs. 42 and 43), the overshoot was smoothly damped.

Analysis of Data and Comparison with Model Used in Engine Dynamics Simulation Program

The approach used in analyzing the data and relating it to the expected characteristics of the nuclear light bulb engine is discussed in this section. Basically, the approach was to first describe the test results in general form by fitting a transfer function to the data. This transfer function was then compared

with a transfer function describing the model presently used in the UNIVAC 1108 engine dynamics simulation program discussed in Ref. 17, particularly the initial rate of change of the amount of simulated-fuel contained in the vortex tube following a change in simulated-fuel flow rate and the gain of the system, i.e., the steady-state ratio of the change in simulated-fuel contained to the change in simulated-fuel flow rate.

In view of the difficulties encountered in describing the experimental results in general form, this analysis was limited to the experiments in which simulated-fuel flow rate was changed. Further analyses of these data can be made, and similar analyses can be conducted for the experiments in which the vortex static pressure was changed. This additional work will require more use of machine computation (particularly the PDP-6 parameter identification technique discussed below) than was possible within the scope of the present program.

General Transfer Function Describing Experimental Results

The first task in analyzing the data was to derive a general form for a linear transfer function that could be used to describe the dynamic response of the system. This was accomplished using the data in Figs. 37 through 39 as input to a parameter identification technique PDP-6 computer program developed by the Simulation Laboratory at UARL. The program takes any function of time as input and fits a specified form of transfer function, selecting the values of the parameters in the transfer function that minimize the root-mean-square error between the input function of time and the time-domain solution of the transfer function.

Referring to Figs. 37 through 39, for example, it is seen that the response characteristics in all tests are generally similar. When a step change in the simulated-fuel flow control valve position was made, the flow went through a large transient (a peak or a valley) and then asymptotically approached a new steady-state value. The associated change in the amount of simulated-fuel contained also went through an oscillatory transient and asymptotically approached a new steady-state value. Examination of Figs. 37 through 39 reveals that, although the general shapes of the responses are similar, the specific dynamic characteristics --- the frequency, damping, amount of overshoot, the steady-state gain, etc. --- were different when the simulated-fuel flow was decreased than when it was increased (compare Figs. 37(a) and (b), for example). Similarly, the specific dynamic characteristics appear to depend upon the amount of bypass flow (compare Figs. 37(b), 38(b) and 39(b)). This indicates that the coefficients of the governing differential equations, and hence the parameters in the transfer functions, depend upon the sign of the input and the amount of bypass. It is probable that they also depend upon the initial conditions (initial simulated-fuel flow rate and simulated-fuel stored), but insufficient data are available to determine this dependence.

It should be mentioned that the 15- to 20-percent changes in simulated-fuel flow rate in the experiments are probably much larger than the changes that would occur during normal operation of the full-scale nuclear light bulb engine. These large changes were necessary in the experiments to provide changes in the amount of simulated-fuel stored that were measurable with reasonable accuracy in the high Reynolds number test facility. The extent to which the transfer function parameters vary with initial conditions, amount of bypass, etc., cannot be determined from the measurements that were made.

The sketches in Fig. 44 will aid in defining terms used in the following discussion.

The equation used to approximate the response of simulated-fuel flow rate, δw_F , to a step change in valve area (see Fig. 44(a)) is

$$\delta w_F = \delta w_{F\infty} + \Delta w_{FOS} \cdot e^{-t/T} \quad (C-1)$$

where $\delta w_{F\infty}$ is the steady-state change, Δw_{FOS} is the overshoot, and T is the time at which the overshoot has decayed to 63 percent of its initial value. The Laplace transform of this equation is

$$\overline{\delta w_F} = \frac{\delta w_{F\infty}}{s} + \frac{T \cdot \Delta w_{FOS}}{1 + Ts} \quad (C-2)$$

or

$$\overline{\delta w_F} = \frac{\delta w_{F\infty}(1 + Ts) + T \cdot \Delta w_{FOS} \cdot s}{s(1 + Ts)} \quad (C-3)$$

From the parameter identification technique program, it was determined that a Laplace transform of the following form can be used to represent the response of simulated fuel contained to the step change in control valve area:

$$\overline{\delta w_F} = \frac{\delta w_{F\infty} \cdot k \cdot (s+a)(s+b)}{s(s+c)(s^2 + 2\zeta\omega_n s + \omega_n^2)} \quad (C-4)$$

The parameters k , a , b , c , d , ζ , and ω_n were computed such that the fits to the data in Figs. 37 through 39 had rms errors of at most 5.6 percent.

By taking the ratio of Eq. (C-4) to Eq. (C-3), the following general transfer function relating a change in simulated fuel contained to a change in simulated-fuel flow rate is obtained:

$$\frac{\overline{\delta W_F}}{\overline{\delta W_F}} = \frac{k \cdot (s+a)(s+b)(1+Ts)}{(s+c)(s^2 + 2\zeta\omega_n s + \omega_n^2)((1+Ts) + (\Delta W_{FOS}/\delta W_{F\infty}) \cdot Ts)} \quad (C-5)$$

The time-domain inverse transform of Eq. (C-5) is complex. Calculations of the dynamic response in the time domain are best handled on an analog computer.

There are, however, two useful limiting cases that can be derived from Eq. (C-5) by applying the initial-value and final-value theorems (Ref. 18). The initial slope of the response (as indicated in Fig. 44(b)) to a step input in simulated-fuel flow rate (i.e., $\overline{\delta W_F} = \delta W_{F\infty}/s$) is given by

$$\lim_{s \rightarrow \infty} s^2 \cdot \frac{\delta W_{F\infty}}{s} \cdot \frac{\overline{\delta W_F}}{\overline{\delta W_F}} \quad (C-6)$$

Evaluating the limit in Eq. (C-6), the initial slope is given by

$$(dW_F/dt)_0 = \frac{k \cdot \delta W_{F\infty}}{1 + (\Delta W_{FOS}/\delta W_{F\infty})} \quad (C-7)$$

Equation (C-7) indicates that the initial rate of change of simulated fuel contained is proportional to the steady-state change in simulated-fuel flow rate. Moreover, Eq. (C-7) indicates that larger overshoots in simulated-fuel flow rate (i.e., large values of $\Delta W_{FOS}/\delta W_{F\infty}$) reduce the initial rate of change.

The second limiting case is the final value of the change in simulated fuel stored for a step change in flow rate, $\overline{\delta W_F} = \delta W_{F\infty}/s$. Using the final-value theorem,

$$\lim_{s \rightarrow 0} s \cdot \frac{\delta W_{F\infty}}{s} \cdot \frac{\overline{\delta W_F}}{\overline{\delta W_F}} \quad (C-8)$$

which yields

$$\delta W_{F\infty} = \frac{k \cdot a \cdot b \cdot \delta W_{F\infty}}{c \omega_n^2} \quad (C-9)$$

This indicates, as expected on the basis of previous steady-state two-component gas-vortex containment tests, that the final change in the amount of simulated fuel contained is directly proportional to the final change in simulated-fuel flow rate.

Transfer Function Describing Model in Engine Dynamics Simulation

The open-loop transfer function governing changes in the amount of fuel contained in the engine, as used in the engine dynamics simulation computer program (Ref. 17), is

$$\frac{\overline{\delta W_F}}{\overline{\delta W_{F_0}}} = \frac{2/\lambda_{F_0}}{(1 + (2/\lambda_{F_0})s)} \quad (C-10)$$

where λ_{F_0} is the value of the fuel decay constant and has the dimensions sec^{-1} (Ref. 17). Equation (C-10) results from assuming small perturbations and is a simplified representation of the situation occurring in the engine. No feedback is included; that is, none of the compensating effects that occur in the engine due to pressure changes in the cavity, due to changes which are fed back to the fuel valve from the neutron flux and reactor period sensors, etc., are included. In Ref. 17, a value of 0.25 sec^{-1} is used for λ_{F_0} .

The time-domain inverse transform of Eq. (C-10) for a step change in fuel flow rate ($\overline{\delta W_F} = \delta W_{F\infty}/s$) is

$$\delta W_F = \frac{2 \cdot \delta W_{F\infty}}{\lambda_{F_0}} \left(1 - e^{-t/(2/\lambda_{F_0})} \right) \quad (C-11)$$

which is non-oscillatory and asymptotically approaches the following steady-state value for the change in fuel contained:

$$\delta W_{F\infty} = \frac{2 \cdot \delta W_{F\infty}}{\lambda_{F_0}} \quad (C-12)$$

The initial rate of change of fuel contained is simply

$$(dW_F/dt)_0 = \delta W_{F\infty} \quad (C-13)$$

Equations (C-12) and (C-13) indicate that, in the engine dynamics simulation model, both the final change in fuel contained and the initial rate of change of fuel contained are proportional to the step change in fuel flow rate.

Comparison of Transfer Functions

It is of interest to compare the two transfer functions ---- the one derived from the experimental data (Eq. (C-5)) and the one representing the model in the

dynamics program (Eq. (C-10)). The following table makes this comparison for the case where step changes in fuel flow rate are made in both systems:

<u>Characteristics</u>	<u>Transfer Function Describing Data</u>	<u>Transfer Function in Engine Dynamics Model</u>
General Response	Heavily Damped Oscillation	Damped Exponential
Initial Response, $(d\mathcal{W}_F/dt)_0$	$\frac{k \cdot \delta w_{F\infty}}{1 + (\Delta w_{FOS}/\delta w_{F\infty})}$	$\delta w_{F\infty}$
Steady-State Gain, $\delta \mathcal{W}_F / \delta w_{F\infty}$	$\frac{k \cdot a \cdot b}{c \omega_n^2}$	$2 / \lambda_{F_0} = 8$

Referring first to the general response characteristics, it is probable that the damped exponential is a satisfactory approximation for use in the engine dynamics studies, even though the transfer function describing the data indicates a heavily damped oscillation. Figures 37(a), 38(a) and 39(a), which are for step decreases in simulated-fuel flow rate with major overshoots, tend to indicate that the oscillations are relatively minor when such changes occur. Figure 37(b), which is for a step increase with a major overshoot, shows a far greater oscillatory characteristic than is shown in the data at higher bypass ratios (Figs. 38(b) and 38(c)). Thus, with the possible exception of large increases in fuel flow rate at zero bypass, the form of the transfer function representing the model is probably adequate.

The initial responses (initial rates of change of fuel contained) of both the transfer function describing the data and that representing the model are proportional to the height of the step in fuel flow rate, $\delta w_{F\infty}$. There are substantial differences in the magnitudes of the initial responses, however. For example, using the values $k = 12.458$, $\delta w_{F\infty} = 0.001$ and $\Delta w_{FOS}/\delta w_{F\infty} = 2.2$ from the case of 46-percent bypass shown in Fig. 38(b), one calculates a value of $(d\mathcal{W}_F/dt)_0 = 0.004$ for the transfer function describing the data, compared with 0.001 for the transfer function representing the model. This implies that the model is conservative --- the initial response in the engine dynamics simulation program is slower than the response indicated in the experiments.

Finally, the steady-state gains can be compared. The gains used currently in the model appear to be about twice that apparent in the experiments. Using the 46-percent bypass case as an example ($k = 12.458$, $a = 0.352$, $b = 1.7095$, $c = 4.4689$ and $\omega_n = 0.4299$), one calculates $\delta \mathcal{W}_{F\infty} / \delta w_{F\infty} = 3.91$ using Eq. (C-9). For $\lambda_{F_0} = 0.25$, the current model gives $\delta \mathcal{W}_{F\infty} / \delta w_F = 8.0$. The engine dynamics program has been run with values of λ_{F_0} from 0.05 to 0.25, corresponding to gains from 40 to 8, with no apparent adverse effects occurring at either end of the range (Ref. 17). It would be relatively easy to investigate even lower gains at a future date.

APPENDIX D

TESTS OF VORTEX-TUBE CONFIGURATION
WITH REFLECTING PERIPHERAL WALL*

A series of tests was conducted in which a metallic reflecting wall was located around the plasma region. These tests were exploratory and their objectives were to determine the average reflectivity of the wall and to verify that a metallic-wall reflector is electrically compatible with an r-f electromagnetic field environment. A sketch of the configuration employed in the tests is shown in Table VIII. The reflector was located between the two fused silica tubes (see Fig. 2(a)) and was water cooled. The reflector consists of a 1.4-in.-dia by 2.8-in.-long copper cylinder having a 0.4-in.-wide longitudinal slot. The reflector was designed with the slot to prevent the reflector from shielding the r-f magnetic field from the discharge region. The reflecting inner-surface consisted of a layer of vacuum-deposited silver over-coated with silicon monoxide.

Three separate tests were necessary to determine the average reflectivity and the r-f power deposited in the reflector. The flow and power conditions for the tests are given in Table VIII. The results indicate 3.1 kw was radiated through the peripheral-wall coolant in the test with no reflector present (Test No. 1) and 1.0 kw was deposited in the peripheral-wall coolant fluid. With the reflector present (Test No. 2), the power deposited in the peripheral-wall coolant increased to 2.2 kw. The results of Test No. 3 (see Table VIII) indicate that 0.65 kw of the 2.2 kw can be attributed to direct r-f heating of the copper reflector-body. Thus, in Test No. 2 the amount of power deposited in the peripheral-wall coolant due to absorption of radiation by the reflector was 0.55 kw (i.e., 2.2 kw minus 1.65 kw = 0.55 kw). The remaining 2.55 kw (i.e., 3.1 kw minus 0.55 kw) of radiation was assumed to have escaped the test chamber through the 0.4-in.-wide opening in the reflector. Based on the area of the opening, a radiation flux at the opening of 2.3 kw/in.² was calculated. The flux at this location when no reflector was used was 0.25 kw/in.². Thus, use of this reflector resulted in a radiation flux at the reflector opening about nine times that with no reflector present. The test results also indicate the average reflectivity of the silvered surface was about 80 percent, based on the measured values of the radiation incident on the reflector and the radiation deposited in the peripheral-wall coolant fluid.

The results of these tests demonstrate that simple metallic reflecting surfaces can be employed in an r-f environment to increase the local radiation flux from the test chamber.

*Tests conducted by John S. Kendall

TABLE I
TEST CONFIGURATIONS AND OPERATING CONDITIONS FOR HEATED VORTEX TESTS
UARL 80-KW R-F INDUCTION HEATER

Configuration (See Note for Abbreviations)	EW Ar No Xe	EW Ar Premixed Xe	EW Ar CL Xe	PW Ar No Xe	PW Ar CL Xe
<u>Figures in which Data are Presented</u>	7(a)	8	9	7(b), 29	10, 31
<u>Flow Conditions</u>					
Buffer Gas					
Injection flow rate, w_B -lb/sec	Argon 5.0×10^{-3}	Argon 3.7×10^{-3}	Argon 5.0×10^{-3}	Argon 4.4×10^{-3}	Argon 4.4×10^{-3}
Injection velocity, v_j -ft/sec	440	360	440	280	280
Injection Reynolds number, Re_j	1.98×10^5	1.50×10^5	1.98×10^5	1.25×10^5	1.25×10^5
Vortex pressure, P_1 -atm	1.3	1.2	1.3	1.3	1.3
Simulated Fuel					
Injection flow rate, w_F -lb/sec	---	Xenon 6.7×10^{-5}	Xenon 2.2×10^{-3}	---	Xenon 2.2×10^{-3}
Injection velocity, v_F -ft/sec	0	---	115	0	115
Simulated-fuel-to-buffer-gas weight flow ratio, w_F/w_B	0	0.018	0.44	0	0.50
Simulated-fuel-to-buffer-gas volume flow ratio, Q_F/Q_B	0	0.0055	0.135	0	0.153
<u>Power Conditions</u>					
Power deposited in plasma, Q_H -kw	12.5	7.2	10.9	9.6	7.9
Power radiated from plasma, Q_R -kw	3.1	1.6	2.6	1.6	1.3
D-C plate power, Q_{PC} -kw	33.5	24.0	28.0	28.0	24.3
Reflected plasma impedance, Z_p -ohms	2120	1300	1220	1670	1180
R-F during frequency, f-mHz	7.25	7.25	7.25	7.25	7.25

Note: EW Ar - Argon injected tangentially through end-wall injectors (see Fig. 2(a)).
 PW Ar - Argon injected tangentially through peripheral-wall injectors (see Fig. 2(b)).
 No Xe - No xenon used.
 Premixed Xe - Xenon mixed with argon upstream of vortex.
 CL Xe - Xenon injected axially at vortex centerline (see Fig. 2).

TABLE II
TEST CONFIGURATIONS AND OPERATING CONDITIONS FOR
UNHEATED TESTS IN 10-IN.-DIA VORTEX TUBE

Peripheral-Wall Buffer-Gas Injection; $A_{B,j} = 0.84$ sq in.
Peripheral-Wall Simulated-Fuel Injection
Air Buffer Gas; Nitrogen/Iodine Simulated-Fuel

Figures in Which Data Are Presented	14, 15	14	14	15	15	15	21	22(a)	22(b)	22(c)	23
Buffer-gas weight flow, w_B -lb/sec	3.6×10^{-2}	3.6×10^{-2}	3.6×10^{-2}	3.9×10^{-2}	3.5×10^{-2}	3.6×10^{-2}	3.6×10^{-2}	3.5×10^{-2}	3.6×10^{-2}	3.9×10^{-2}	3.6×10^{-2}
Injection Reynolds number, Re_j	1.5×10^5	1.5×10^5	1.5×10^5	1.7×10^5	1.5×10^5	1.5×10^5	1.6×10^5	1.5×10^5	1.5×10^5	1.7×10^5	1.6×10^5
Radial Reynolds number, Re_r	120	120	184	83	184	58	121	184	120	83	58 → 184
Bypass ratio, percent	48	48	48	*84	*0	*96	48	0	48	84	*0 → 96
Simulation-fuel weight flow, w_F -lb/sec	6.9×10^{-3}	6.9×10^{-3}	6.9×10^{-3}	6.7×10^{-3}	6.7×10^{-3}	6.9×10^{-3}	6.9×10^{-3}	6.7×10^{-3}	6.9×10^{-3}	6.7×10^{-3}	6.7×10^{-3}
Simulated-fuel injection area, $A_{F,j}$ -sq in.	0.731	0.436	0.146	0.877	0.146 → 0.877	0.877	0.585	0.146 → 0.877	0.146 → 0.877	0.146 → 0.877	0.292
Buffer-gas-to-simulated-fuel weight flow ratio, w_B/w_F	5.2	5.2	5.2	5.2	5.2	5.0	5.2	5.2	5.2	5.8	5.4
Simulated-fuel to buffer-gas injection velocity ratio, v_F/v_j	*0.22	*0.37	*1.1	0.20	*0.22	0.24	0.28	*0.184 → 1.13	*0.184 → 1.10	*0.164 → 1.03	0.54
Simulated-fuel-to-buffer gas volume flow ratio, Q_F/Q_B	0.195	0.195	0.195	0.197	0.197	0.206	0.193	0.197	0.195	0.176	0.186

* Denotes primary test variable

TABLE III
TEST CONFIGURATIONS AND OPERATING CONDITIONS FOR
UNHEATED TESTS IN 10-IN.-DIA VORTEX TUBE

Peripheral-Wall Buffer-Gas Injection; $A_{B,j} = 0.84$ sq in.
End-Wall Simulated-Fuel Injection at $r/r_1 = 0.8$

Figures in which data are presented	16, 17	16	16	17	17	17	21	22(a)	22(b)	22(c)	23	24	24
Buffer gas	Air	Air	Air	Air	Air	Air	Air	Air	Air	Air	Air	Air	Air
Buffer-gas weight flow, \dot{w}_B -lb/sec	3.5×10^{-2}	3.5×10^{-2}	3.5×10^{-2}	3.5×10^{-2}	3.5×10^{-2}	3.5×10^{-2}	3.6×10^{-2}	3.5×10^{-2}	3.5×10^{-2}	3.9×10^{-2}	3.5×10^{-2}	5.4×10^{-1}	3.4×10^{-2}
Injection Reynolds number, Re_j	1.5×10^5	1.5×10^5	1.5×10^5	1.5×10^5	1.5×10^5	1.5×10^5	1.6×10^5	1.5×10^5	1.5×10^5	1.7×10^5	1.5×10^5	2.5×10^5	1.5×10^5
Radial Reynolds number, Re_r	124	124	124	83	59	121	121	188	124	83	59	45	99
Bypass ratio, percent	48	48	48	*82	*96	49	49	0	48	83	*0	*91	96
Simulated fuel	Nitrogen/ Iodine	Nitrogen/ Iodine	Nitrogen/ Iodine	Nitrogen/ Iodine	Nitrogen/ Iodine	Nitrogen/ Iodine	Nitrogen/ Iodine	Nitrogen/ Iodine	Nitrogen/ Iodine	Nitrogen/ Iodine	Nitrogen/ Iodine	Nitrogen/ Iodine	Nitrogen/ Iodine
Simulated-fuel weight flow, \dot{w}_F -lb/sec	7.1×10^{-3}	7.1×10^{-3}	7.1×10^{-3}	7.1×10^{-3}	7.1×10^{-3}	7.1×10^{-3}	7.1×10^{-3}	7.1×10^{-3}	7.1×10^{-3}	7.1×10^{-3}	7.1×10^{-3}	1.2×10^{-3}	7.2×10^{-3}
Simulated-fuel injection area, $A_{F,j}$ -sq in.	0.871	0.436	0.145	0.871	0.871	0.581	0.581	0.145 1.16	0.145 1.16	0.145 1.16	0.290	1.16	0.29
Buffer-gas-to-simulated-fuel weight flow ratio, \dot{w}_B/\dot{w}_F	5.0	5.0	5.0	5.6	4.9	5.0	5.0	5.0	5.0	5.6	5.0	45.0	4.6
Simulated-fuel-to-buffer-gas injection velocity ratio, v_F/v_j	*0.20	*0.38	*1.18	0.17	0.21	0.30	0.30	*0.133 1.17	*0.133 1.17	*0.129 1.02	0.57	0.51	0.41
Simulated-fuel-to-buffer-gas volume flow ratio, \dot{Q}_F/\dot{Q}_B	0.203	0.199	0.204	0.179	0.217	0.208	0.208	0.201	0.199	0.179	0.199	0.702	0.212

*Denotes primary test variable.

TABLE IV

TEST CONFIGURATIONS AND OPERATING CONDITIONS FOR
UNHEATED TESTS IN 10-IN.-DIA VORTEX TUBE

Peripheral-Wall Buffer-Gas Injection; $A_{B,j} = 0.84$ sq in.
End-Wall Simulated-Fuel Injection at $r/r_1 = 0.8$
Simulated-Fuel Weight Flow; $w_F = 7.1 \times 10^{-3}$ lb/sec
Air Buffer Gas; Nitrogen/Iodine Simulated Fuel

Figures in which data are presented	18, 19	18	18	19	19	19	19	21	22(a)	22(b)	22(c)	23	27
Buffer-gas weight flow, w_B -lb/sec	3.6×10^{-2}	3.6×10^{-2}	3.6×10^{-2}	4.0×10^{-2}	3.5×10^{-2}	3.6×10^{-2}	3.6×10^{-2}	3.6×10^{-2}	3.6×10^{-2}	3.6×10^{-2}	4.0×10^{-2}	3.6×10^{-2}	3.6×10^{-2}
Injection Reynolds number, Re_j	1.6×10^5	1.6×10^5	1.6×10^5	1.7×10^5	1.5×10^5	1.6×10^5	1.6×10^5	1.6×10^5	1.6×10^5	1.6×10^5	1.7×10^5	1.6×10^5	1.6×10^5
Radial Reynolds number, Re_r	123	123	123	84	59	121	186	121	186	123	84	186	125
Bypass ratio, percent	48	48	48	*82	*96	47	0	47	0	48	83	*90	47
Simulated-fuel injection area, sq in.	0.871	0.436	0.145	0.871	0.871	0.581	0.871	0.581	0.871	0.871	0.871	0.290	0.290
Buffer-gas-to-simulated-fuel weight flow ratio, w_B/w_F	5.1	5.1	5.1	5.6	4.9	5.1	5.1	5.1	5.1	5.1	5.6	5.1	5.1
Simulated-fuel-to-buffer-gas injection velocity ratio, v_F/v_j	*0.18	*0.35	*1.10	0.17	0.19	0.28	*0.184	0.28	*0.184	*0.184	*0.169	0.56	0.56
Simulated-fuel-to-buffer-gas volume flow ratio, Q_F/Q_B	0.191	0.180	0.191	0.176	0.199	0.191	0.191	0.191	0.191	0.180	0.176	0.193	0.193

*Denotes primary test variable.

TABLE V

TEST CONFIGURATIONS AND OPERATING CONDITIONS FOR UNHEATED TESTS
IN 10-IN.-DIA VORTEX TUBE

Peripheral-Wall Buffer-Gas Injection; $A_{Bj} = 0.84$ sq in.
Centerline Simulated-Fuel Injection
Air Buffer Gas
Nitrogen/Iodine Simulated Fuel

Figures in which data are presented	20, 23	20, 21 23, 27	20, 23
Buffer-gas weight flow, w_B -lb/sec	3.5×10^{-2}	3.8×10^{-2}	3.8×10^{-2}
Simulated-fuel weight, flow w_F -lb/sec	7.5×10^{-3}	7.5×10^{-3}	7.5×10^{-3}
Simulated-fuel injection area, sq in.	0.29	0.29	0.29
Buffer-gas-to-simulated-fuel weight flow ratio, w_B/w_F	4.6	5.1	4.3
Injection Reynolds number, Re_j	1.5×10^5	1.7×10^5	1.4×10^5
Radial Reynolds number, Re_r	189	121	58
Bypass ratio, percent	0	45	95
Simulated-fuel-to-buffer-gas injection velocity ratio, v_F/v_j	0.62	0.57	0.67
Simulated-fuel-to-buffer-gas volume flow ratio, Q_F/Q_B	0.215	0.197	0.230

TABLE VI

TEST CONFIGURATIONS AND OPERATING CONDITIONS FOR UNHEATED TESTS
IN 1.26-IN.-DIA VORTEX TUBE

Peripheral-Wall Buffer-Gas Injection - $AB_j = 1.72 \times 10^{-2}$ sq in.
Argon Buffer Gas
Argon/Bromine Simulated Fuel

Figures in which data are presented	22(b), 23, 25	22(c) 23, 25	22(a), 23, 26, 31	22(b), 23, 26	22(c) 23, 26
Buffer-gas weight flow, w_B -lb/sec	4.5×10^{-3}	5.0×10^{-3}	5.0×10^{-3}	4.5×10^{-3}	5.0×10^{-3}
Injection Reynolds number, Re_j	1.4×10^5	1.5×10^5	1.5×10^5	1.3×10^5	1.5×10^5
Radial Reynolds number, Re_r	118	86	209	121	89
Bypass flow, percent	44	69	0	44	69
Simulated-fuel injection configuration	EW $r/r_1 = 0.5$	EW $r/r_1 = 0.5$	Centerline	Centerline	Centerline
Simulated-fuel weight flow, w_F -lb/sec	0.9×10^{-3}	0.9×10^{-3}	1.0×10^{-3}	1.0×10^{-3}	1.0×10^{-3}
Simulated-fuel injection area, sq in.	5.0×10^{-3}	5.0×10^{-3}	6.9×10^{-3}	6.9×10^{-3}	6.9×10^{-3}
Buffer-gas-to-simulated-fuel weight flow ratio, w_B/w_F	5.0	5.6	5.0	4.6	5.0
Simulated Fuel-to-buffer injection velocity ratio, v_F/v_j	0.61	0.52	0.39	0.46	0.39
Simulated Fuel-to-buffer volume flow ratio, Q_F/Q_B	0.18	0.15	0.16	0.18	0.16

Note: EW - Injection from end wall

TABLE VII

TEST CONFIGURATIONS AND OPERATING CONDITIONS FOR NONSTEADY-STATE
UNHEATED TESTS IN 10-IN.-DIA VORTEX TUBE

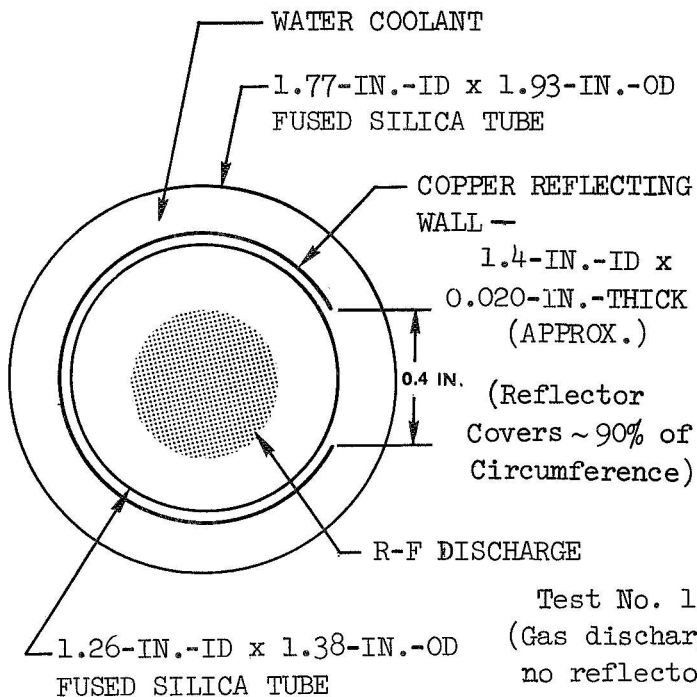
Peripheral-Wall Buffer-Gas Injection; $A_{B,j} = 0.84$ sq in.
End-Wall Simulated-Fuel Injection at $r/r_1 = 0.8$; $A_{F,j} = 0.436$ sq in.
Air Buffer Gas; Nitrogen/Iodine Simulated Fuel

Figures in which data are presented	36, 38	37	39	40, 42	41	43
Buffer-gas weight flow, w_B -lb/sec	3.6×10^{-2}	3.6×10^{-2}	3.6×10^{-2}	3.3×10^{-2}	2.9×10^{-2}	3.5×10^{-2}
Injection Reynolds number, Re_j	1.6×10^5	1.6×10^5	1.6×10^5	1.4×10^5	1.3×10^5	1.5×10^5
Radial Reynolds number, Re_r	123	192	84	112	163	74
Bypass ratio, percent	46	0	85	46	0	85
Vortex peripheral-wall static pressure, P_1 -atm	0.935	0.932	0.938	*0.951 0.959	*0.951 0.969	*0.950 0.956
Simulated-fuel weight flow, w_F -lb/sec	*6.3 $\times 10^{-3}$	*6.3 $\times 10^{-3}$	*5.7 $\times 10^{-3}$	7.4 $\times 10^{-3}$	8.0 $\times 10^{-3}$	6.8 $\times 10^{-3}$
Buffer-gas-to-simulated-fuel weight flow ratio, w_B/w_F	5.0	5.1	5.5	4.4	3.6	5.2
Simulated-fuel-to-buffer-gas injection velocity ratio, v_F/v_j	0.29	0.29	0.26	0.35	0.37	0.32
Simulated-fuel-to-buffer-gas volume flow ratio, Q_F/Q_B	0.178	0.176	0.162	0.184	0.194	0.166
Secondary flow parameter, β_t (See Ref. 12)	39.0	25.3	58.8	39.0	24.9	58.4

*Denotes primary test variable.

TABLE VIII

RESULTS OF TESTS OF CONFIGURATION
WITH REFLECTING PERIPHERAL WALL
(See Appendix D for Discussion)

End-View of Test ConfigurationTest Conditions

Gas	Argon
Injection weight flow, lb/sec	4.9×10^{-3}
Chamber pressure, atm	1.2
Heater plate voltage, kv	6.2
Heater plate current, amp	5.9
Heater frequency, mHz	7.25
Peak-to-peak coil voltage, kv	13.9

Test No. 1
(Gas discharge -
no reflector)

Test No. 2
(Gas discharge -
with reflector)

Test No. 3
(R-F only -
with reflector)

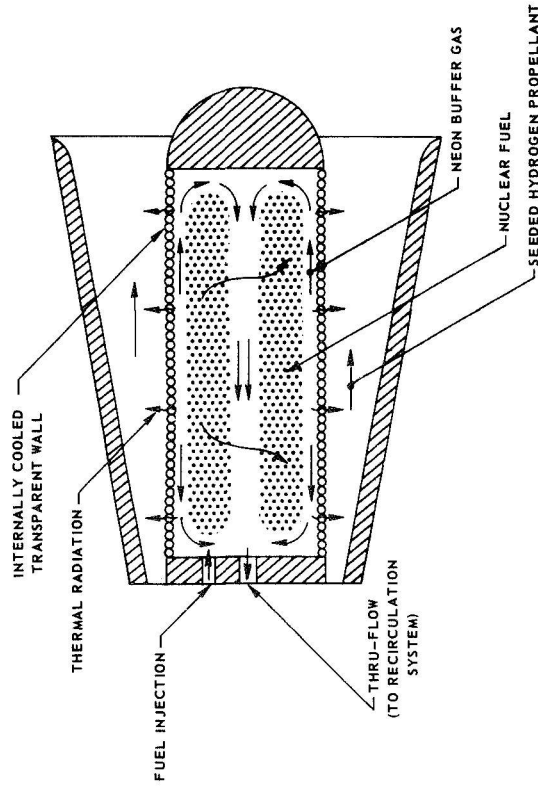
Power Dissipation

Peripheral-wall coolant, kw	1.0	2.2	0.65
End-wall coolant, kw	5.3	5.3	--
Injection-probe coolant, kw	4.4	4.4	--
Radiated power, kw	3.1	*	--
Total power, kw	13.8	11.9	0.65

*Emitted radiation not measured in this test.

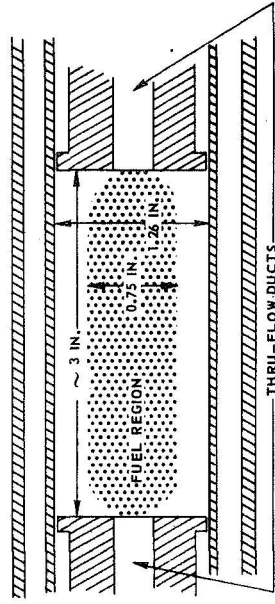
COMPARISON OF NUCLEAR LIGHT BULB UNIT CAVITY WITH VORTEX TUBES USED IN TESTS

(a) UNIT CAVITY OF NUCLEAR LIGHT BULB ENGINE



(c) 1.26-IN.-DIA VORTEX TUBE
(USED IN HEATED TESTS AND SOME UNHEATED TESTS)

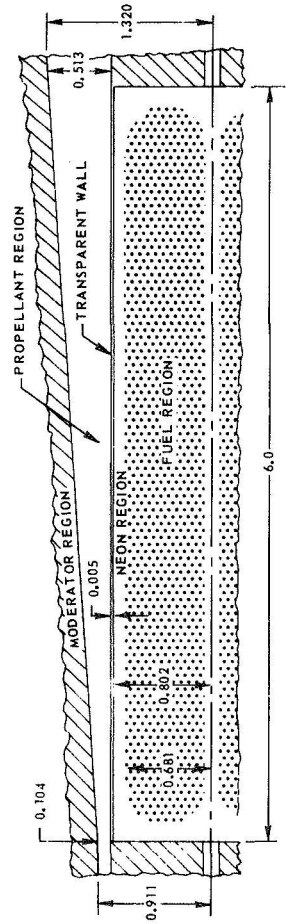
SEE FIG. 2 FOR DETAILS OF INJECTION CONFIGURATIONS



(b) DIMENSIONS OF UNIT CAVITY IN REFERENCE ENGINE

ALL DIMENSIONS IN FT

COMPLETE ENGINE IS COMPOSED OF A SEVEN-UNIT-CAVITY CLUSTER



(d) 10-IN.-DIA VORTEX TUBE (USED IN UNHEATED TESTS)

SEE FIGS. 4 AND 5 FOR DETAILS
OF INJECTION CONFIGURATIONS

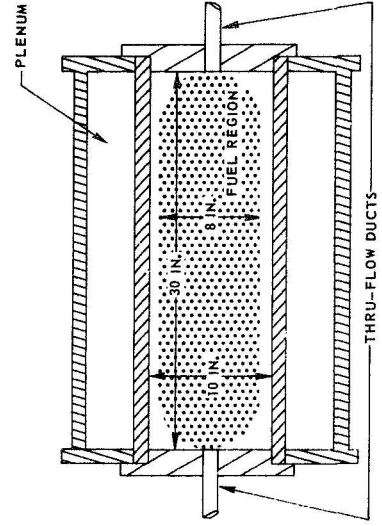
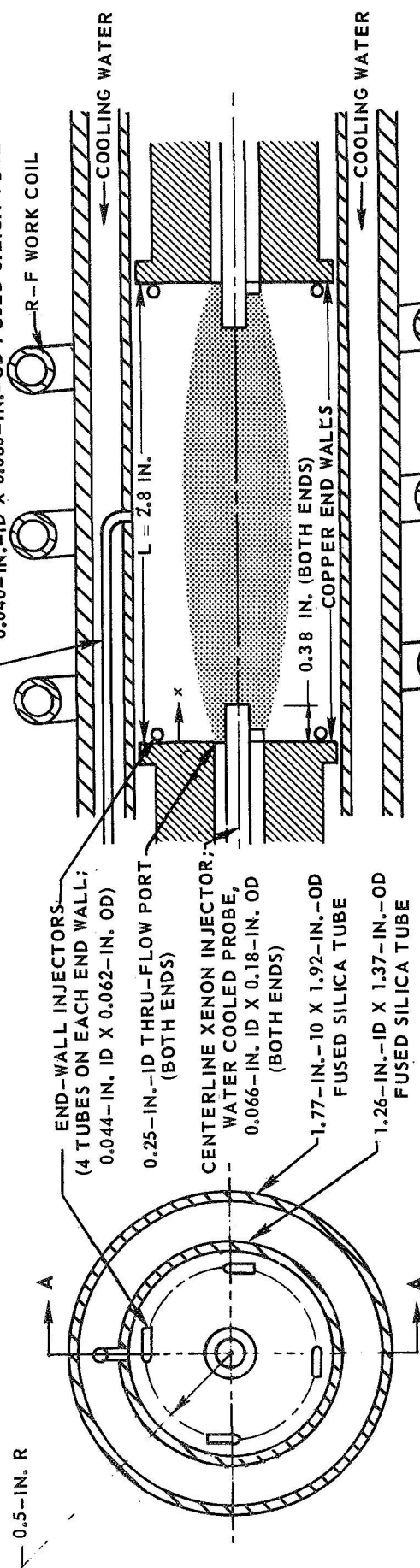


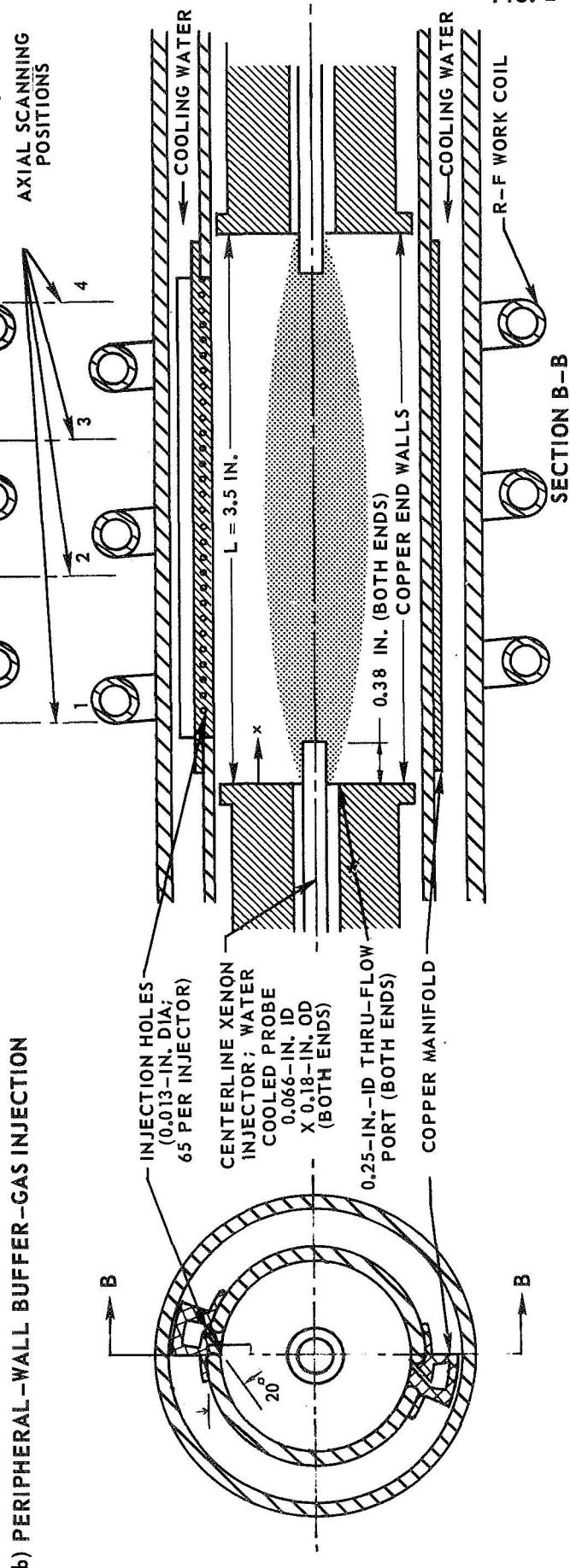
FIG. 1

SKETCHES OF VORTEX TUBES USED IN 80-KW R-F HEATER TESTS SHOWING INJECTION SYSTEMS

(a) END-WALL BUFFER-GAS INJECTION

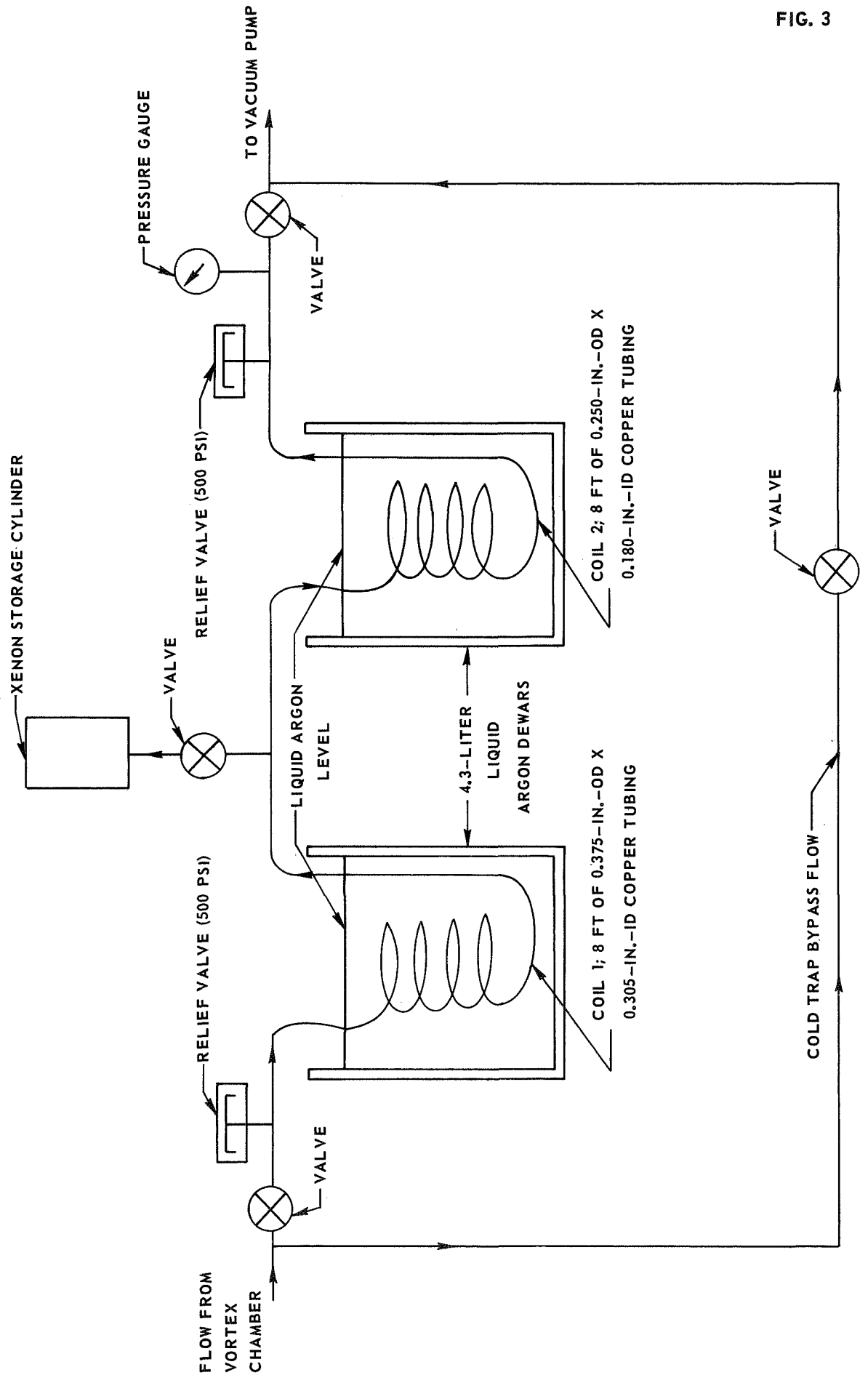


(b) PERIPHERAL-WALL BUFFER-GAS INJECTION



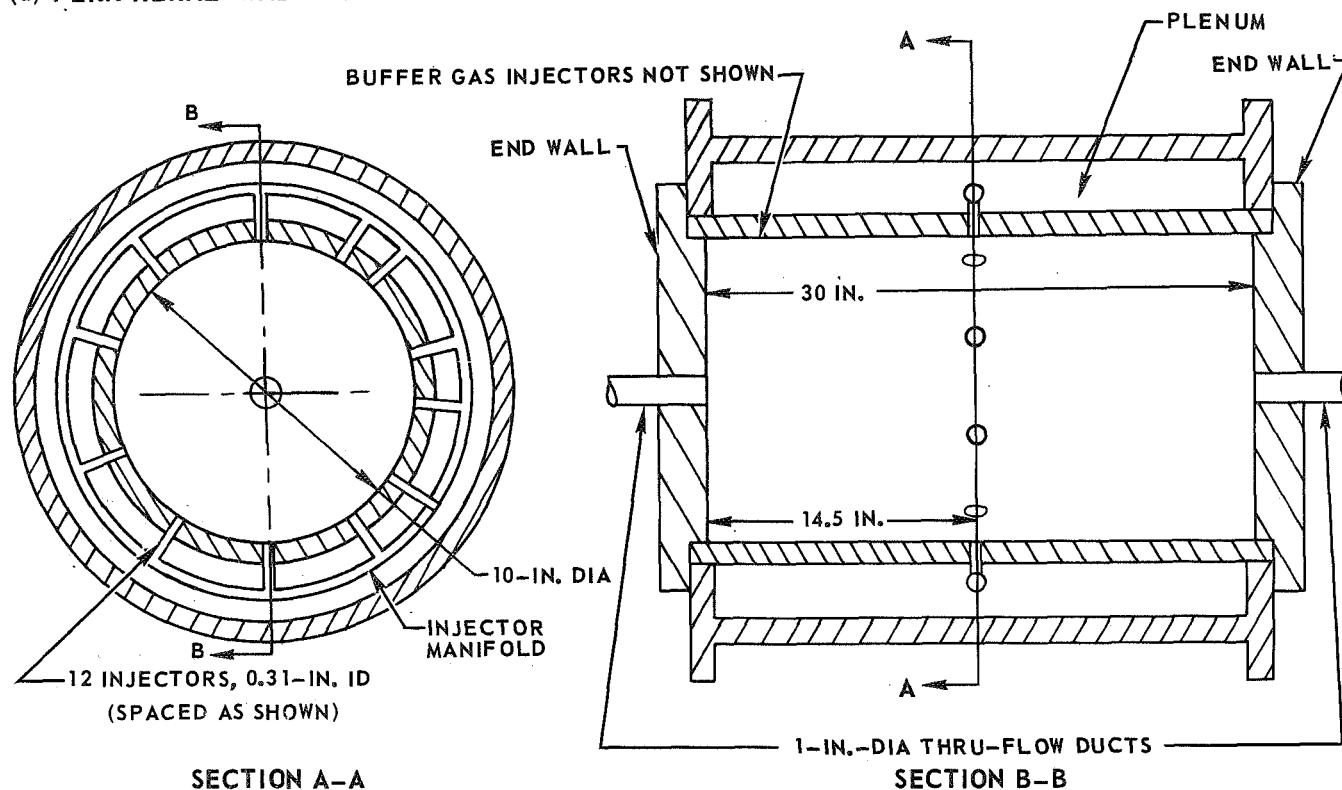
SCHEMATIC DIAGRAM OF XENON COLD TRAP FOR 80-KW R-F HEATER TESTS

SEE TEXT FOR DESCRIPTION OF OPERATION

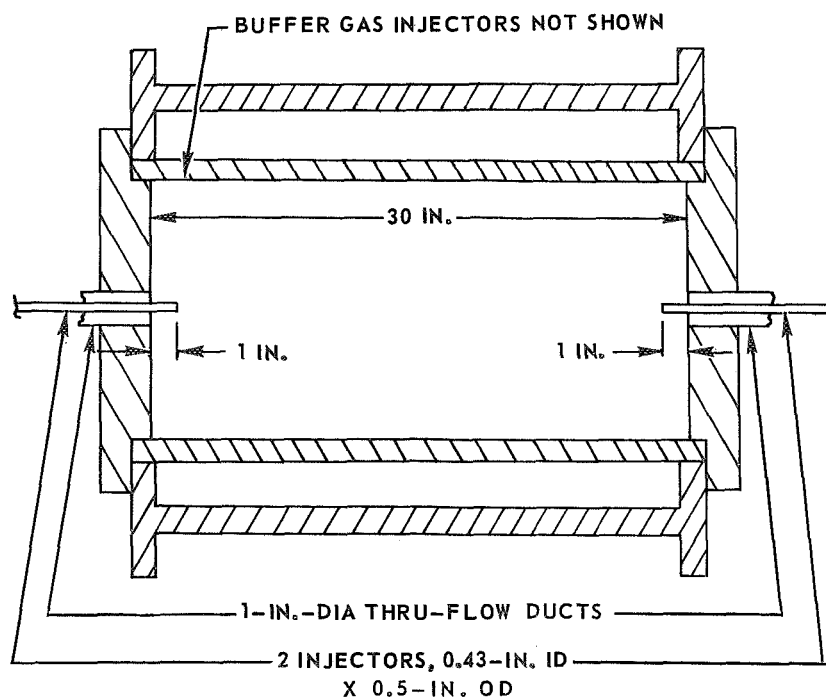


PERIPHERAL-WALL AND CENTERLINE SIMULATED-FUEL INJECTION CONFIGURATIONS FOR TESTS IN HIGH REYNOLDS NUMBER TEST FACILITY

(a) PERIPHERAL-WALL SIMULATED-FUEL INJECTION

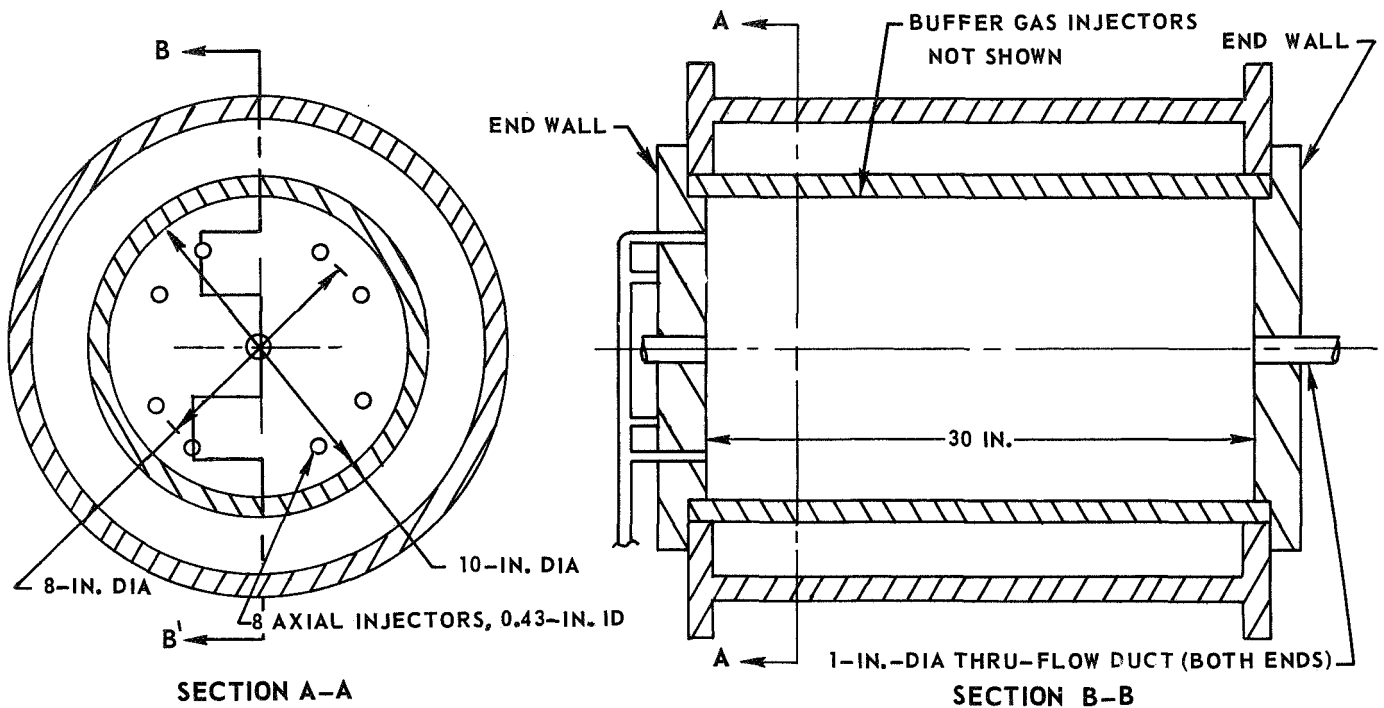


(b) CENTERLINE SIMULATED-FUEL INJECTION

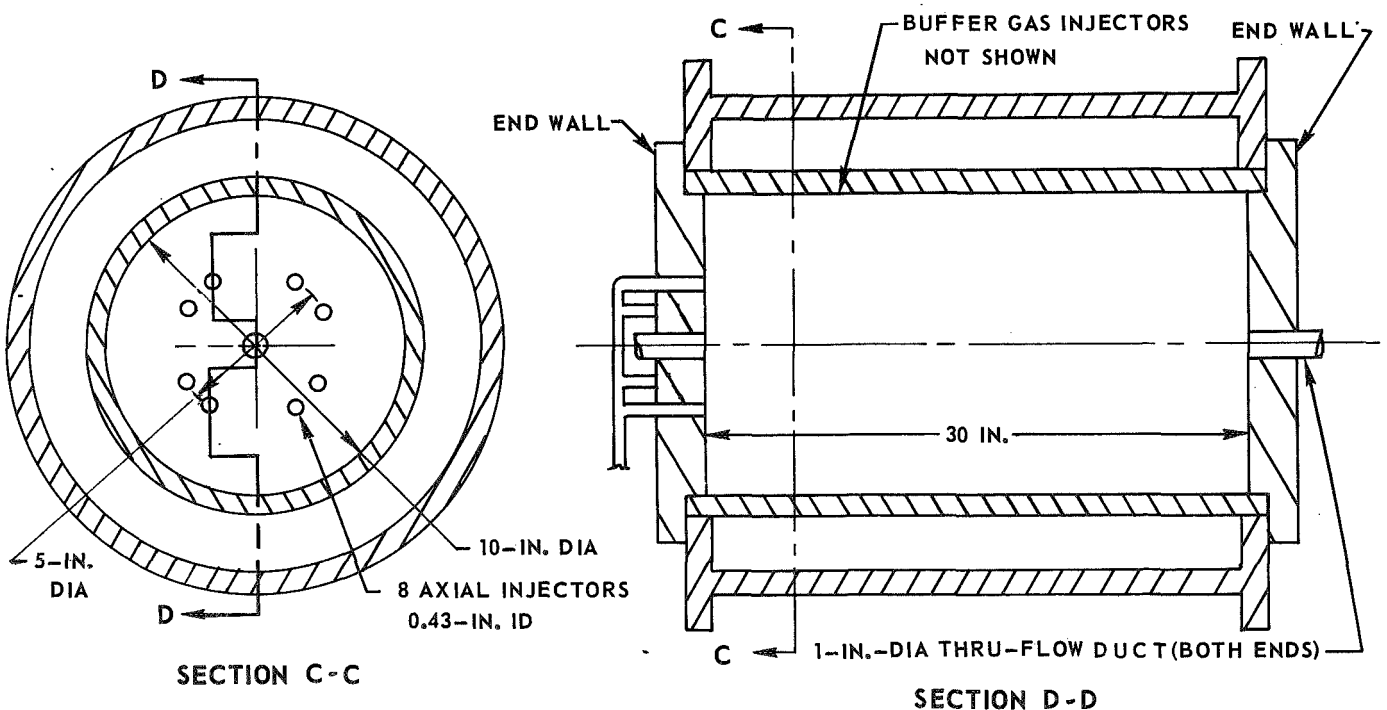


END-WALL SIMULATED-FUEL INJECTION CONFIGURATIONS FOR TESTS IN HIGH REYNOLDS NUMBER TEST FACILITY

(a) END-WALL SIMULATED-FUEL INJECTION AT $r/r_1 = 0.8$

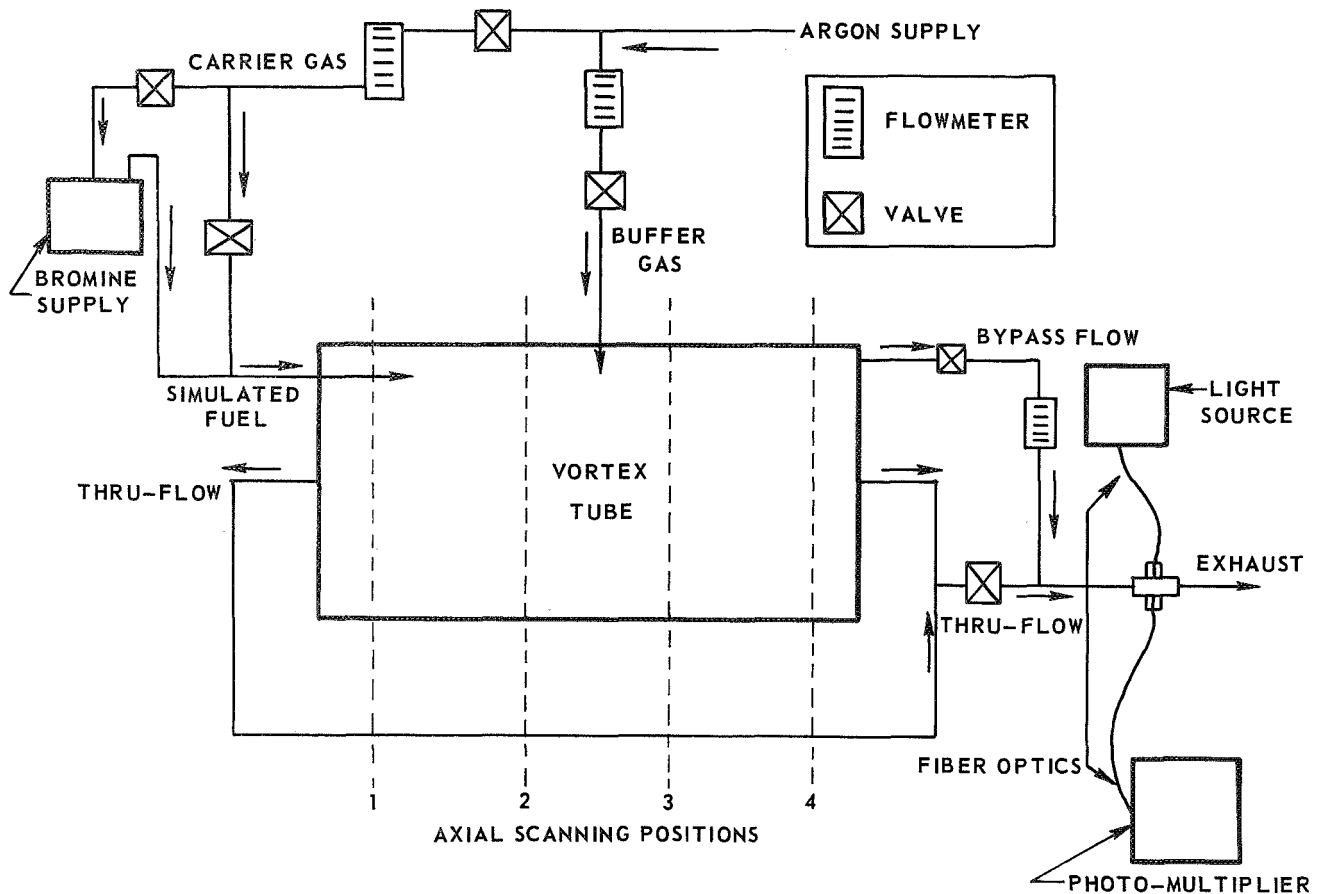


(b) END-WALL SIMULATED-FUEL INJECTION AT $r/r_1 = 0.5$

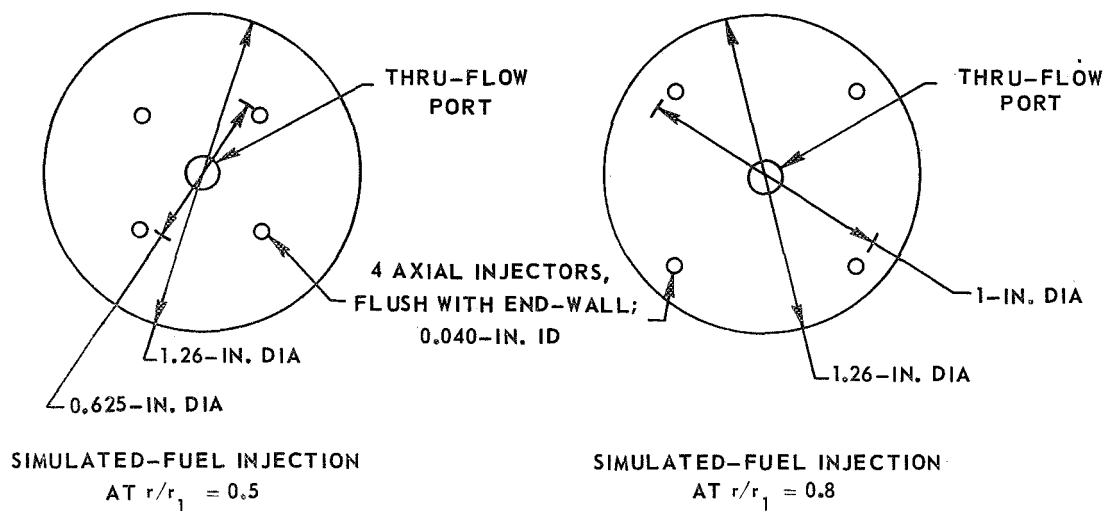


GEOMETRIES USED FOR UNHEATED VORTEX TESTS WITH 1.26-IN.-ID VORTEX TUBE

(a) SCHEMATIC DIAGRAM OF TEST ASSEMBLY



(b) END-WALL SIMULATED-FUEL INJECTION CONFIGURATIONS



RADIAL DISTRIBUTIONS OF TEMPERATURE IN AN ARGON PLASMA VORTEX

AT 1.3 ATM PRESSURE IN 1.26-IN.-DIA VORTEX TUBE

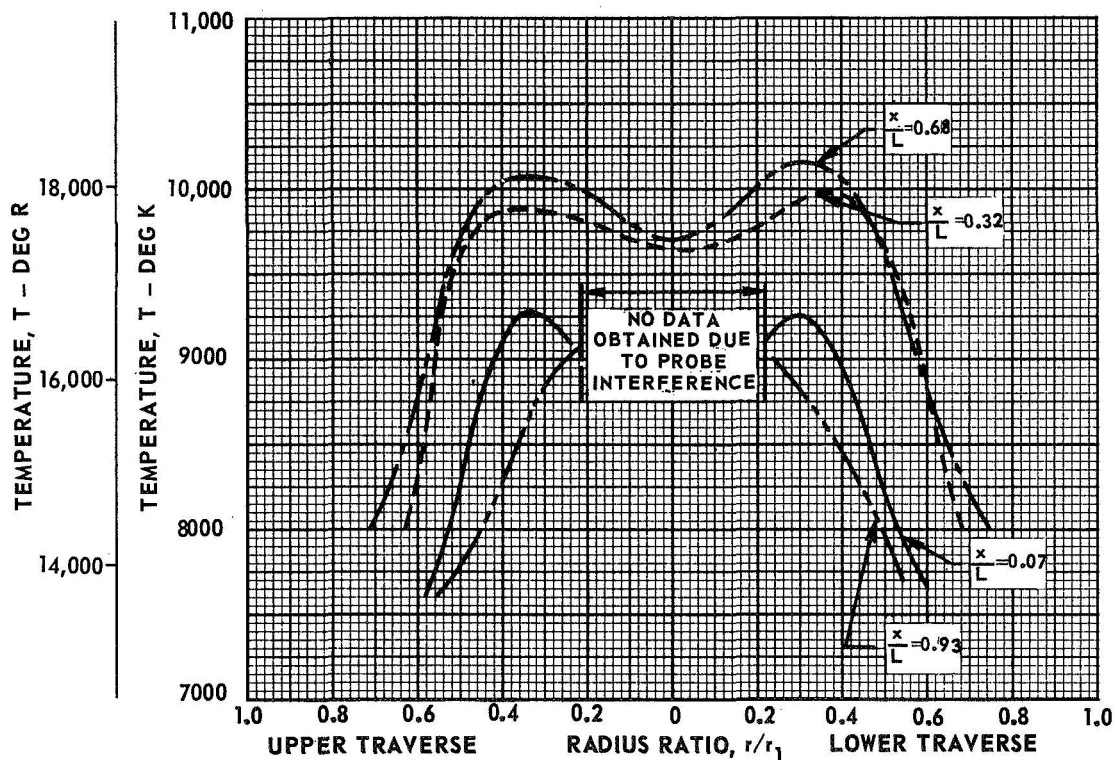
SEE FIG. 2 FOR BUFFER-GAS ARGON INJECTION CONFIGURATIONS

NO SIMULATED FUEL INJECTED

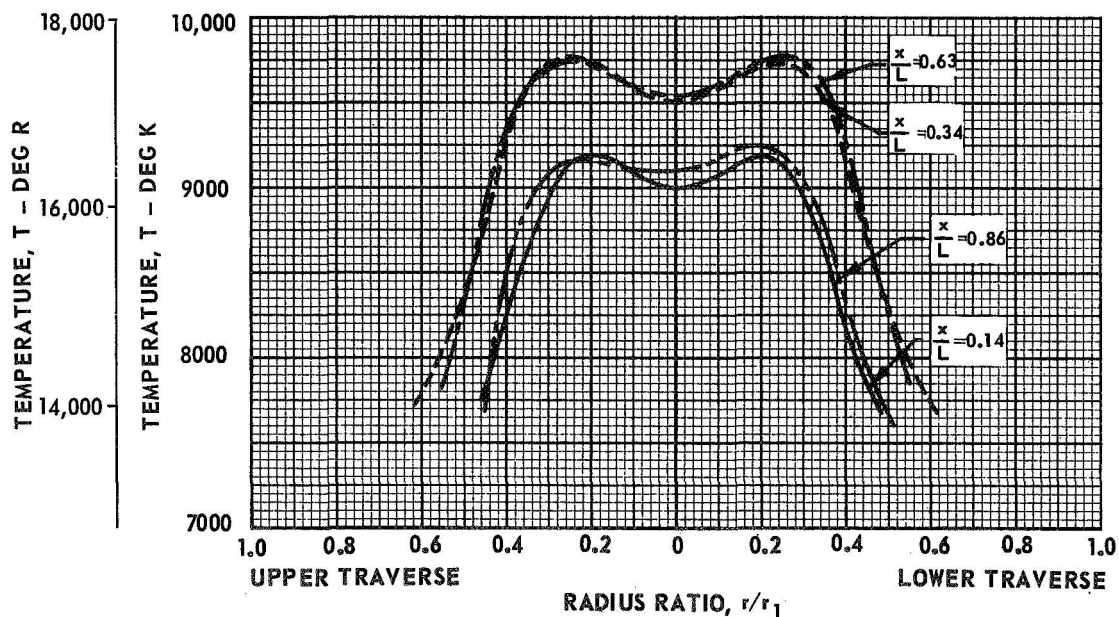
TEMPERATURES DETERMINED FROM PEAK INTENSITY OF AR I 6965 Å LINE

LINE	AXIAL POSITION SEE FIG. 2
—	1
- - -	2
- · - · -	3
— · — · —	4

(a) END-WALL BUFFER-GAS INJECTION



(b) PERIPHERAL-WALL BUFFER-GAS INJECTION



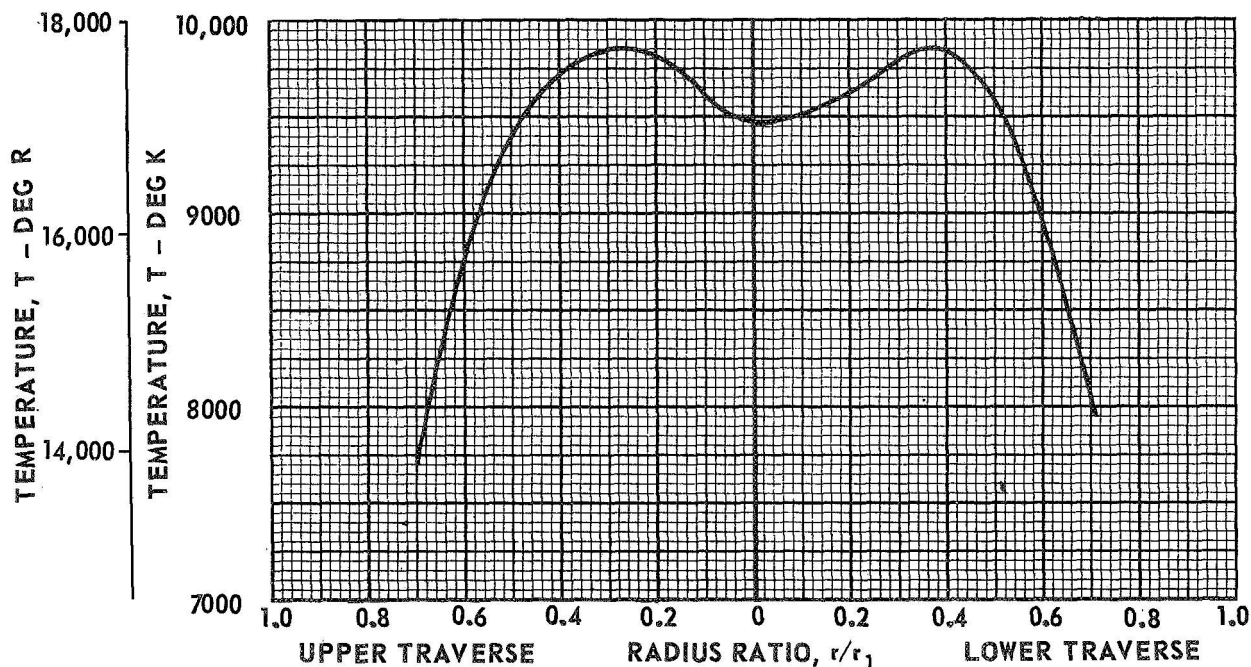
RADIAL DISTRIBUTIONS OF TEMPERATURE AND XE I 4671 Å PEAK INTENSITY CONSTANT FOR A PLASMA VORTEX HAVING A UNIFORM MIXTURE OF ARGON AND XENON IN 1.26-IN.-DIA VORTEX TUBE

$$\frac{P_{xe}}{P_{ar}} = 0.0055 \quad \frac{W_{ar}}{W_{xe}} = 55.6$$

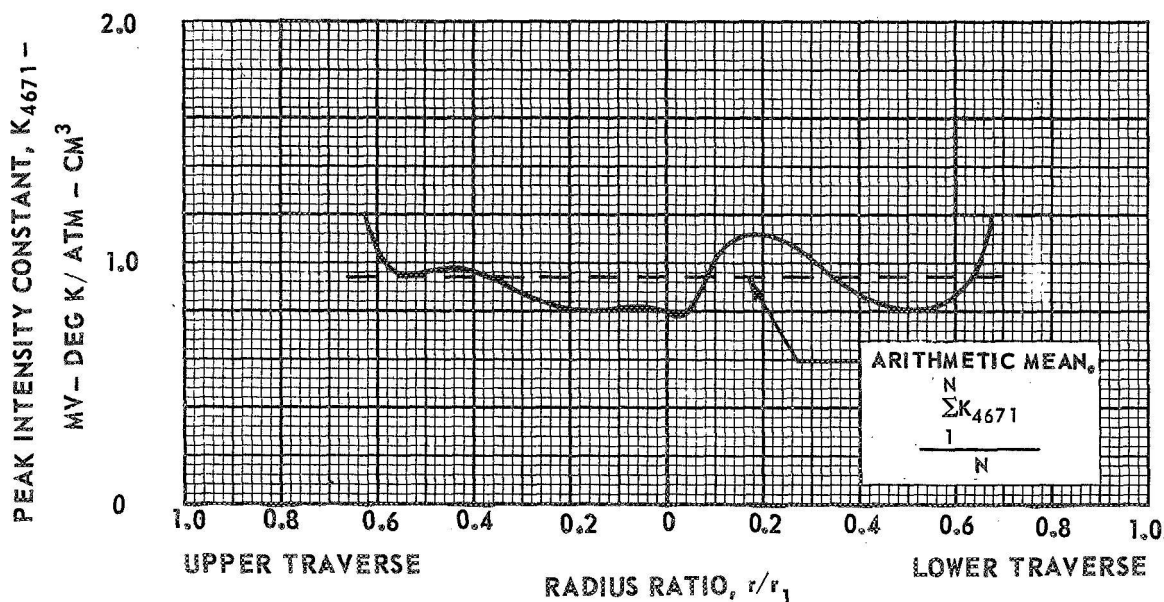
AXIAL POSITION 2 $\left(\frac{x}{L} = 0.32\right)$

END-WALL INJECTION OF ARGON-XENON BUFFER-GAS MIXTURE
(SEE FIG. 2(a))

(a) TEMPERATURE



(b) XE I 4671 Å PEAK INTENSITY CONSTANT



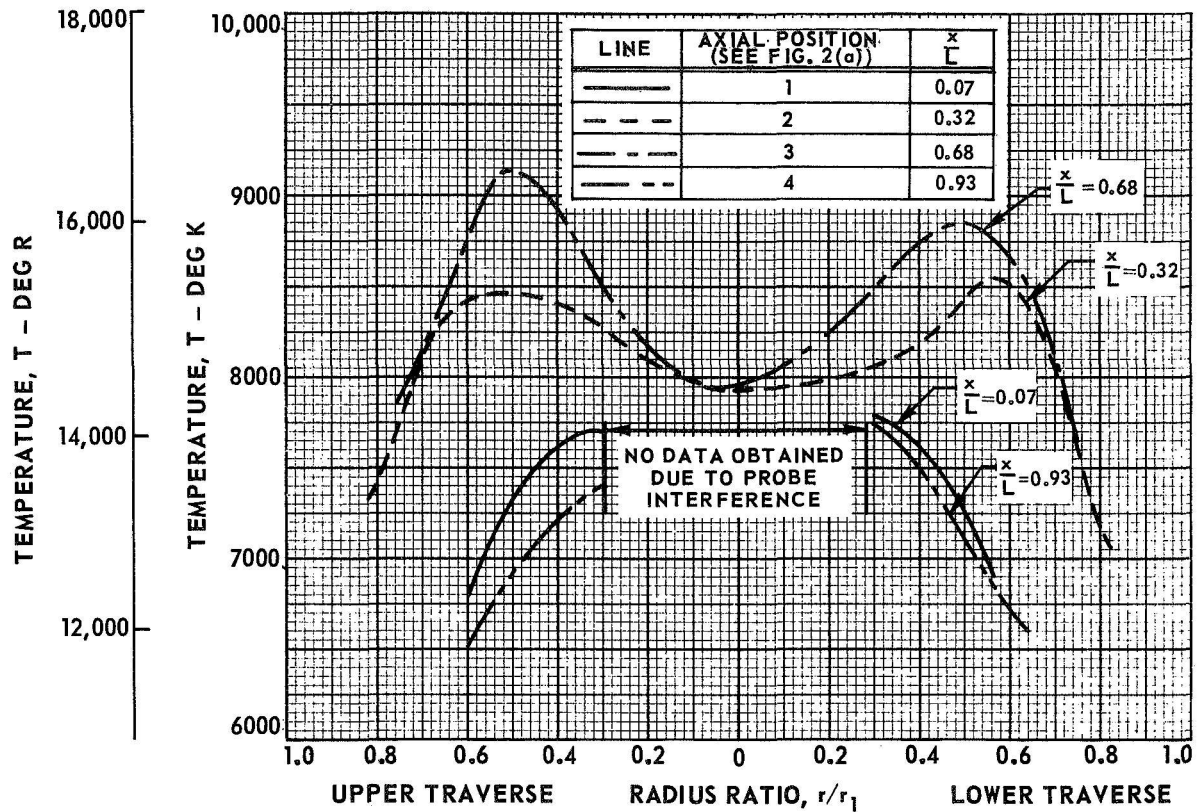
RADIAL DISTRIBUTIONS OF TEMPERATURE AND SIMULATED-FUEL PARTIAL PRESSURE RATIO FOR AN END-WALL DRIVEN ARGON VORTEX WITH CENTERLINE XENON INJECTION IN 1.26-IN.-DIA VORTEX TUBE

SEE FIG. 2(a) FOR INJECTION CONFIGURATIONS

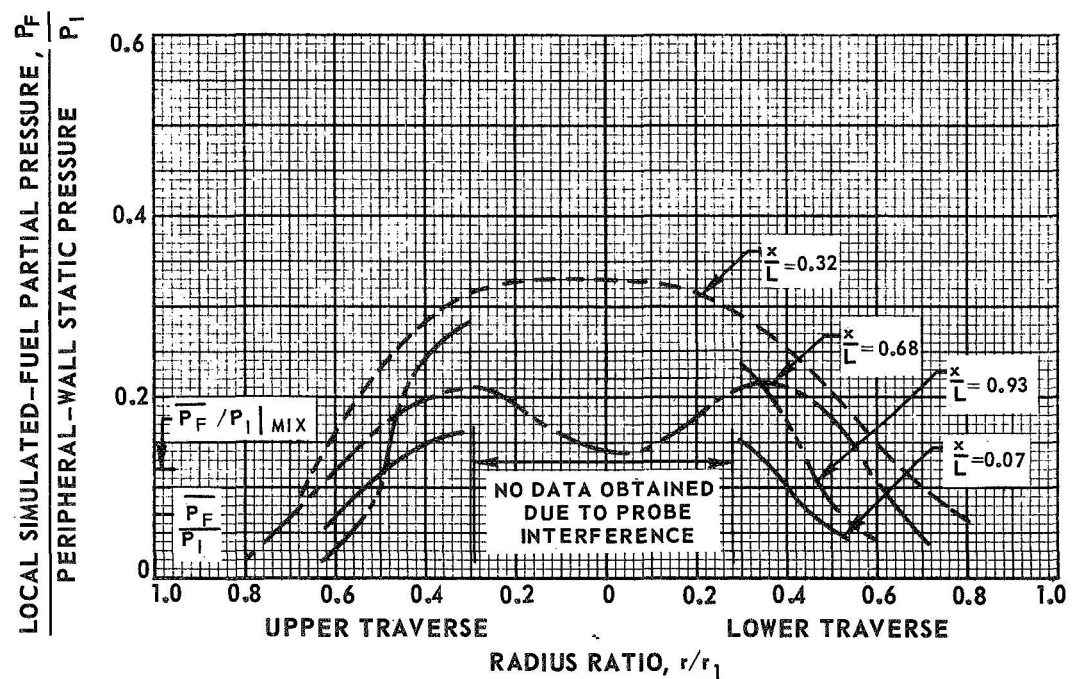
$$P_F = P_{xe}^o + 2 P_{xe}^+$$

$$\frac{W_{ar}}{W_{xe}} = 2.5$$

(a) TEMPERATURE (FROM ARI 6965A LINE)



(b) SIMULATED-FUEL PARTIAL PRESSURE (FROM XE I 4671 A LINE)



RADIAL DISTRIBUTIONS OF TEMPERATURE AND SIMULATED-FUEL PARTIAL PRESSURE FOR A PERIPHERAL-WALL DRIVEN ARGON VORTEX WITH CENTERLINE XENON INJECTION IN 1.26-IN.-DIA. VORTEX TUBE

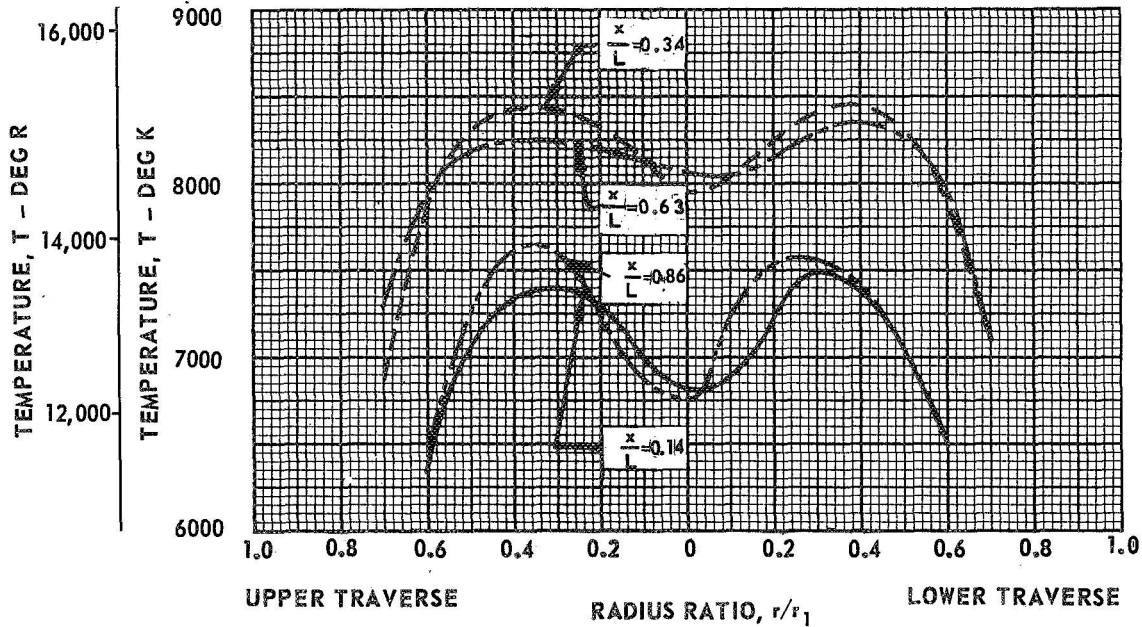
SEE FIG. 2(b) FOR INJECTION CONFIGURATION

$$W_{ar}/W_{xe} = 2.0$$

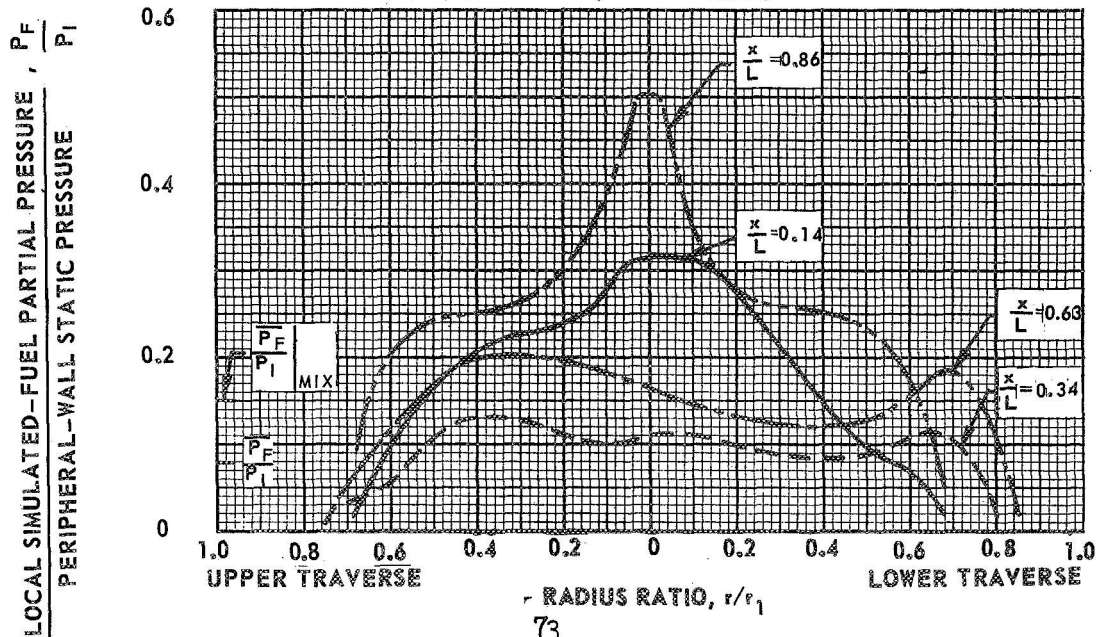
LINE	AXIAL POSITION SEE FIG. 2(b)	$\frac{x}{L}$
---	1	0.14
---	2	0.34
---	3	0.63
---	4	0.86

$$P_F = P_{xe^o} + 2P_{xe^+}$$

(a) TEMPERATURE (FROM ARI 6965 Å LINE)



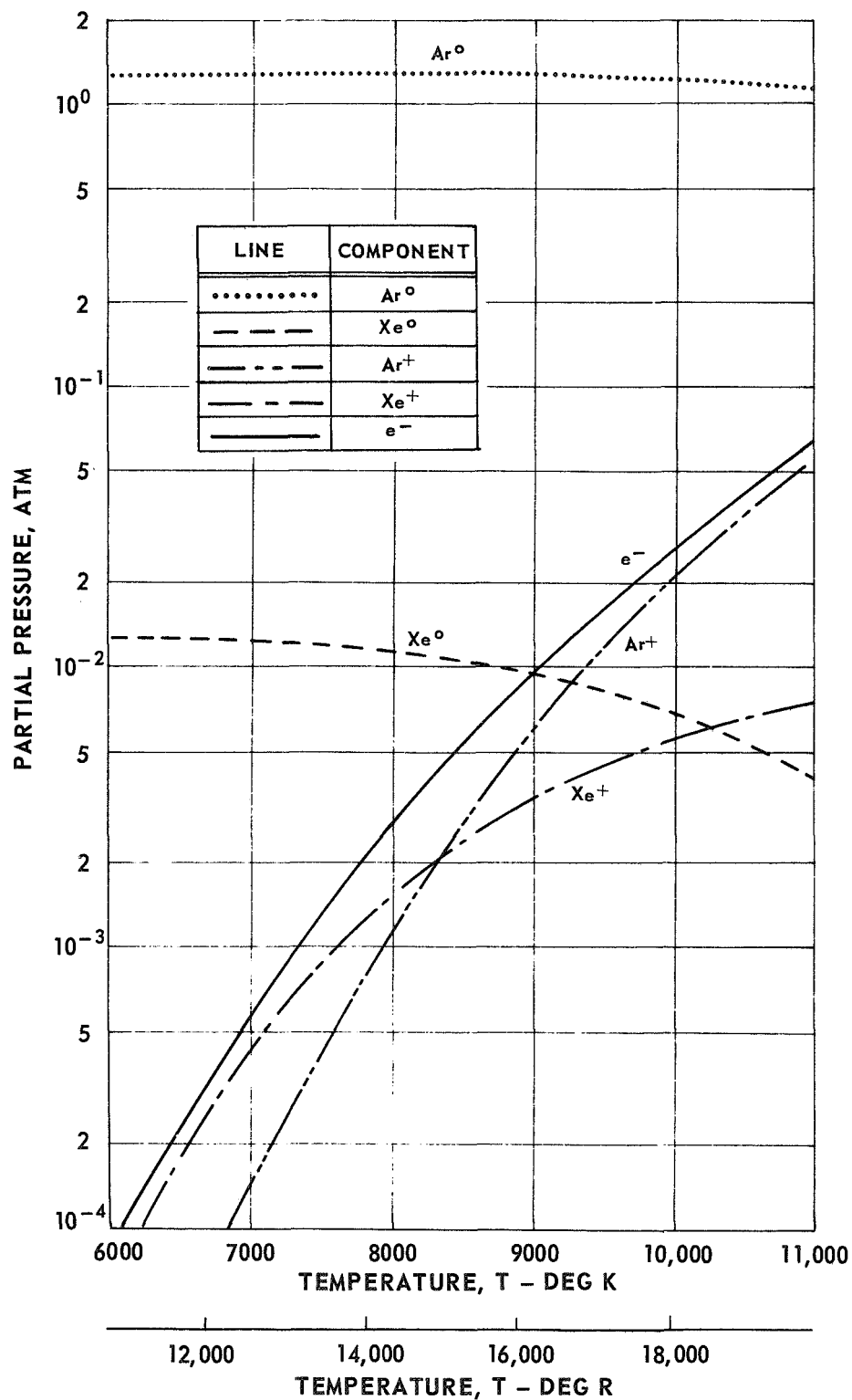
(b) SIMULATED-FUEL PARTIAL PRESSURE (FROM XEI 4671 Å LINE)



COMPOSITION OF AN EQUILIBRIUM ARGON - XENON MIXTURE WITH A XENON MOLE FRACTION OF 1 PERCENT

CALCULATED BY METHOD OF REF. 10

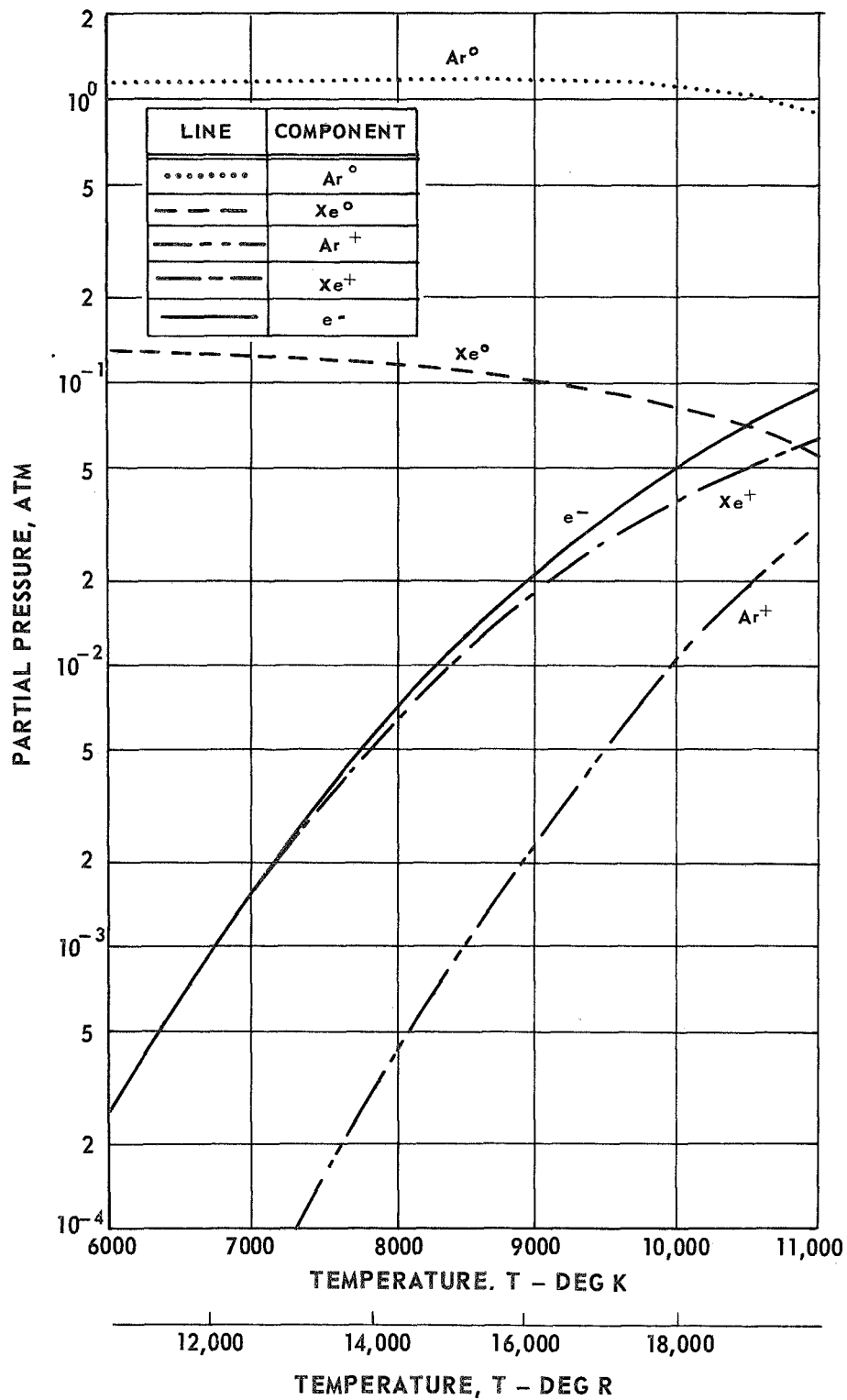
TOTAL PRESSURE = 1.3 ATM



COMPOSITION OF AN EQUILIBRIUM ARGON - XENON MIXTURE WITH XENON MOLE FRACTION OF 10 PERCENT

CALCULATED BY METHOD OF REF. 10

TOTAL PRESSURE = 1.3 ATM



PHOTOGRAPH OF VORTEX CHAMBER PERIPHERAL-WALL AFTER HEATED VORTEX TEST WITH ARGON/ TUNGSTEN-HEXAFLUORIDE SIMULATED FUEL

END-WALL BUFFER-GAS INJECTION

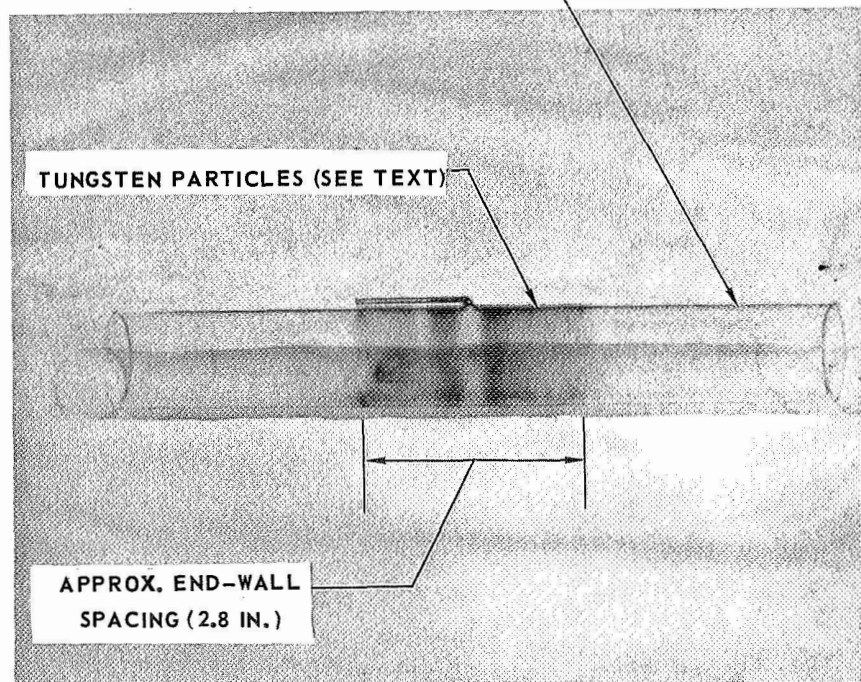
CENTERLINE SIMULATED-FUEL INJECTION

SEE FIG. 2(a) FOR INJECTION CONFIGURATIONS

CONSTANTS: $P_1 = 1.3 \text{ ATM}$; $W_B = 4.9 \times 10^{-3} \text{ LB/SEC}$; $W_{CG} = 7.5 \times 10^{-4} \text{ LB/SEC}$

$W_{WF_6} = 7.5 \times 10^{-6} \text{ LB/SEC}$; $W_B/W_F = 6.5$

1.26-IN.-ID X 1.37-IN.-OD
FUSED SILICA TUBE (SEE FIG. 2(a))



RADIAL DISTRIBUTIONS OF SIMULATED-FUEL PARTIAL PRESSURE FOR SEVERAL INJECTION VELOCITY RATIOS WITH PERIPHERAL-WALL SIMULATED-FUEL INJECTION IN 10-IN.-DIA VORTEX TUBE

PERIPHERAL-WALL BUFFER-GAS INJECTION

NITROGEN/IODINE SIMULATED FUEL

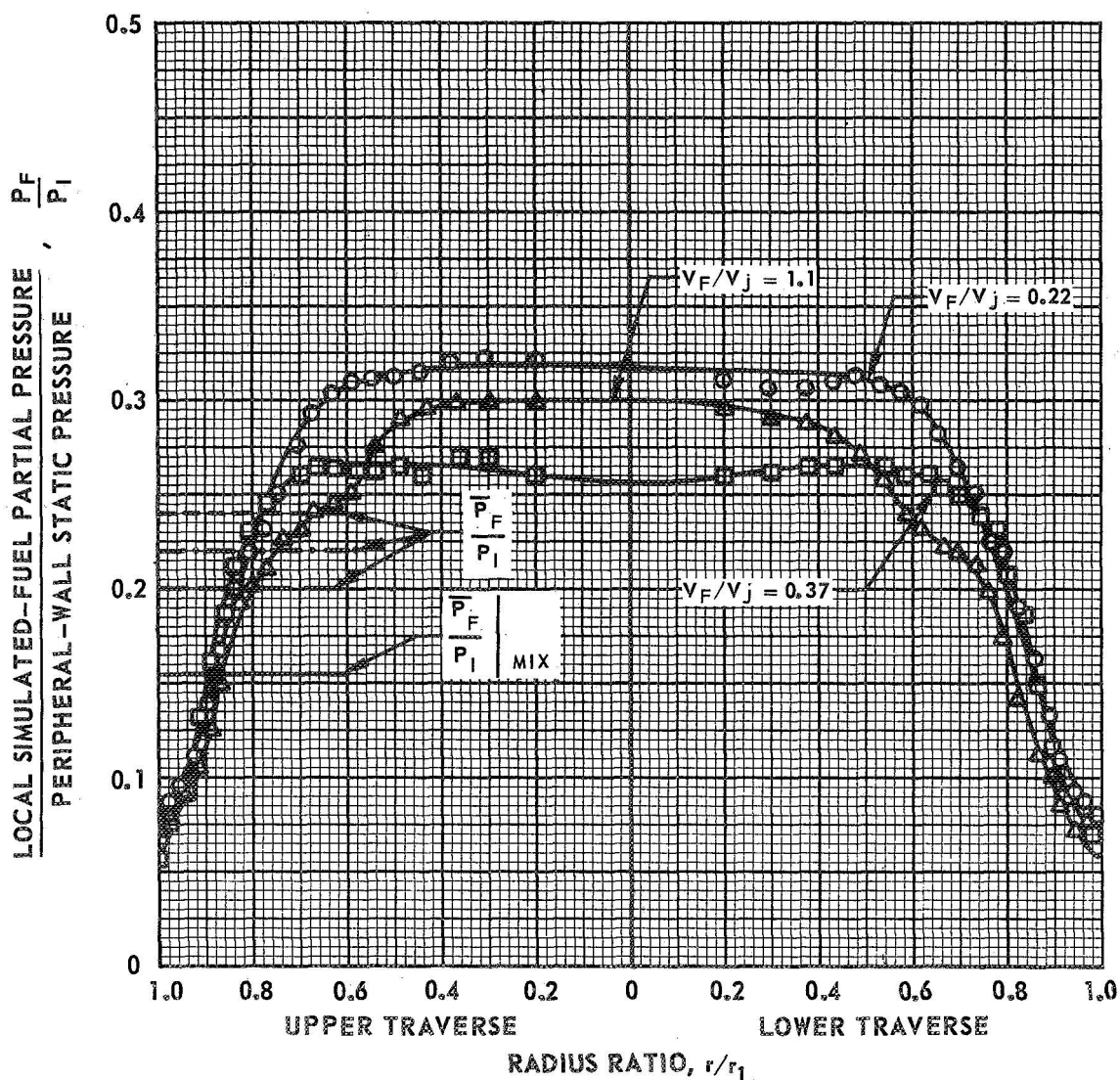
SEE FIG. 4(a) FOR INJECTION CONFIGURATIONS

V_F VARIED BY CHANGING NUMBER OF SIMULATED-FUEL INJECTION PORTS

CONSTANTS: $Re_j = 1.5 \times 10^5$; $Re_F = 120$; BYPASS = 48%

$W_F = 6.9 \times 10^{-3}$ LB/SEC; $W_B/W_F = 5.2$; $A_{B,j} = 0.84$ IN²

SYMBOL	\bar{P}_F/P_I	V_F/V_j	$A_{F,j} - \text{IN}^2$
—○—	(0.24)	0.22	0.731
—□—	(0.22)	0.37	0.436
—△—	(0.20)	1.1	0.146



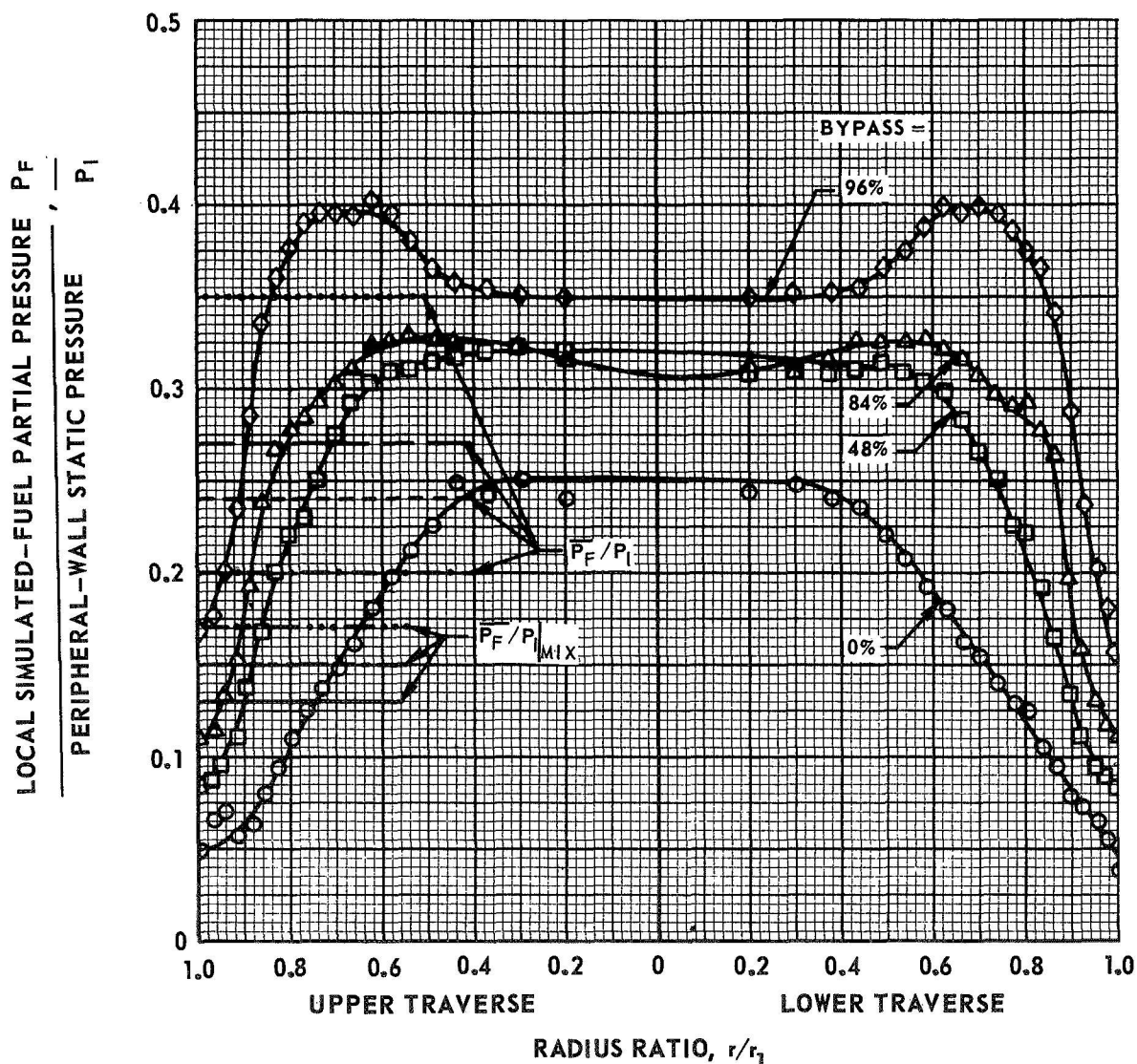
RADIAL DISTRIBUTIONS OF SIMULATED-FUEL PARTIAL PRESSURE FOR SEVERAL BYPASS RATIOS WITH PERIPHERAL-WALL SIMULATED-FUEL INJECTION IN 10-IN.-DIA VORTEX TUBE

PERIPHERAL-WALL BUFFER-GAS INJECTION

NITROGEN/IODINE SIMULATED FUEL

SEE FIG. 4(a) FOR INJECTION CONFIGURATIONS

SYMBOL	Re_j	Re_r	BYPASS RATIO, PERCENT	W_F - LB/SEC	W_B/W_F	V_F/V_j	\bar{P}_F/P_I	$\bar{P}_F/P_I _{MIX}$
—○—	1.5	184	0	6.7×10^{-3}	5.2	0.23	(0.20)	(0.17)
—□—	1.5	120	48	6.6×10^{-3}	5.2	0.22	(0.24)	(0.15)
—△—	1.7	83	84	6.7×10^{-3}	5.8	0.20	(0.27)	(0.13)
—◇—	1.5	58	96	6.9×10^{-3}	5.0	0.24	(0.35)	(0.13)



RADIAL DISTRIBUTIONS OF SIMULATED-FUEL PARTIAL PRESSURE FOR SEVERAL INJECTION VELOCITY RATIOS WITH END-WALL ($r/r_1 = 0.8$) SIMULATED-FUEL INJECTION IN 10-IN.-DIA VORTEX TUBE

PERIPHERAL-WALL BUFFER-GAS INJECTION

NITROGEN/IODINE SIMULATED FUEL

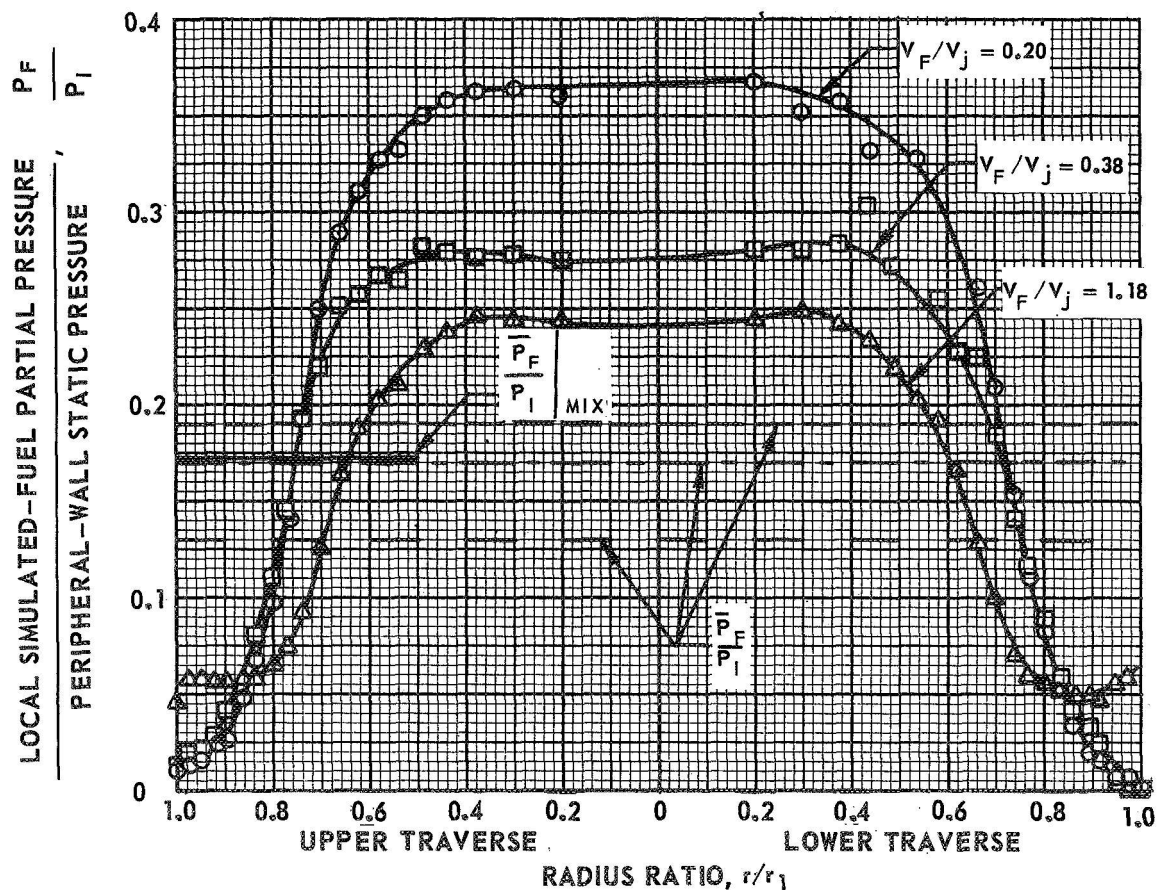
SEE FIG. 5(a) FOR INJECTION CONFIGURATIONS

V_F VARIED BY CHANGING NUMBER OF SIMULATED-FUEL INJECTION PORTS

CONSTANTS: $Re_j = 1.5 \times 10^5$; $Re_r = 124$; BYPASS = 48%

$W_F = 7.1 \times 10^{-3}$ LB/SEC; $W_B/W_F = 5.0$

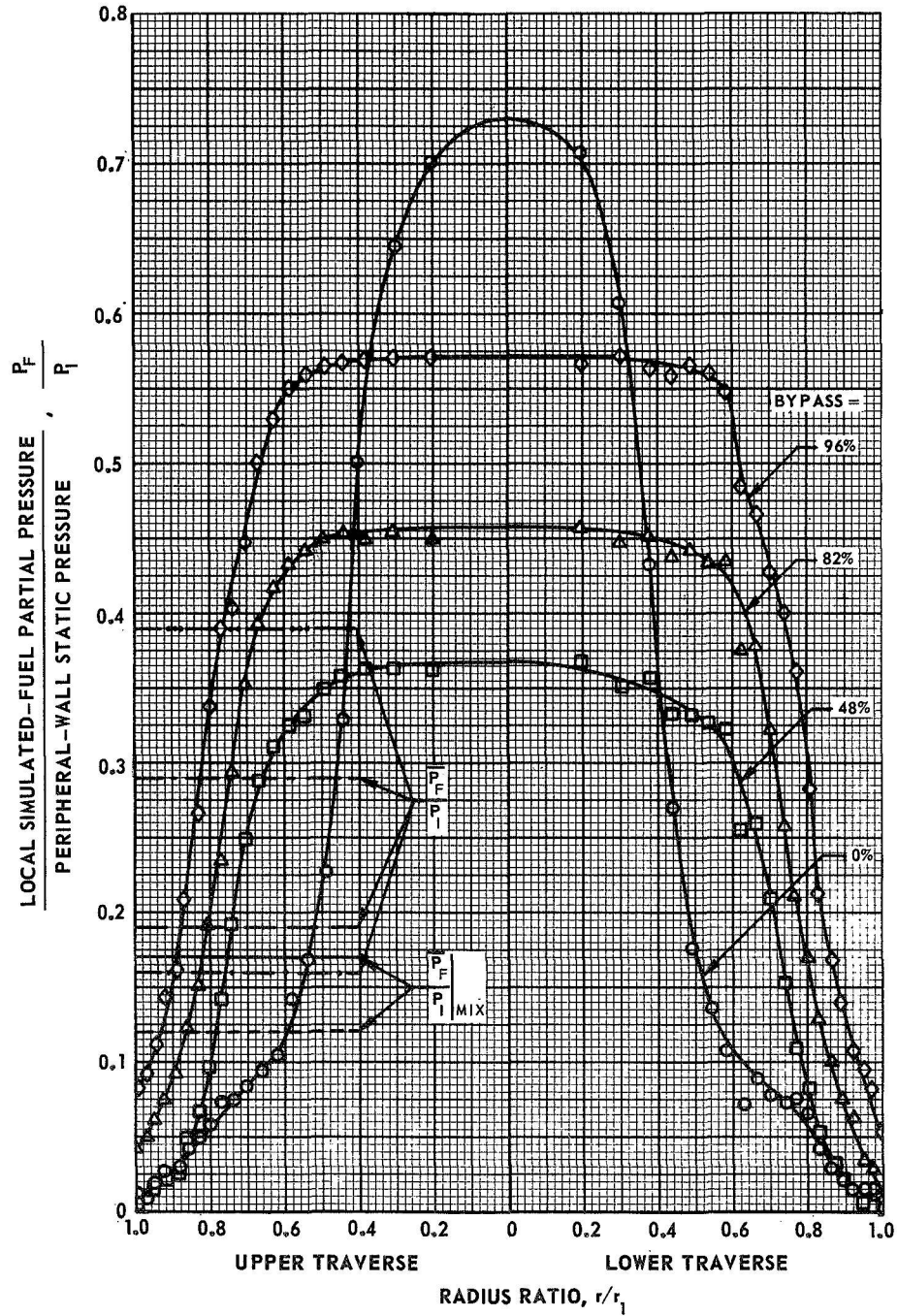
SYMBOL	\bar{P}_F/P_I	V_F/V_j	$A_{F,j} - \text{IN.}^2$
—○—	(0.19)	0.20	0.871
—□—	(0.17)	0.38	0.436
—△—	(0.13)	1.18	0.145



**RADIAL DISTRIBUTIONS OF SIMULATED FUEL PARTIAL PRESSURE
FOR SEVERAL BYPASS RATIOS WITH END WALL ($r/r_1 = 0.8$)
SIMULATED FUEL INJECTION IN 10-IN.-DIA VORTEX TUBE**

PERIPHERAL-WALL BUFFER-GAS INJECTION
NITROGEN/IODINE SIMULATED FUEL
SEE FIG. 5(a) FOR INJECTION CONFIGURATIONS
CONSTANT: $W_F = 7.1 \times 10^{-3}$ LB/SEC

SYMBOL	Re_j	Re_r	BYPASS RATIO, PERCENT	W_B/W_F	V_F/V_j	\bar{P}_F/P_I	$\bar{P}_F/P_{I,MIX}$
○	1.5×10^5	188	0	5.0	0.19	(0.16)	(0.17)
□	1.5×10^5	124	48	5.0	0.20	(0.19)	(0.17)
△	1.7×10^5	83	82	5.6	0.17	(0.29)	(0.12)
◇	1.5×10^5	59	96	4.9	0.21	(0.39)	(0.12)



**RADIAL DISTRIBUTIONS OF SIMULATED-FUEL PARTIAL PRESSURE FOR SEVERAL
INJECTION VELOCITY RATIOS WITH END-WALL ($r/r_1 = 0.5$)
SIMULATED-FUEL INJECTION IN 10-IN.-DIA VORTEX TUBE**

PERIPHERAL-WALL BUFFER-GAS INJECTION
NITROGEN/IODINE SIMULATED FUEL

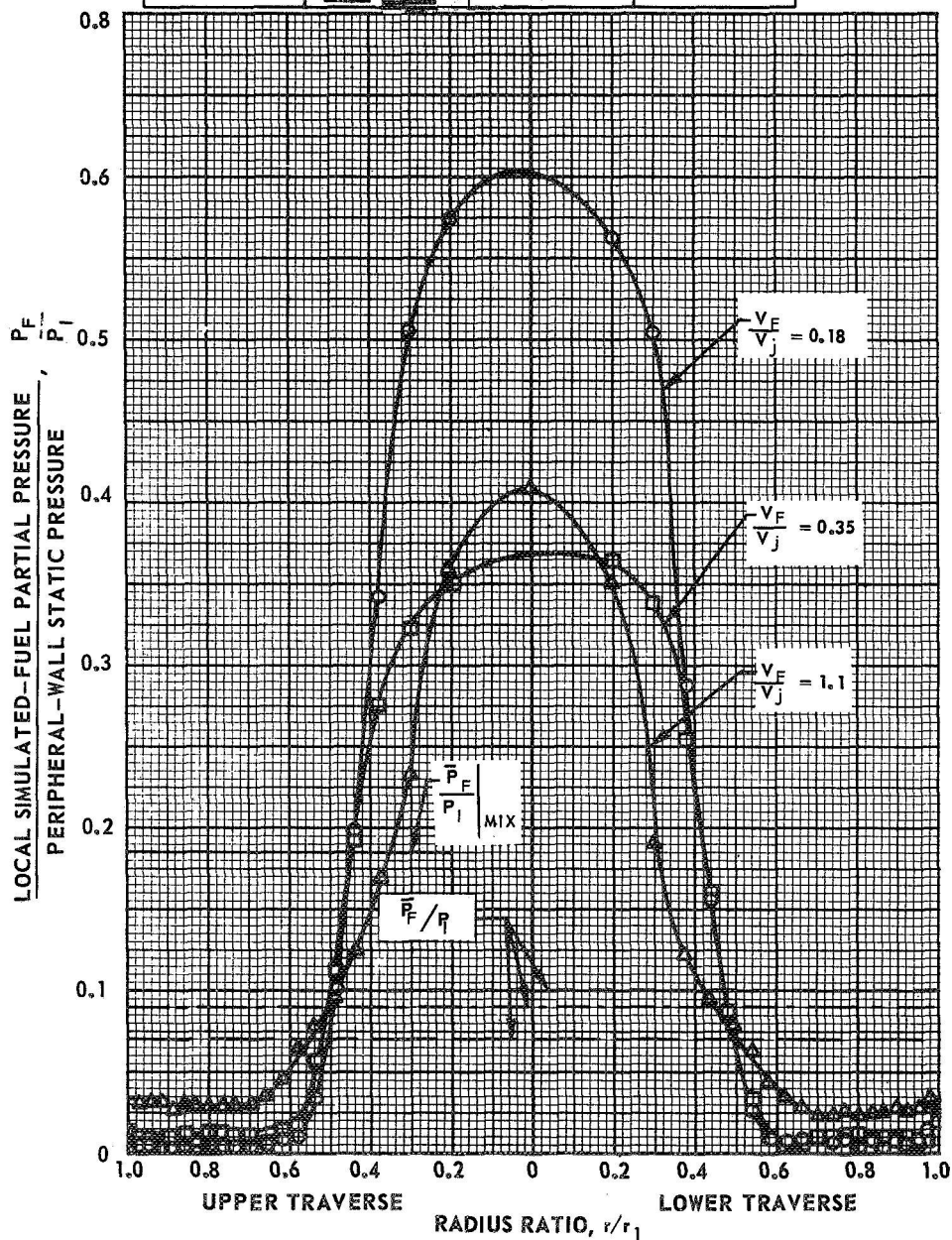
SEE FIG. 5(b) FOR INJECTION CONFIGURATIONS

V_F VARIED BY CHANGING NUMBER OF SIMULATED-FUEL INJECTION PORTS

CONSTANTS: $Re_J = 1.6 \times 10^5$; $Re_F = 123$; BYPASS = 48%

$W_F = 7.1 \times 10^{-3}$ LB/SEC; $W_B/W_F = 5.1$

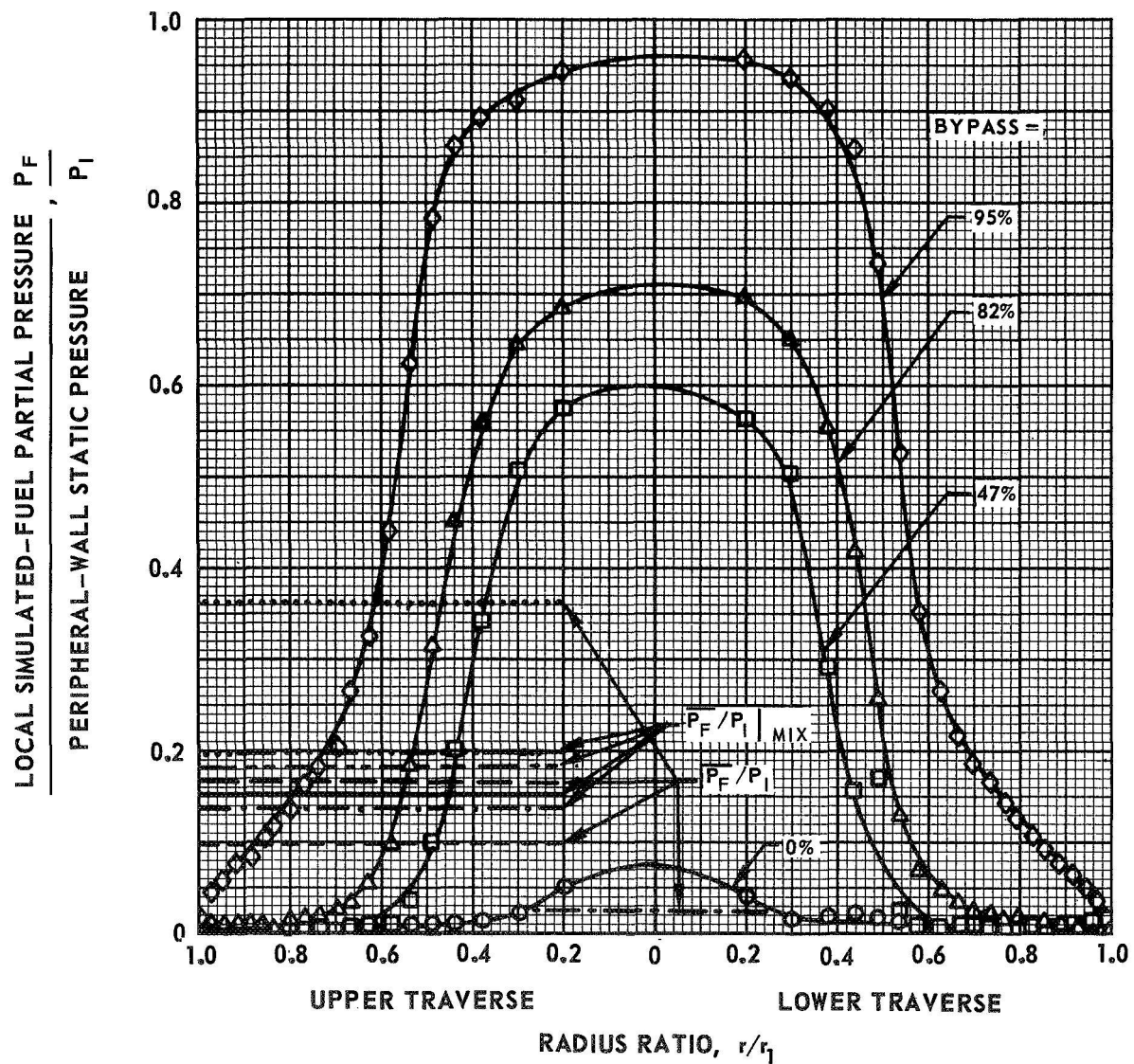
SYMBOL	\bar{P}_F/P_I	V_F/V_J	$A_{FJ} - \text{IN.}^2$
—○—	(0.10)	0.18	0.871
—□—	(0.09)	0.35	0.436
—△—	(0.07)	1.10	0.145



RADIAL DISTRIBUTIONS OF SIMULATED-FUEL PARTIAL PRESSURE FOR SEVERAL BYPASS RATIOS WITH END-WALL ($r/r_1 = 0.5$) SIMULATED-FUEL INJECTION IN 10-IN.-DIA VORTEX TUBE

PERIPHERAL-WALL BUFFER-GAS INJECTION
NITROGEN/IODINE SIMULATED FUEL
SEE FIG. 5(b) FOR INJECTION CONFIGURATIONS
CONSTANT: $W_F = 7.1 \times 10^{-3}$ LB/SEC

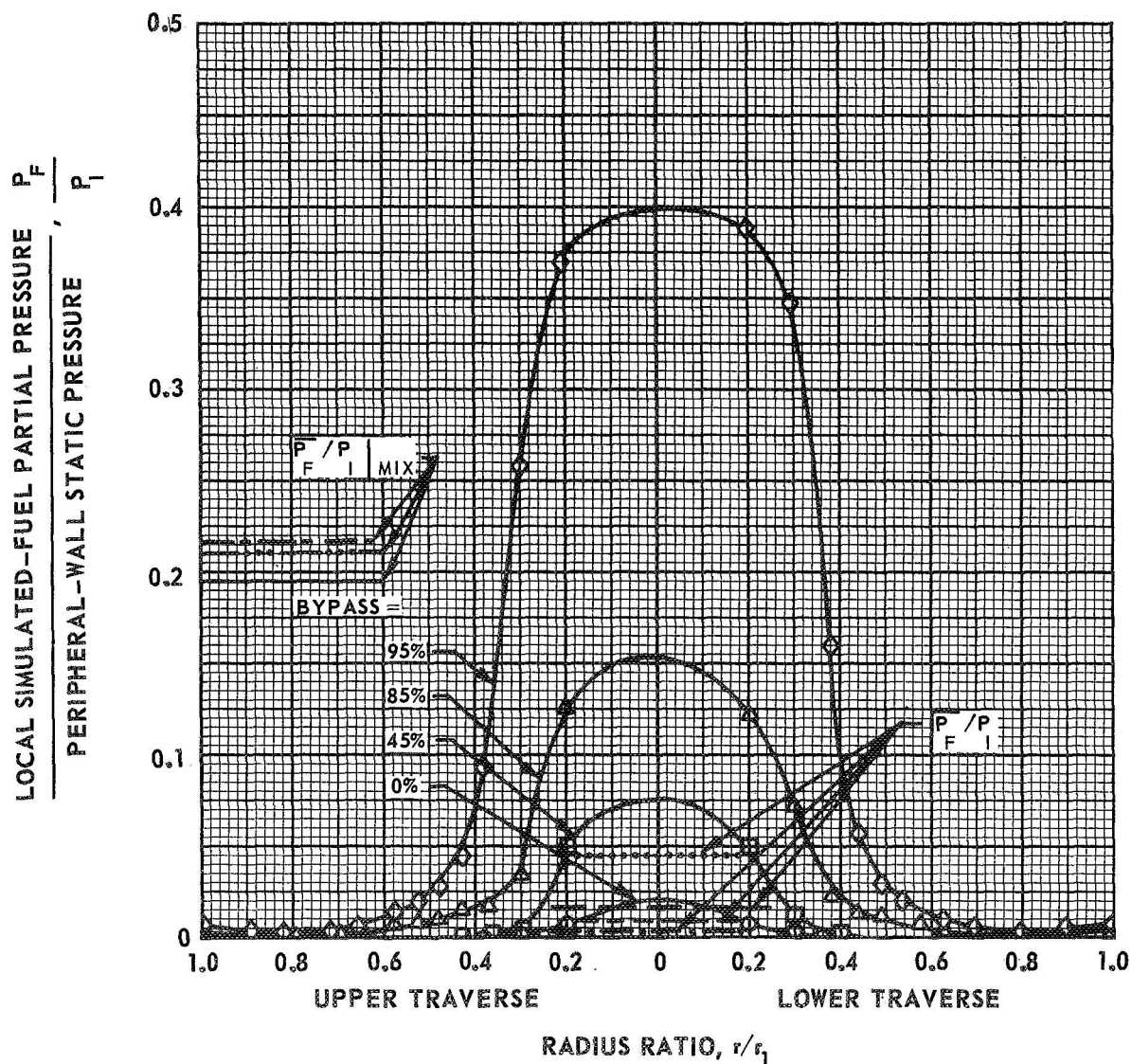
SYMBOL	Re_j	Re_r	BYPASS RATIO PERCENT	W_B/W_F	V_F/V_j	\bar{P}_F/P_I	$\bar{P}_F/P_I _{MIX}$
—○—	1.6×10^5	186	0	5.0	0.19	(0.03)	(0.195)
—□—	1.6×10^5	123	48	5.0	0.18	(0.095)	(0.182)
—△—	1.7×10^5	84	82	5.6	0.17	(0.16)	(0.15)
—◇—	1.5×10^5	59	95	4.9	0.19	(0.36)	(0.132)



RADIAL DISTRIBUTIONS OF SIMULATED-FUEL PARTIAL PRESSURE FOR SEVERAL BYPASS RATIOS WITH CENTERLINE SIMULATED-FUEL INJECTION IN 10-IN.-DIA VORTEX TUBE

PERIPHERAL-WALL BUFFER-GAS INJECTION
NITROGEN/IODINE SIMULATED FUEL
SEE FIG. 4(b) FOR INJECTION CONFIGURATIONS
CONSTANT: $w_F = 7.5 \times 10^{-3}$ LB/SEC

SYMBOL	Re_j	Re_r	BYPASS RATIO, PERCENT	w_B/w_F	V_F/V_j	$\overline{P_F}/P_1$	$\overline{P_F}/P_1 _{MIX}$
—○—	1.5×10^5	189	0	4.6	0.62	(0.004)	(0.21)
—□—	1.6×10^5	121	45	5.1	0.57	(0.01)	(0.195)
—△—	1.6×10^5	82	85	5.0	0.58	(0.015)	(0.195)
—◇—	1.5×10^5	58	95	4.3	0.67	(0.045)	(0.217)




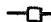

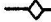
RADIAL DISTRIBUTIONS OF SIMULATED-FUEL PARTIAL PRESSURE FOR SEVERAL SIMULATED-FUEL INJECTION CONFIGURATIONS IN 10-IN.-DIA VORTEX TUBE

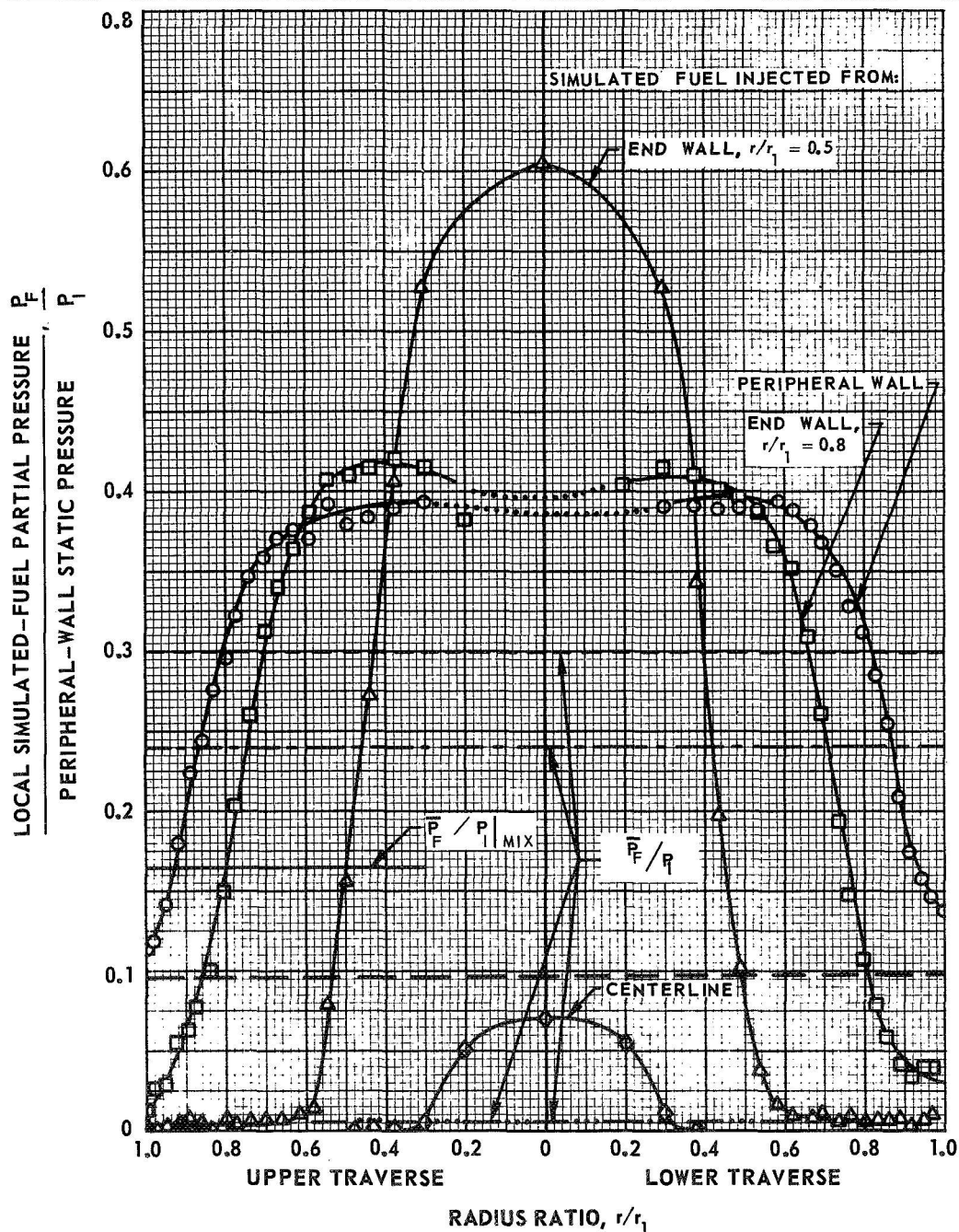
NITROGEN/IODINE SIMULATED-FUEL

PERIPHERAL-WALL BUFFER-GAS INJECTION

SEE FIGS. 4 AND 5 FOR INJECTION CONFIGURATION

CONSTANTS: $R_{e_j} = 1.6 \times 10^5$; $R_{e_r} = 121$;

SYMBOL	SIMULATED-FUEL INJECTION CONFIGURATION	\bar{P}_F / P_I	$\bar{P}_F / P_I _{WALL}$	V_F / V_j	BYPASS RATIO, PERCENT	W_F LB/SEC	W_F / W_B
	PERIPHERAL WALL	(0.30)	~ 0.12	0.28	48	6.9	5.2
	END-WALL, $r/r_1 = 0.8$	(0.24)	~ 0.01	0.30	49	7.1	5.0
	END-WALL, $r/r_1 = 0.5$	(0.098)	< 0.005	0.28	47	7.1	5.0
	CENTERLINE	(0.004)	< 0.005	0.57	45	7.5	5.1

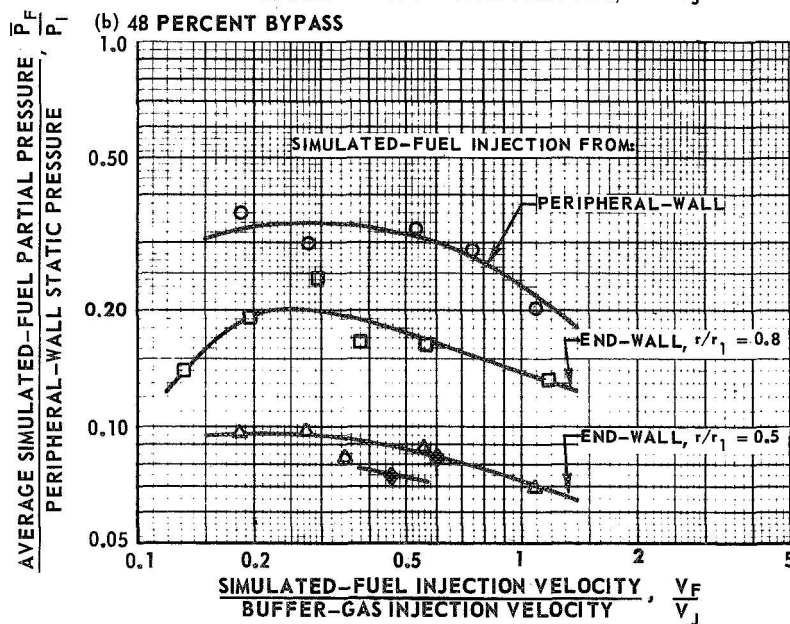
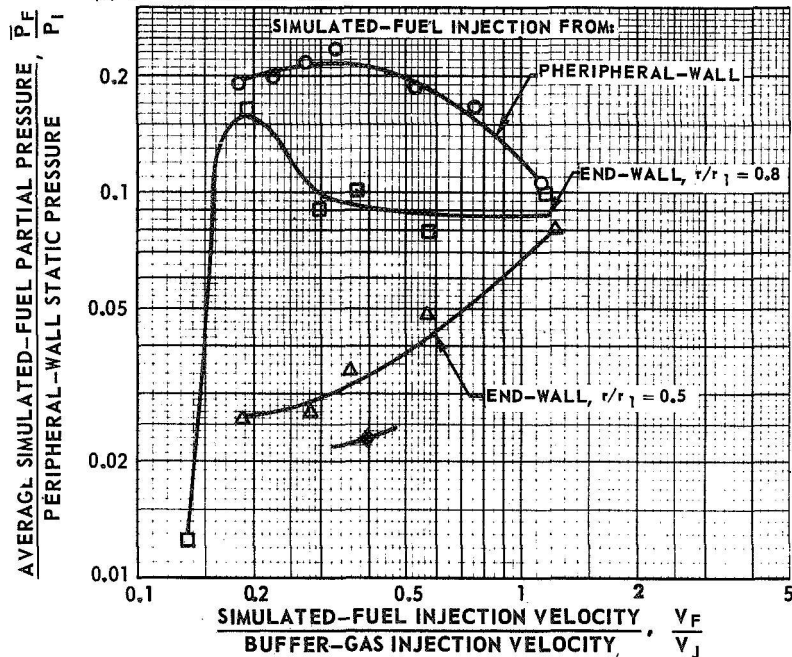


EFFECT OF SIMULATED-FUEL INJECTION VELOCITY ON AVERAGE SIMULATED-FUEL PARTIAL PRESSURE

PERIPHERAL-WALL BUFFER-GAS INJECTION

SYMBOL	VORTEX TUBE DIA.	SIMULATED-FUEL INJECTION CONFIGURATION	Re_j	W_F	W_B/W_F
○	10-IN.	PERIPHERAL-WALL	1.5×10^5	7.0×10^{-3}	5.0
□	10-IN.	END-WALL $r/r_1 = 0.8$	1.5×10^5	7.1×10^{-3}	5.0
△	10-IN.	END-WALL $r/r_1 = 0.5$	1.6×10^5	7.1×10^{-3}	5.1
▲	1.26-IN.	END-WALL $r/r_1 = 0.5$	1.4×10^5	0.9×10^{-3}	5.0
◆	1.26-IN.	CENTERLINE	1.5×10^5	1.0×10^{-3}	5.0

(a) 0 PERCENT BYPASS



(CONTINUED)

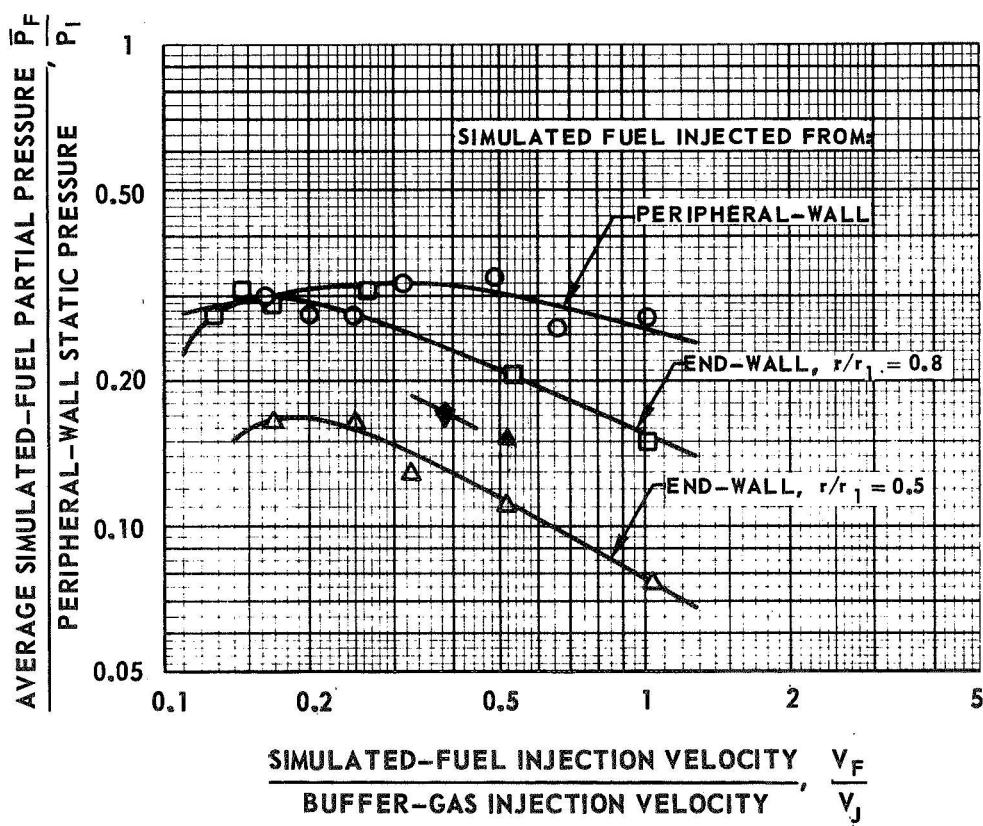
EFFECT OF SIMULATED-FUEL INJECTION VELOCITY ON AVERAGE SIMULATED-FUEL PARTIAL PRESSURE (CONTINUED)

PERIPHERAL-WALL BUFFER-GAS INJECTION

SYMBOL	VORTEX TUBE DIA	SIMULATED-FUEL INJECTION CONFIGURATION	Re_j	W_F	W_B/W_F
○	10-IN.	PERIPHERAL-WALL	1.7×10^5	6.7×10^{-3}	5.8
□	10-IN.	END-WALL $r/r_1 = 0.8$	1.7×10^5	7.1×10^{-3}	5.6
△	10-IN.	END-WALL $r/r_1 = 0.5$	1.7×10^5	7.1×10^{-3}	5.6
◆	1.26-IN.	CENTERLINE *	1.5×10^5	1.0×10^{-3}	5.0
▲	1.26-IN.	END-WALL $r/r_1 = 0.5$ *	1.5×10^5	0.9×10^{-3}	5.6

*69 PERCENT BYPASS FOR THIS CONFIGURATION

(c) 83 PERCENT BYPASS



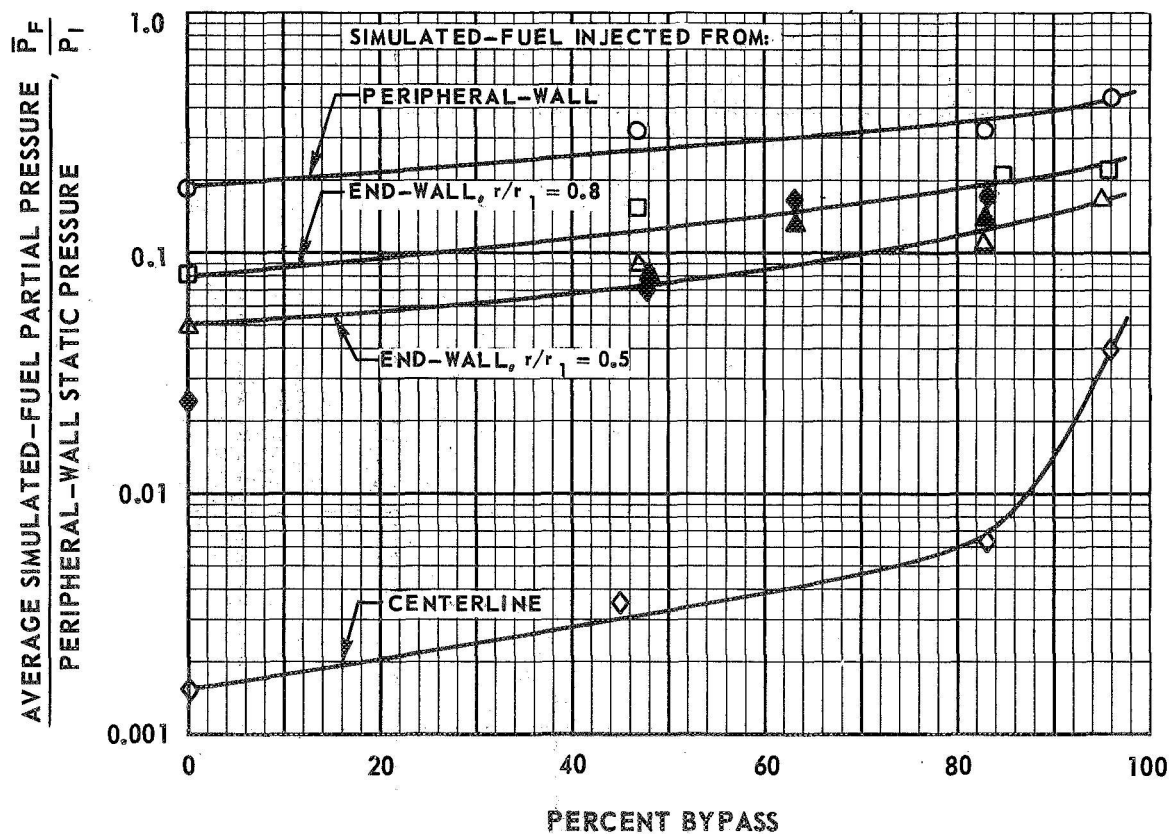
EFFECT OF BUFFER GAS BYPASS FLOW ON AVERAGE SIMULATED-FUEL PARTIAL PRESSURE

PERIPHERAL-WALL BUFFER-GAS INJECTION

INJECTION VELOCITY RATIO, $\frac{V_F}{V_j} \approx 0.55$

SYMBOL	VORTEX TUBE DIA	SIMULATED-FUEL INJECTION CONFIGURATION	Re_j	W_F	W_B/W_F
—○—	10-IN.	PERIPHERAL-WALL	1.6×10^5	6.7×10^{-3}	5.4
—□—	10-IN.	END-WALL $r/r_1 = 0.8$	1.5×10^5	7.1×10^{-3}	5.0
—△—	10-IN.	END-WALL $r/r_1 = 0.5$	1.6×10^5	7.1×10^{-3}	5.1
—◇—	10-IN.	CENTERLINE	1.7×10^5	7.5×10^{-3}	5.0
▲	1.26-IN.	END-WALL $r/r_1 = 0.5$	1.4×10^5	0.9×10^{-3}	5.0
◆	1.26-IN.	CENTERLINE*	1.5×10^5	1.0×10^{-3}	5.0

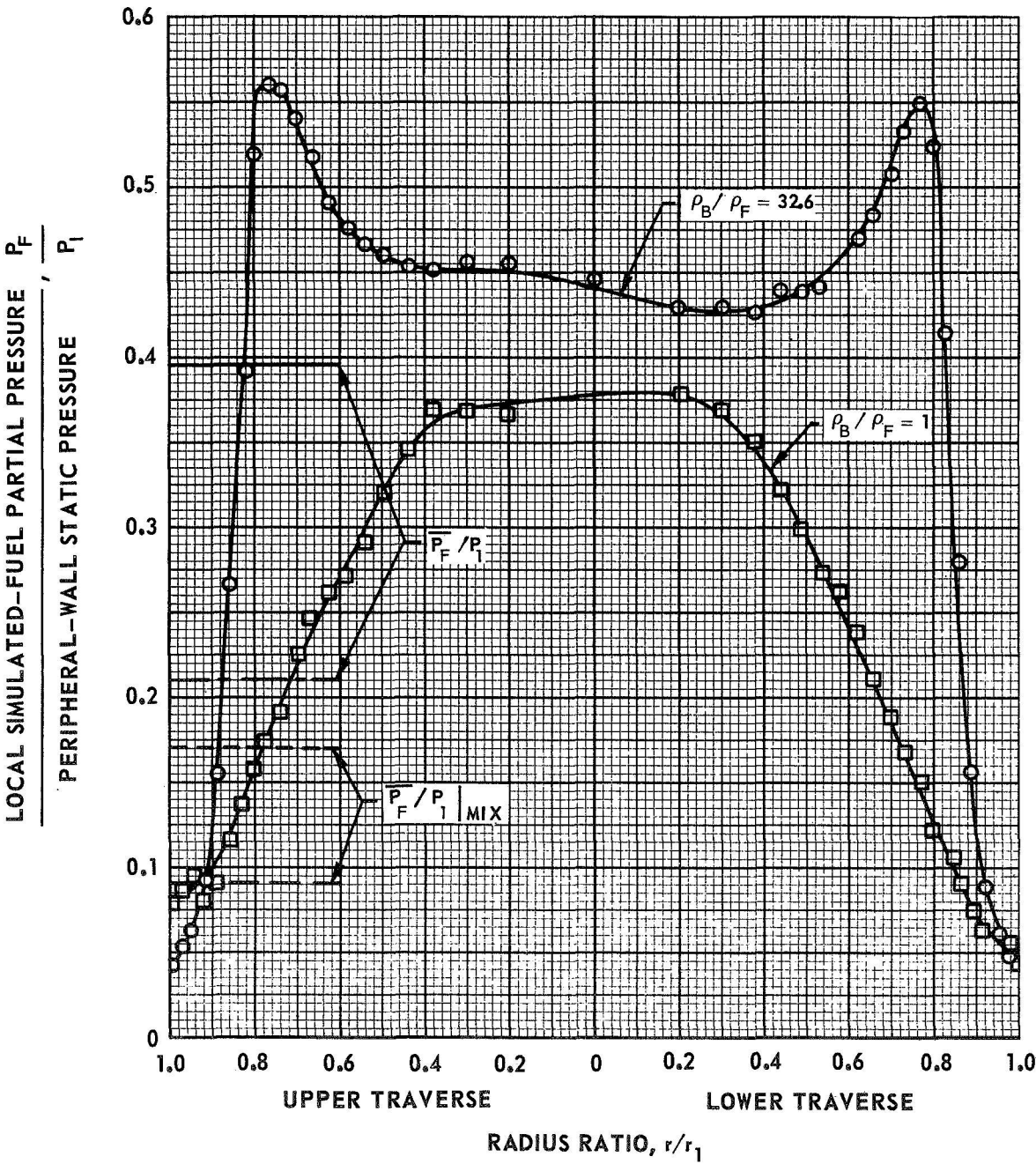
* $V_F/V_j = 0.4$ FOR THIS CONFIGURATION



RADIAL DISTRIBUTIONS OF SIMULATED - FUEL PARTIAL PRESSURE FOR TWO DENSITY RATIOS IN 10-IN.-DIA VORTEX TUBE

PERIPHERAL-WALL BUFFER-GAS INJECTION
END-WALL SIMULATED-FUEL INJECTION ($r/r_1 = 0.8$)
SEE FIG. 5 (a) FOR INJECTION CONFIGURATIONS

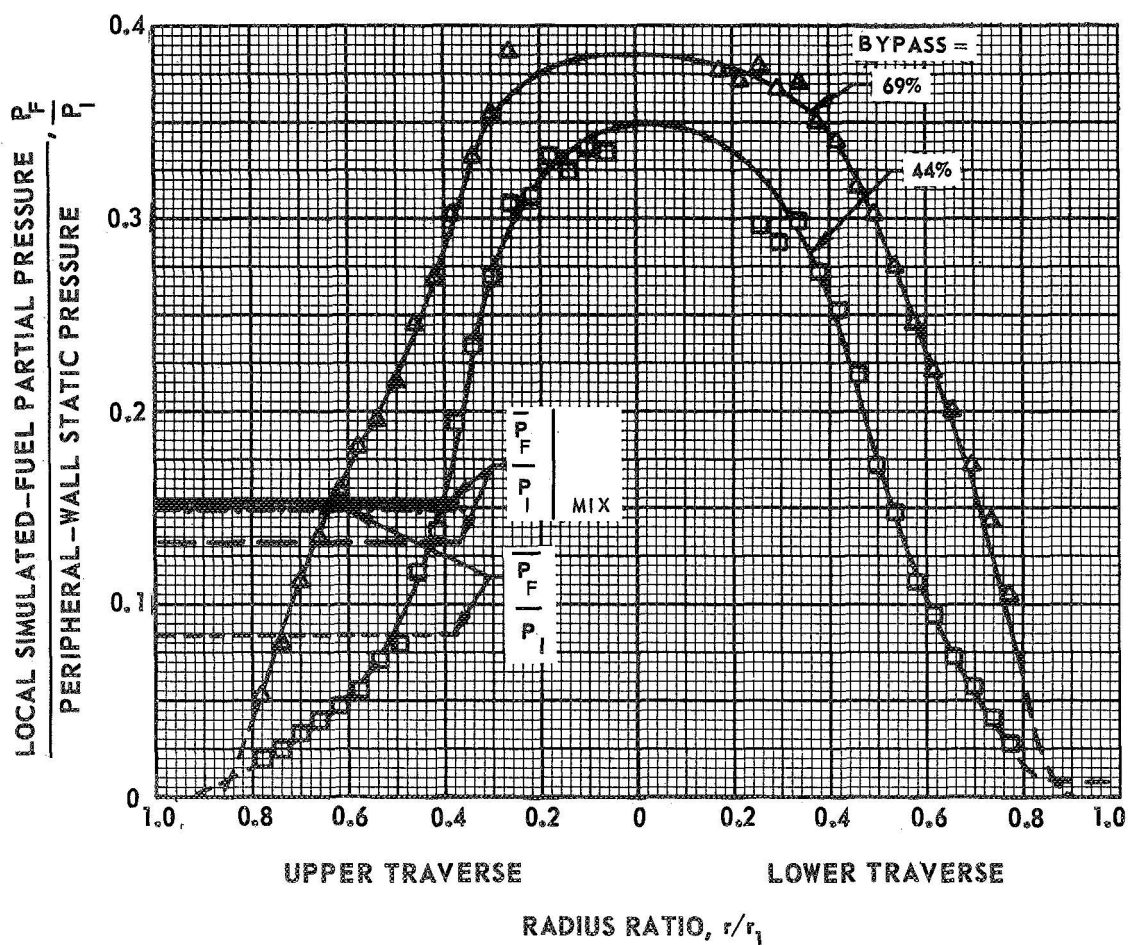
SYMBOL	BUFFER GAS	SIMULATED FUEL	ρ_B/ρ_F	Re_j	Re_r	BYPASS RATIO, PERCENT	w_F , LB/SEC	w_B/w_F	v_F/v_j	\bar{P}_F/P_1	\bar{P}_F/P_1 MIX
—○—	SULFUR HEXAFLUORIDE	HELIUM/IODINE	32.6	2.5×10^5	45	91	0.0012	45.0	0.51	(0.395)	(0.09)
—□—	AIR	NITROGEN/IODINE	1.0	1.5×10^5	59	96	0.0072	4.6	0.41	(0.21)	(0.17)



**RADIAL DISTRIBUTIONS OF SIMULATED-FUEL PARTIAL PRESSURE FOR
TWO BYPASS RATIOS WITH END-WALL ($r/r_1 = 0.5$) SIMULATED-FUEL INJECTION
IN 1.26-IN.-DIA VORTEX TUBE**

PERIPHERAL-WALL BUFFER-GAS INJECTION
ARGON BUFFER GAS
ARGON/BROMINE SIMULATED FUEL
SEE FIGS. 2(b) AND 6 FOR INJECTION CONFIGURATIONS
DASHED LINES INDICATE EXTRAPOLATION (SEE TEXT)
CONSTANT: $W_F = 0.9 \times 10^{-3}$ LB/SEC

SYMBOL	Re_j	Re_r	BYPASS RATIO, PERCENT	W_B/W_F	V_F/V_j	\bar{P}_F/P_I	\bar{P}_F/P_I MIX
—□—	1.4×10^5	118	44	5.0	0.61	(0.084)	(0.153)
—△—	1.5×10^5	86	69	5.6	0.52	(0.15)	(0.133)



RADIAL DISTRIBUTIONS OF SIMULATED-FUEL PARTIAL PRESSURE FOR SEVERAL BYPASS RATIOS WITH CENTERLINE SIMULATED-FUEL INJECTION IN 1.26-IN.-DIA VORTEX TUBE

PERIPHERAL-WALL BUFFER-GAS INJECTION

ARGON BUFFER GAS

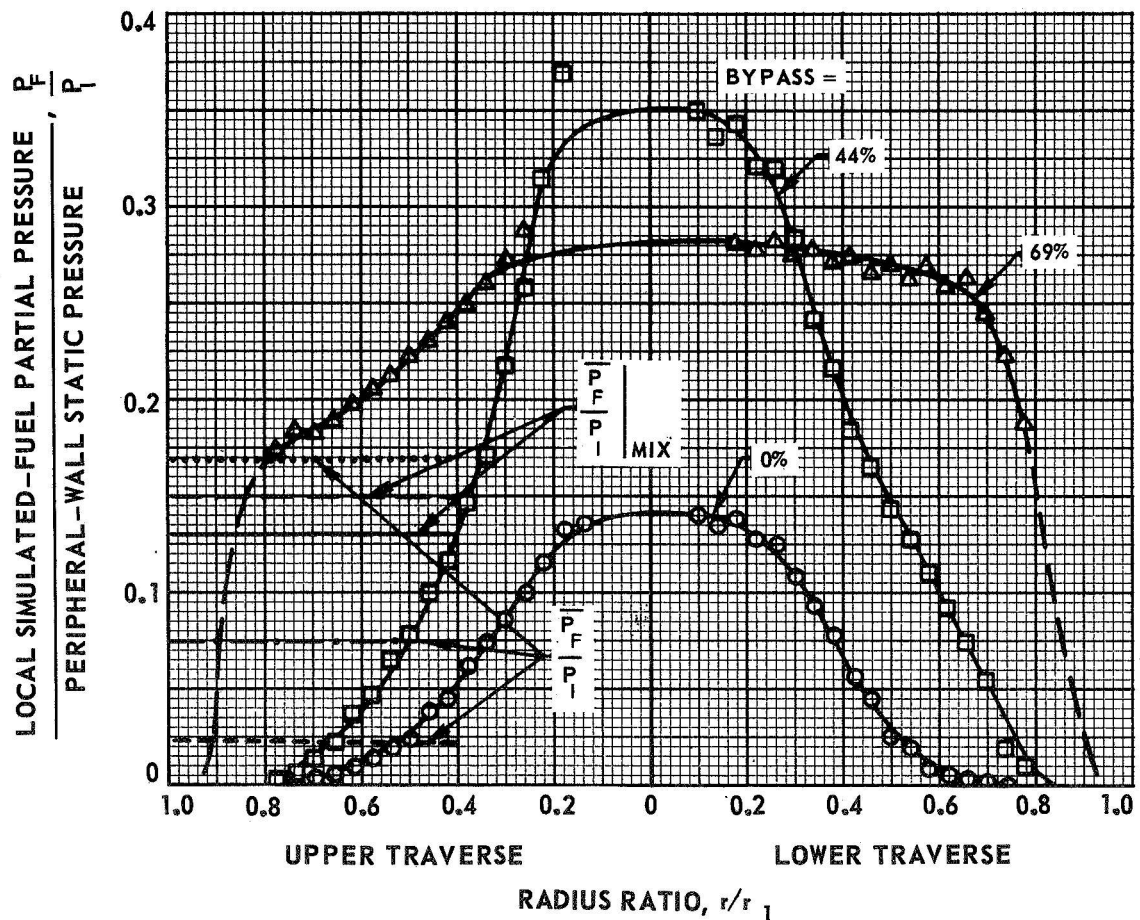
ARGON/BROMINE SIMULATED FUEL

SEE FIGS. 2(b) AND 6 FOR INJECTION CONFIGURATIONS

DASHED LINES INDICATE EXTRAPOLATION (SEE TEXT)

CONSTANT: $W_F = 1.0 \times 10^{-3}$ LB/SEC

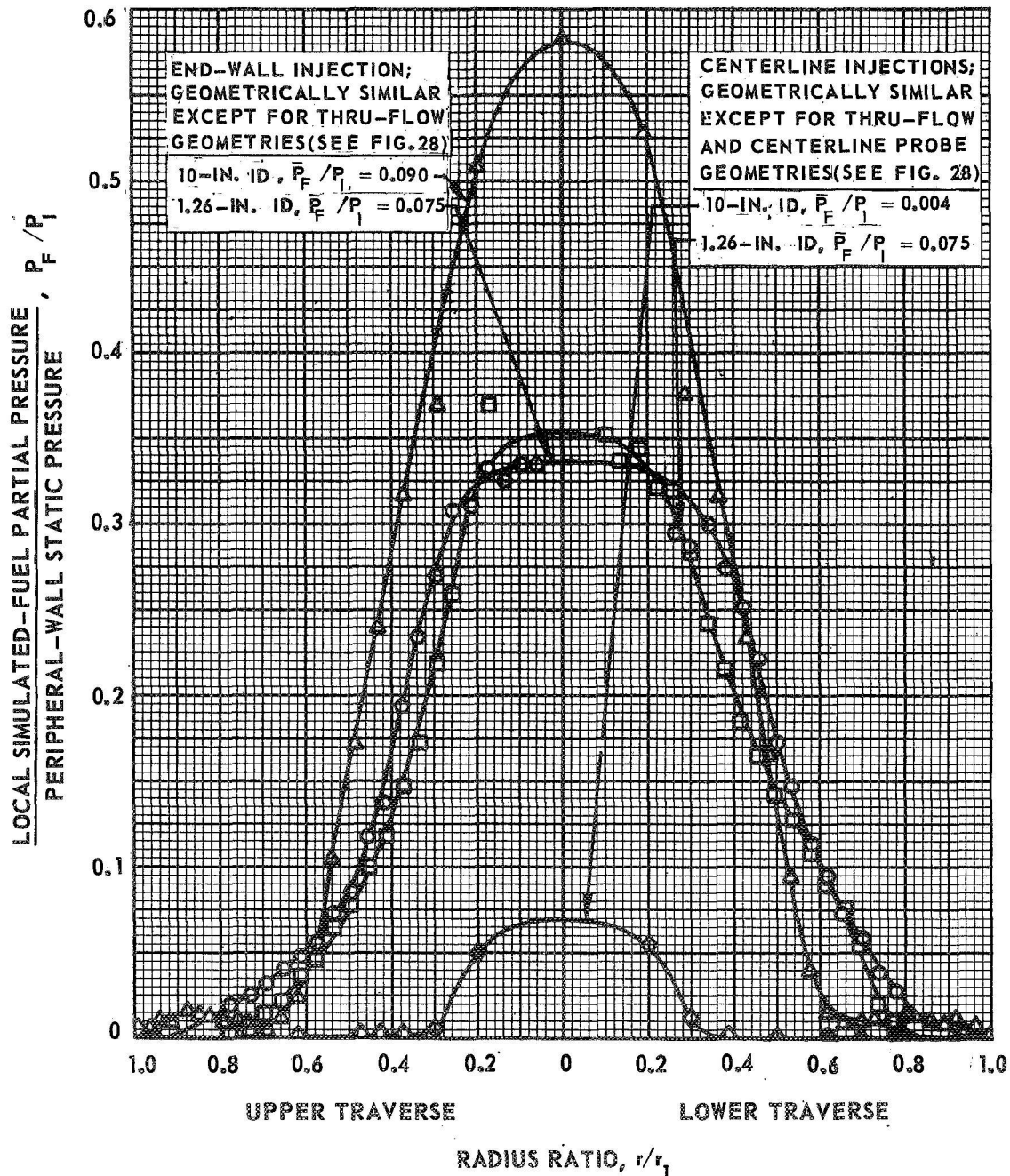
SYMBOL	Re_j	Re_r	BYPASS RATIO, PERCENT	W_B/W_F	V_F/V_j	\bar{P}_F/P_I	$\bar{P}_F/P_I \mid_{MIX}$
—○—	1.5×10^5	209	0	5.0	0.39	(0.023)	(0.13)
—□—	1.3×10^5	121	44	4.6	0.46	(0.075)	(0.15)
—△—	1.5×10^5	89	69	5.0	0.39	(0.17)	(0.13)



COMPARISON OF RADIAL DISTRIBUTIONS OF SIMULATED-FUEL PARTIAL PRESSURE FOR TWO VORTEX TUBE SIZES AND TWO SIMULATED-FUEL INJECTION CONFIGURATIONS

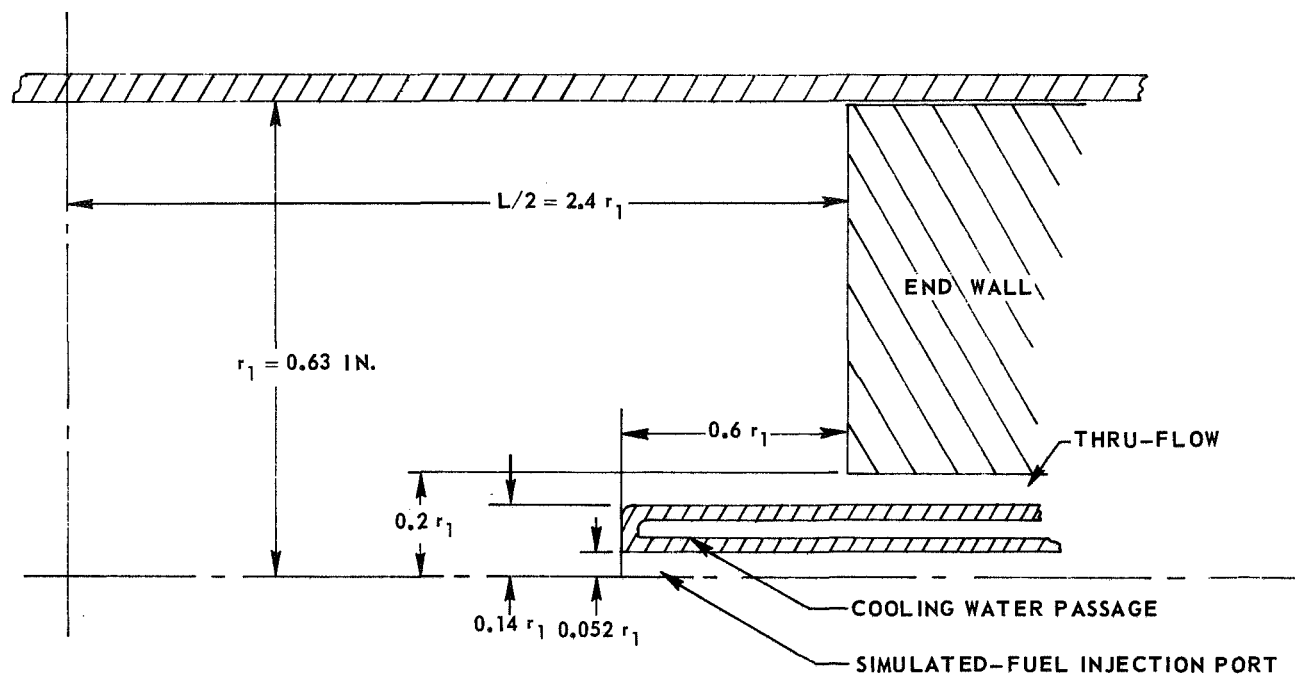
PERIPHERAL-WALL BUFFER GAS INJECTION

SYMBOL	VORTEX TUBE ID-IN.	SIMULATED-FUEL INJECTION	SIMULATED FUEL	Re_j	Re_f	BYPASS RATIO, PERCENT	W_F LB/SEC	W_B/W_F	V_F/V_J	\bar{P}_F/P_I	\bar{P}_F/P_I MIX
○	1.26	END-WALL $r/r_1 = 0.5$	ARGON/	1.3×10^5	118	44	0.9	5.0	0.61	0.084	0.15
□	1.26	CENTERLINE	BROMINE	1.3×10^5	121	44	1.0	4.6	0.46	0.075	0.15
△	10.0	END-WALL $r/r_1 = 0.5$	NITROGEN/	1.6×10^5	125	47	7.1	5.1	0.56	0.090	0.18
◇	10.0	CENTERLINE	IODINE	1.6×10^5	121	45	7.5	5.1	0.57	0.004	0.19

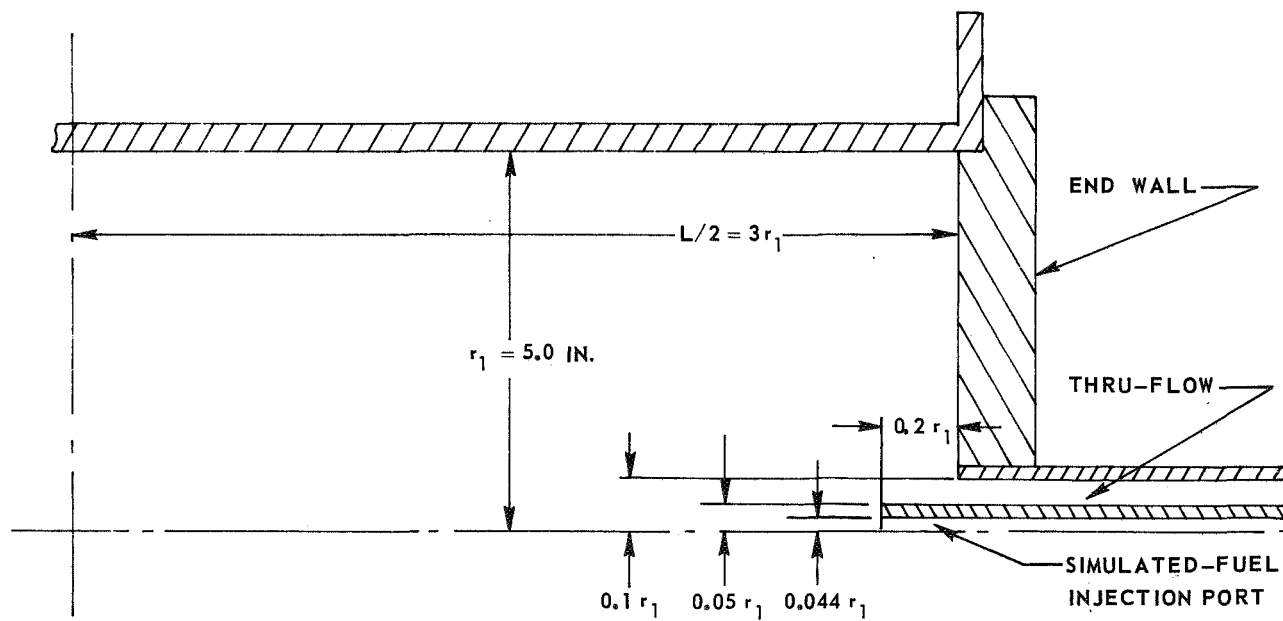


DIFFERENCES IN THRU-FLOW AND CENTERLINE PROBE GEOMETRIES BETWEEN 1.26-IN.-ID AND 10-IN.-ID VORTEX TUBES

(a) 1.26-IN.-ID TUBE



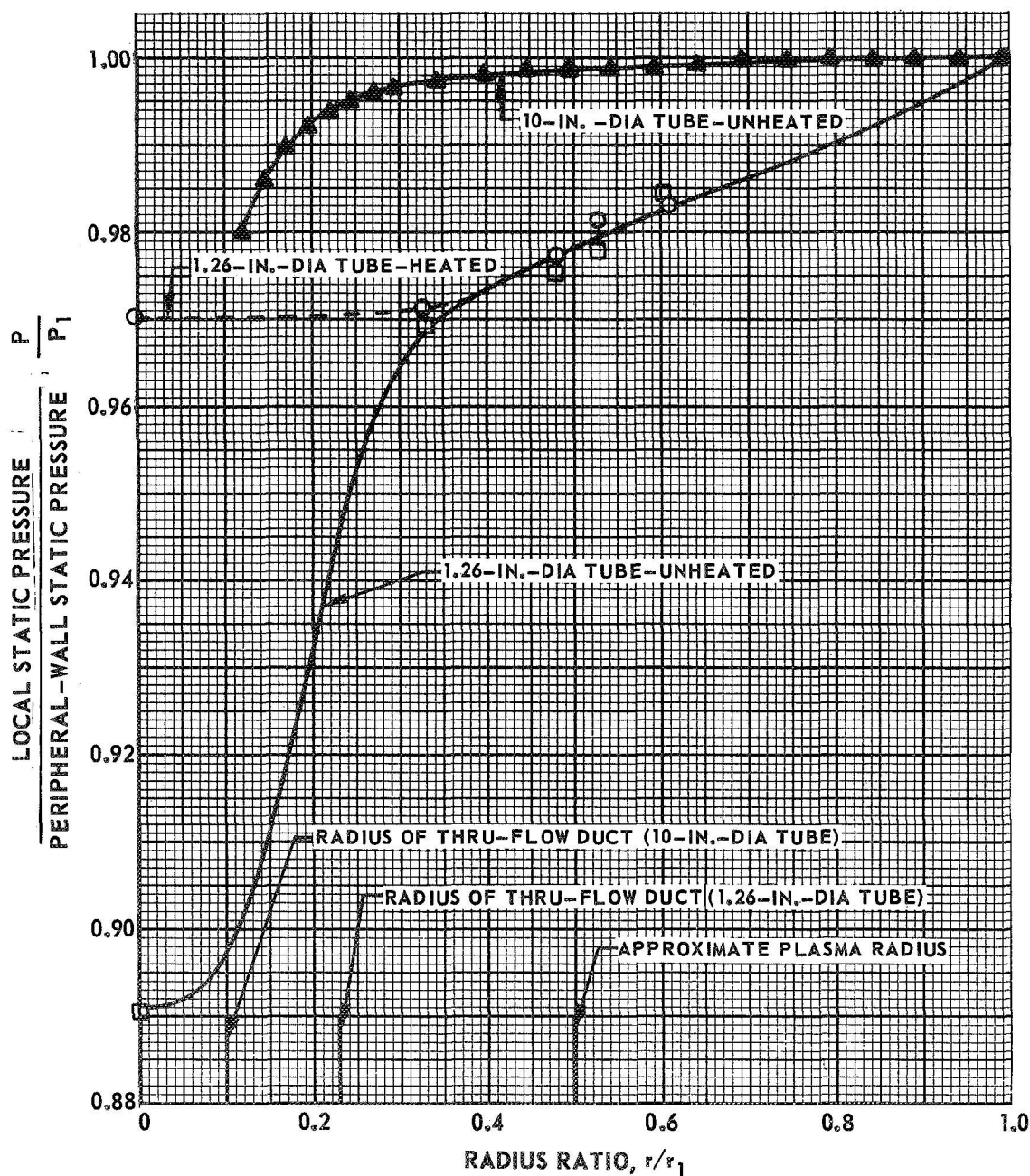
(b) 10-IN.-ID TUBE



EXPERIMENTALLY DETERMINED RADIAL STATIC-PRESSURE DISTRIBUTIONS IN HEATED AND UNHEATED VORTEXES

PERIPHERAL-WALL BUFFER GAS INJECTION

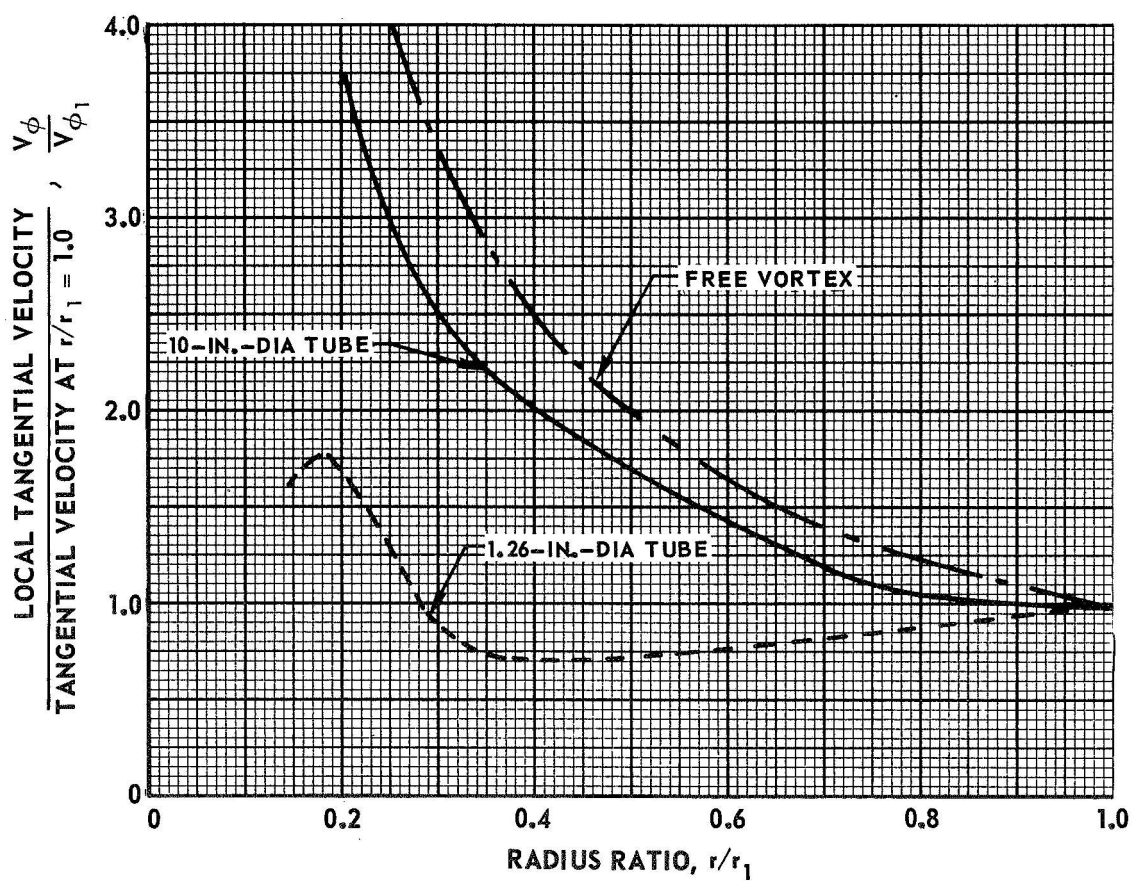
SYMBOL	VORTEX TUBE DIA	BUFFER GAS	P ₁
○ WITH HEAT ADDITION	1.26-IN.	ARGON	1 ATM
□ NO HEAT ADDITION	1.26-IN.	ARGON	1 ATM
▲ NO HEAT ADDITION	10-IN.	AIR	0.92 ATM



EXPERIMENTALLY DETERMINED TANGENTIAL VELOCITY DISTRIBUTIONS IN UNHEATED VORTEXES

PERIPHERAL-WALL BUFFER-GAS INJECTION
CALCULATED FROM PRESSURE DISTRIBUTIONS OF FIG. 29

SYMBOL	VORTEX TUBE DIA	BUFFER GAS	P ₁	V _{φ₁} FT/SEC	V _j FT/SEC
---- NO HEAT ADDITION	1.26-IN.	ARGON	1 ATM	170	280
— NO HEAT ADDITION	10-IN.	AIR	0.92 ATM	36	125



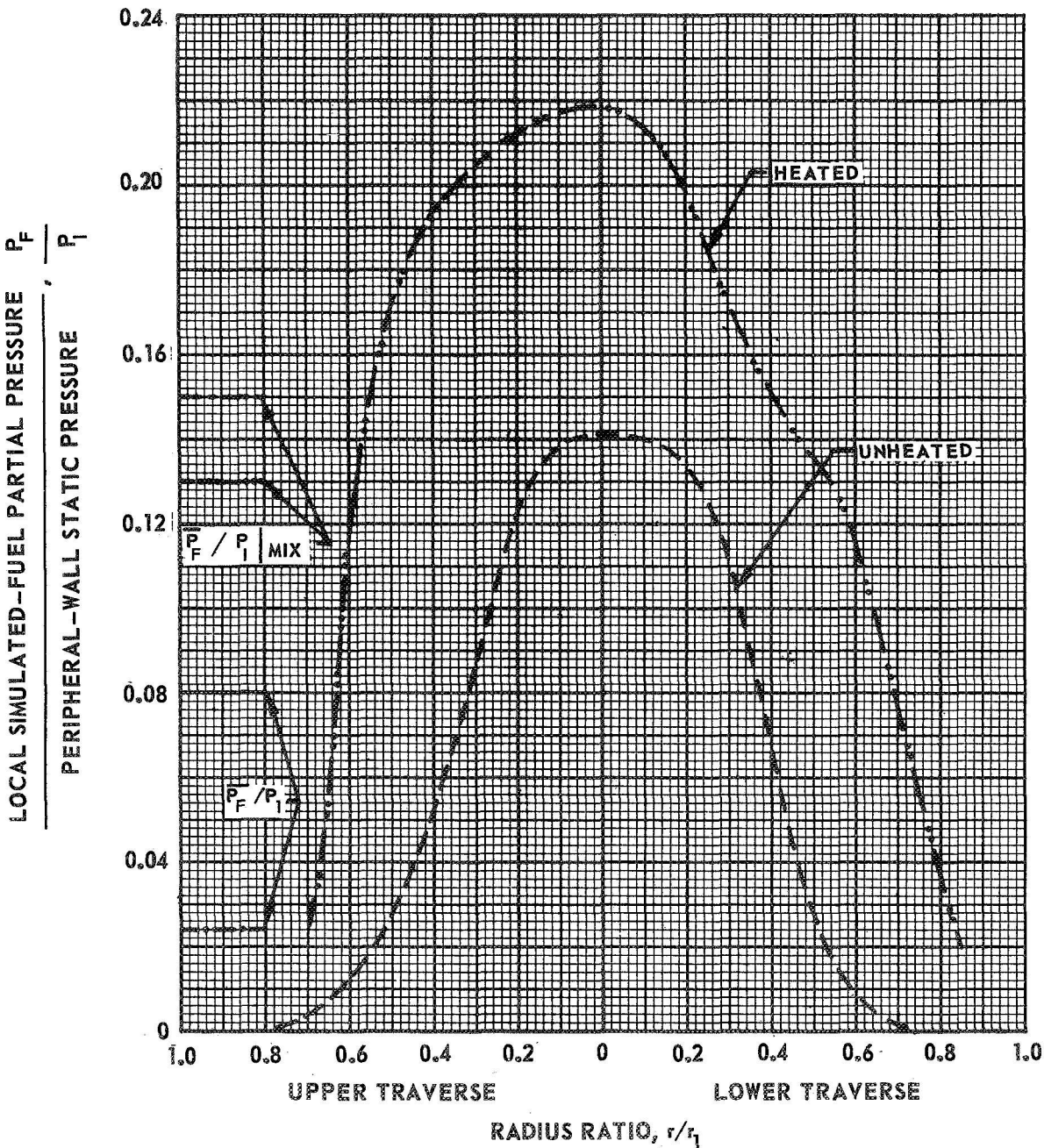
COMPARISON OF RADIAL DISTRIBUTIONS OF SIMULATED-FUEL PARTIAL PRESSURE
FOR HEATED AND UNHEATED VORTEX FLOWS IN 1.26-IN.-DIA VORTEX TUBE

PERIPHERAL-WALL BUFFER-GAS INJECTION
CENTERLINE SIMULATED-FUEL INJECTION

ARGON BUFFER GAS

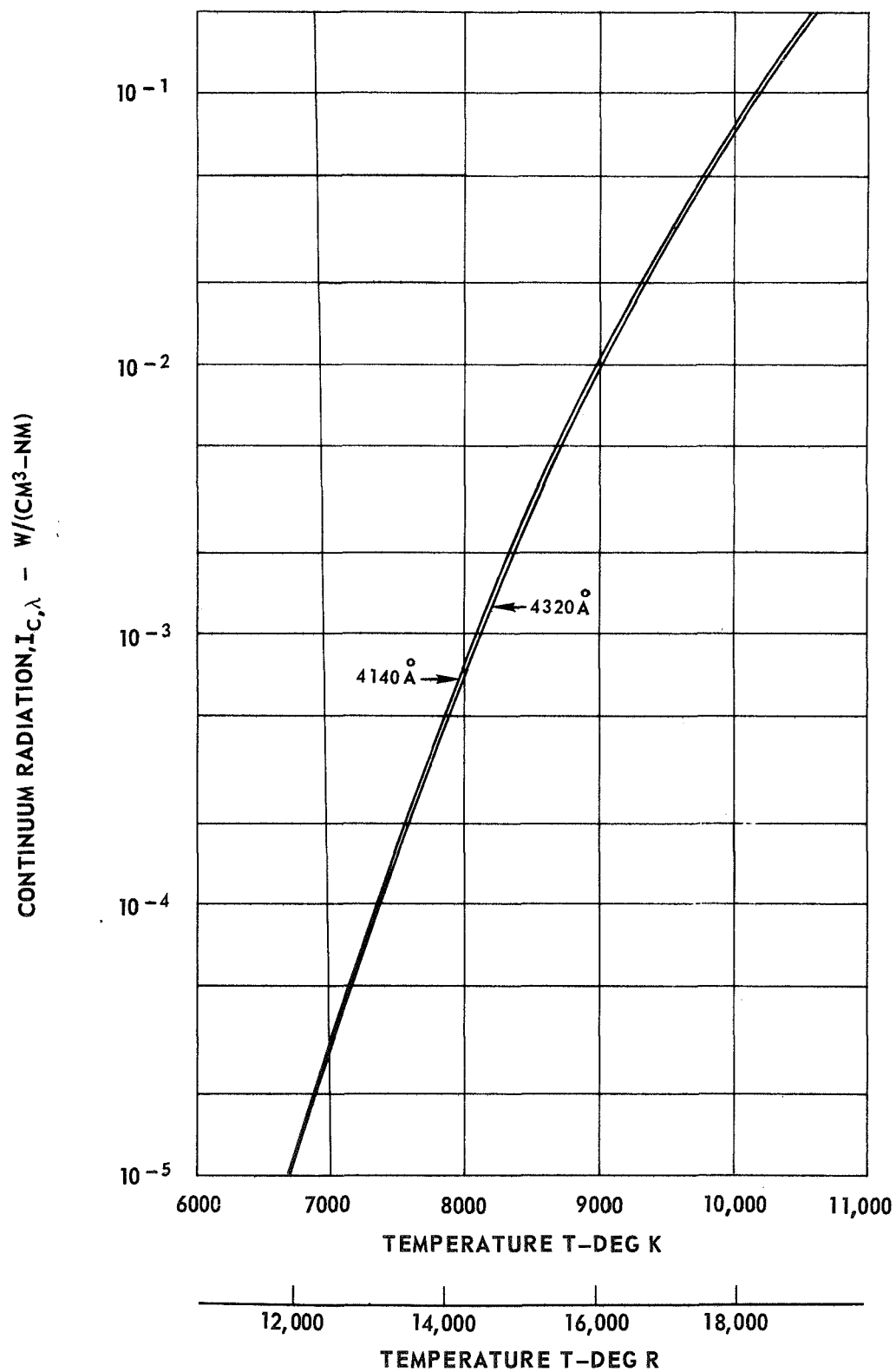
SEE FIG. 2 (b) FOR INJECTION CONFIGURATIONS

SYMBOL	VORTEX FLOW	W_F LB/SEC	SIMULATED FUEL	Re_j	W_B/W_F	$\overline{P_F}/P_1$	$\overline{P_F}/P_1$ MIX	Q_F/Q_B
---	UNHEATED	1.0×10^{-3}	ARGON/BROMINE	1.5×10^5	5.0	0.024	0.13	0.159
---	HEATED	2.2×10^{-3}	ARGON/XENON	1.3×10^5	2.0	0.08	0.15	0.153



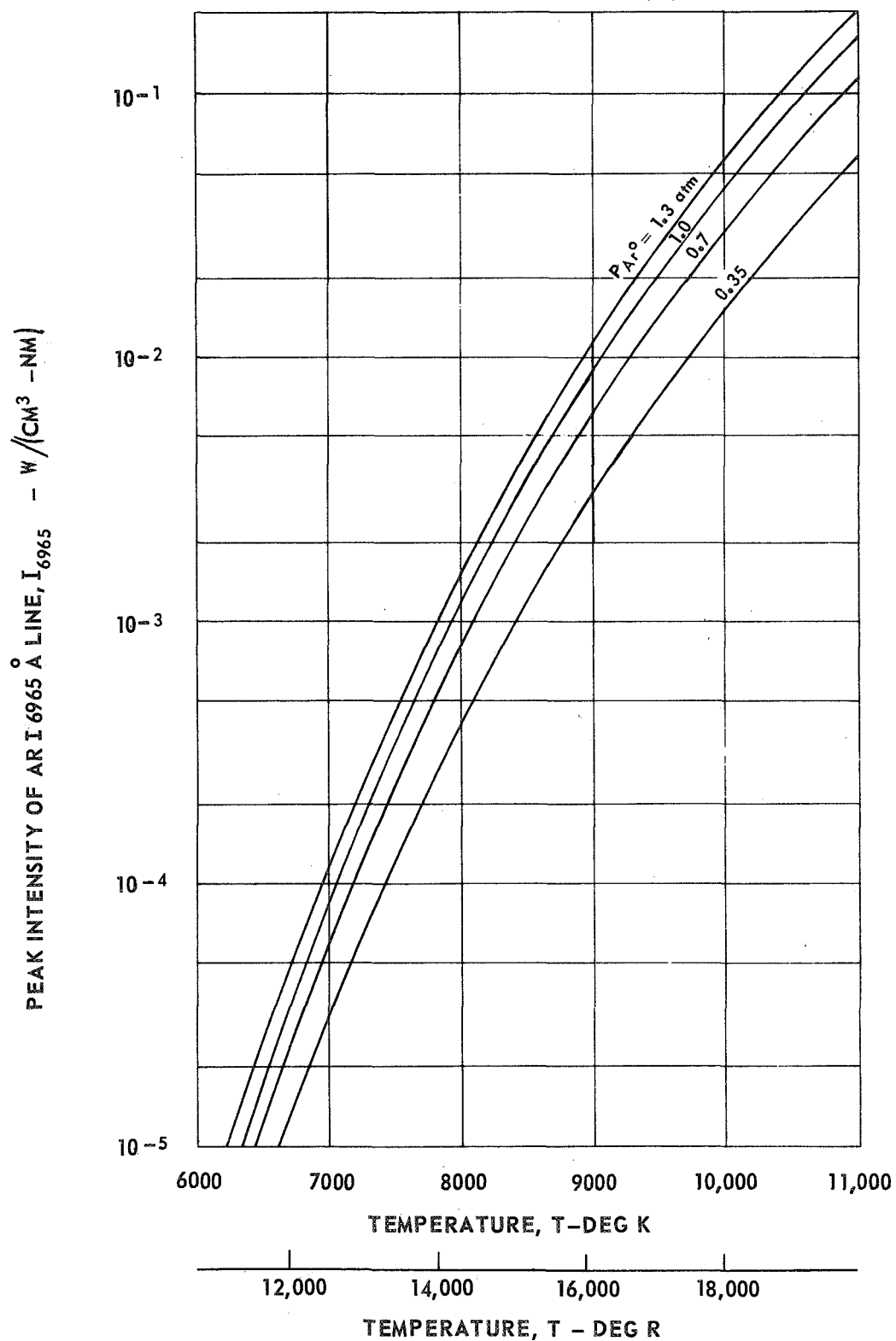
CALCULATED VARIATION WITH TEMPERATURE OF THE ARGON CONTINUUM RADIATION AT 4320 Å AND 4140 Å

TOTAL PRESSURE = 1.3 ATM
CALCULATED FROM EQUATION (A-2)



CALCULATED VARIATION WITH TEMPERATURE OF THE PEAK INTENSITY OF THE AR I 6965 Å LINE

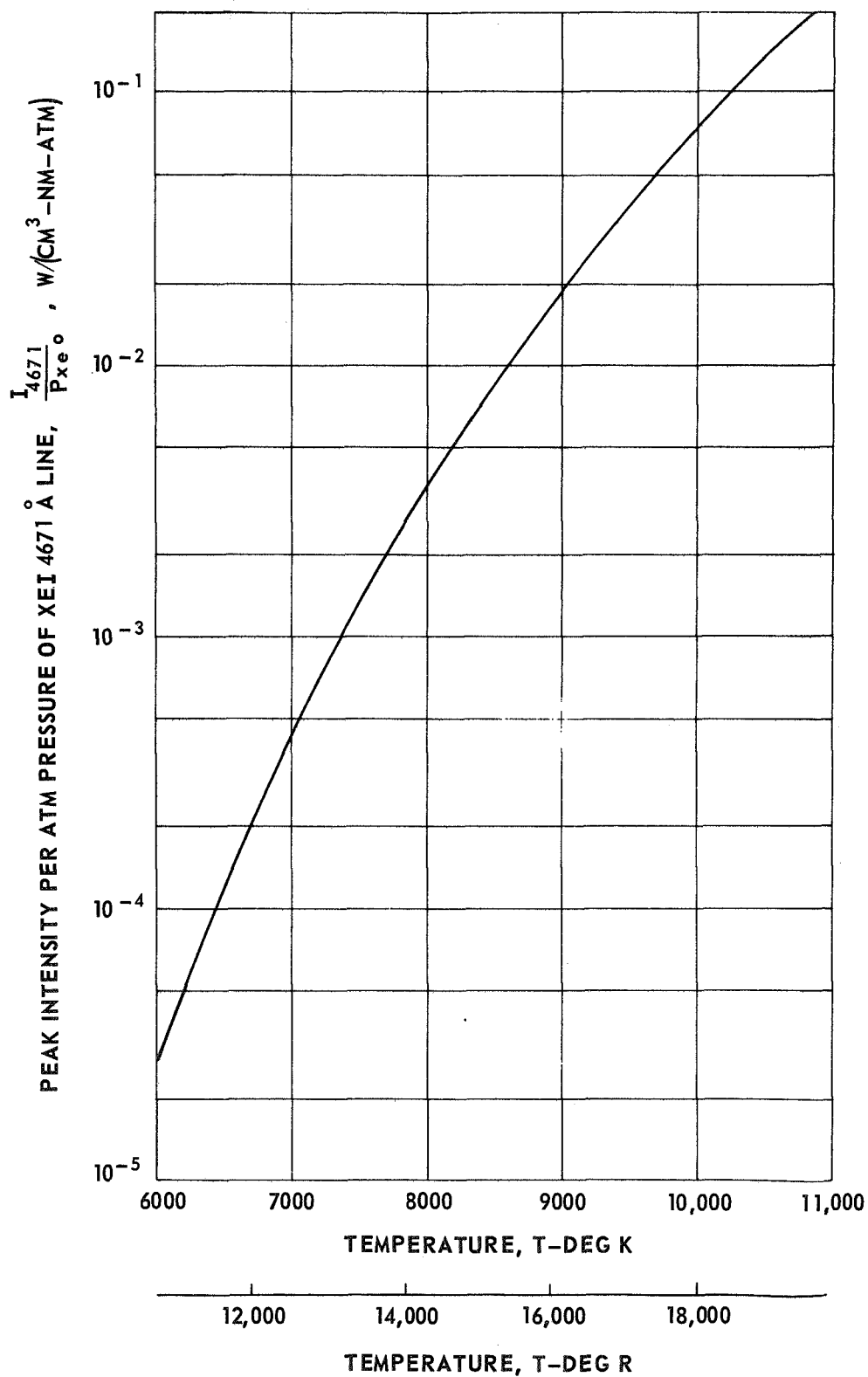
SEE TEXT FOR DEFINITION OF PEAK INTENSITY
CALCULATED FROM EQUATION A-3



CALCULATED VARIATION WITH TEMPERATURE OF THE PEAK INTENSITY PER ATMOSPHERE PRESSURE OF THE XE_I 4671 Å LINE

CALCULATED FROM EQ.(A-3) USING CONSTANT FROM FIG. 8(b)

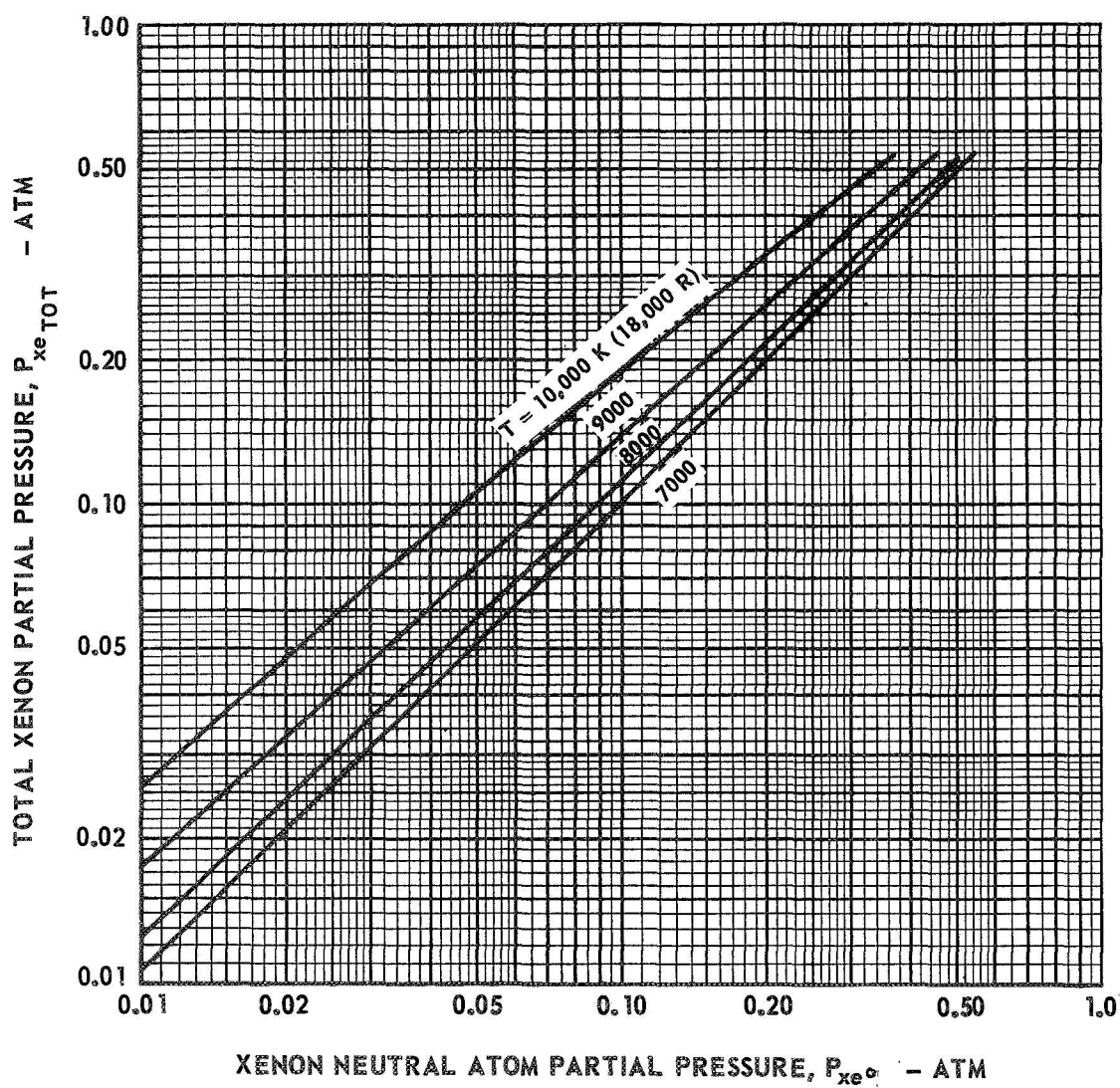
SEE TEXT FOR DEFINITION OF PEAK INTENSITY



VARIATION OF TOTAL XENON PARTIAL PRESSURE WITH
NEUTRAL XENON ATOM PARTIAL PRESSURE FOR AN
ARGON-XENON PLASMA AT A PRESSURE OF 1.3 ATM

CALCULATED USING METHOD OF REF. 10

$$P_{xe\text{ TOT}} = P_{xe0} + 2P_{xe+}$$



EFFECT OF STEP CHANGE IN SIMULATED-FUEL WEIGHT FLOW ON LOCAL PARTIAL PRESSURE RATIO
FOR A BYPASS RATIO OF 46 PERCENT IN A 10-IN.-DIA VORTEX TUBE

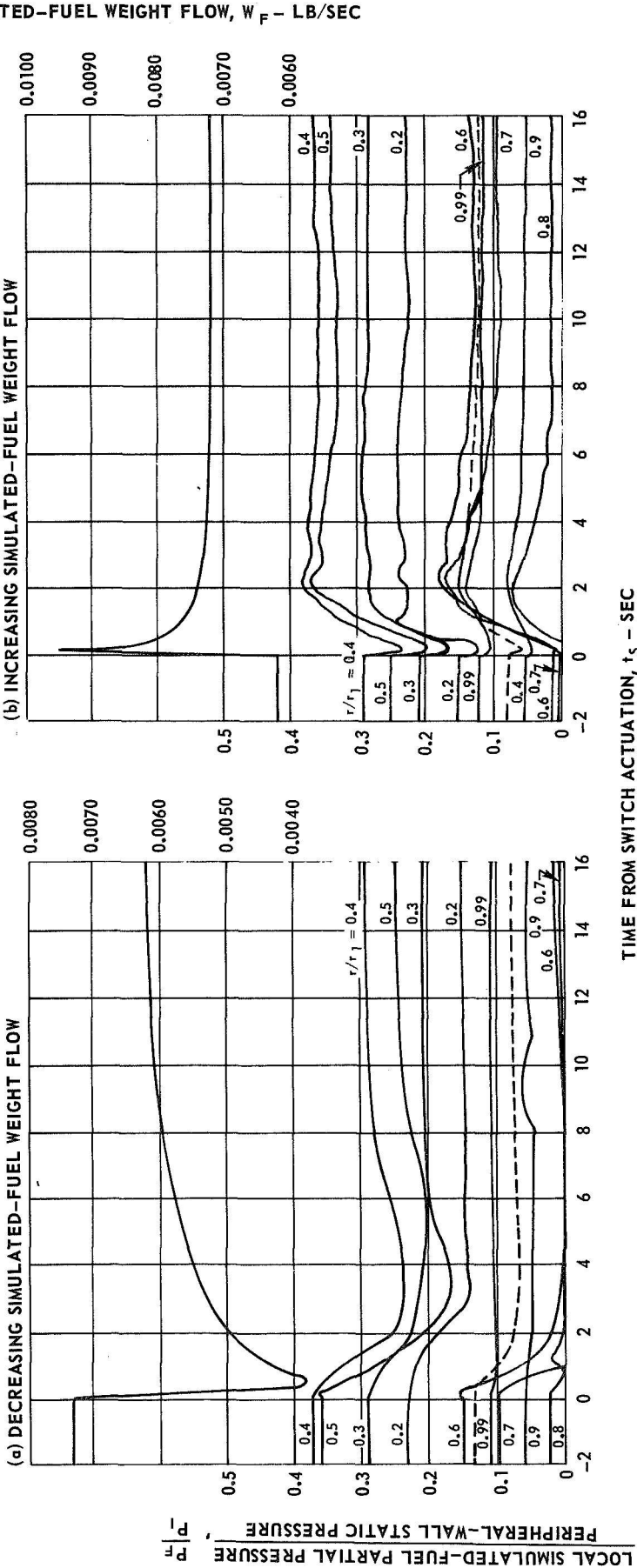
PERIPHERAL-WALL BUFFER-GAS INJECTION
END-WALL SIMULATED-FUEL INJECTION ($r/r_1 = 0.8$)

NITROGEN/IODINE SIMULATED FUEL

SEE TABLE VII FOR RANGE OF FLOW CONDITIONS

CONSTANTS: $Re_j = 1.6 \times 10^5$; $Re_r = 123$; $P_1 = 0.935$ ATM

DASHED LINE INDICATE VOLUME-AVERAGED PARTIAL PRESSURE RATIO - \bar{P}_F / P_1



EFFECT OF STEP CHANGE IN SIMULATED-FUEL WEIGHT FLOW ON CONTAINMENT FOR A BYPASS RATIO OF 0 PERCENT IN A 10-IN.-DIA VORTEX TUBE

PERIPHERAL-WALL BUFFER-GAS INJECTION

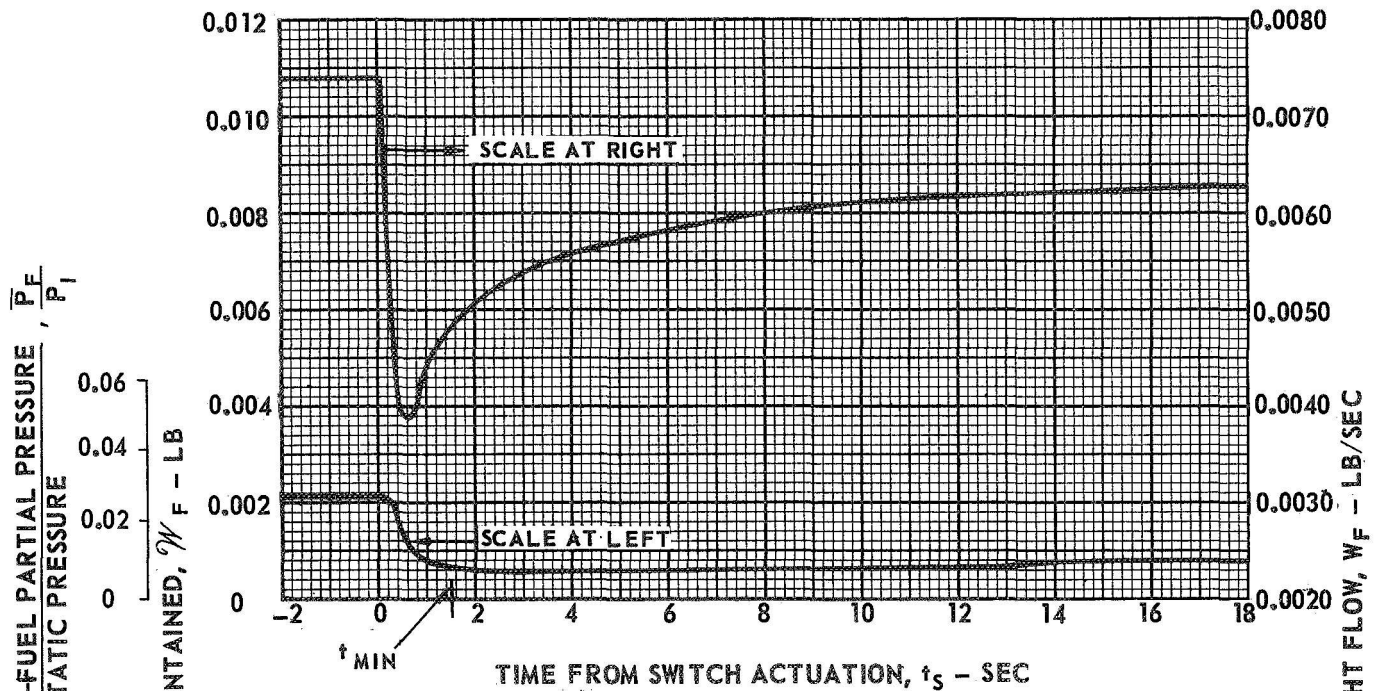
END-WALL SIMULATED FUEL INJECTION ($r/r_1 = 0.8$)

NITROGEN/IODINE SIMULATED FUEL

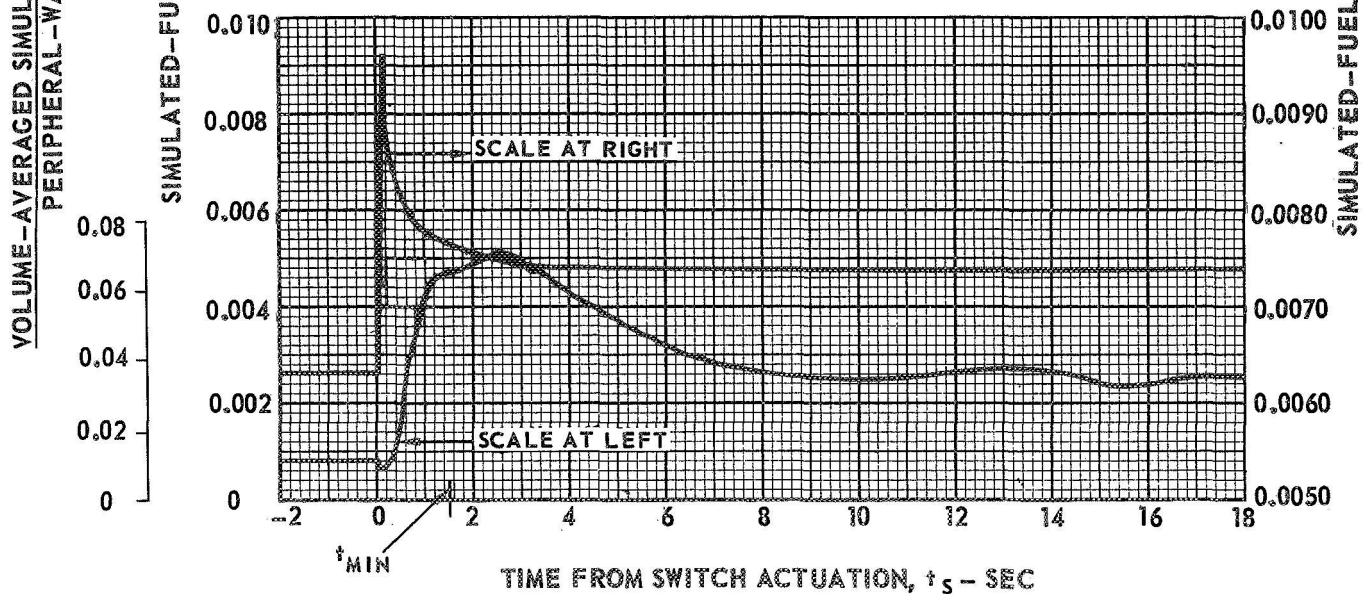
SEE TABLE VII FOR RANGE OF FLOW CONDITIONS

CONSTANTS: $Re_j = 1.6 \times 10$; $Re_r = 192$; $\beta_t = 25.3$; $P_1 = 0.923$ ATM

(a) DECREASING SIMULATED-FUEL WEIGHT FLOW



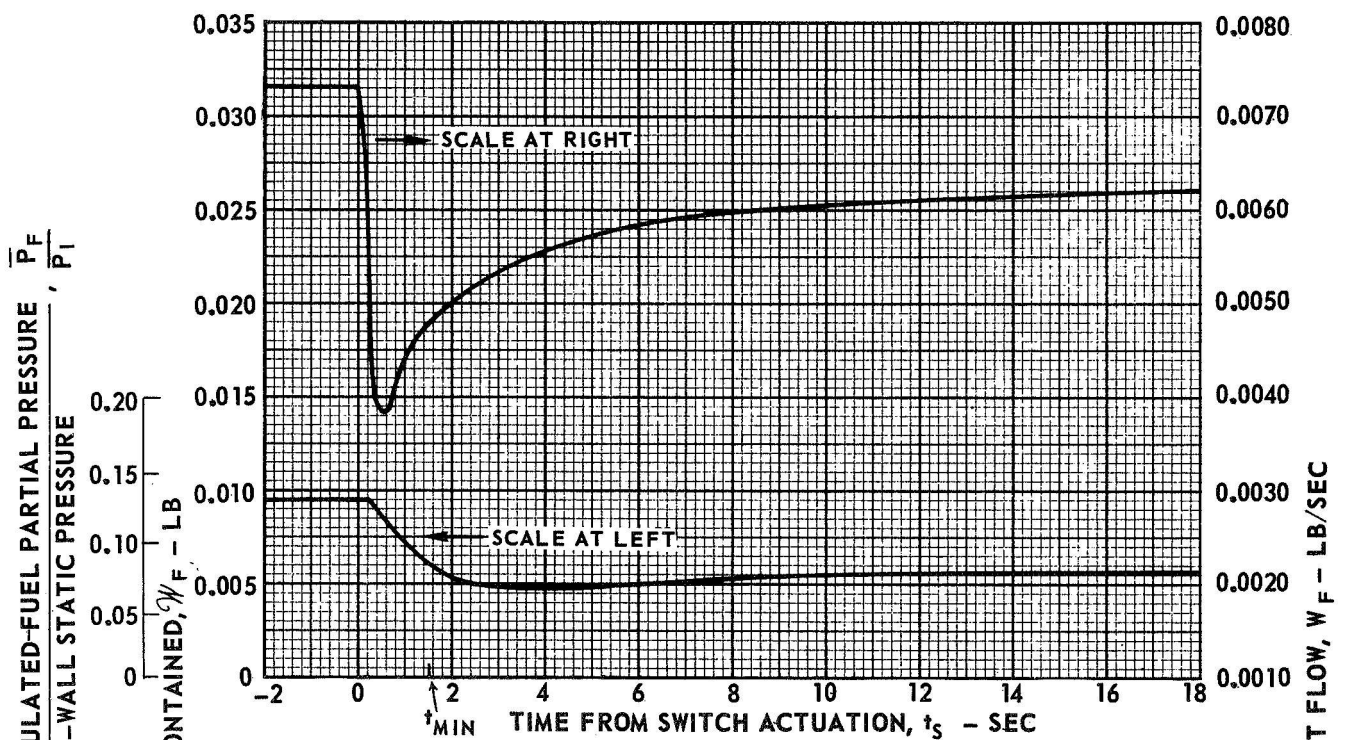
(b) INCREASING SIMULATED-FUEL WEIGHT FLOW



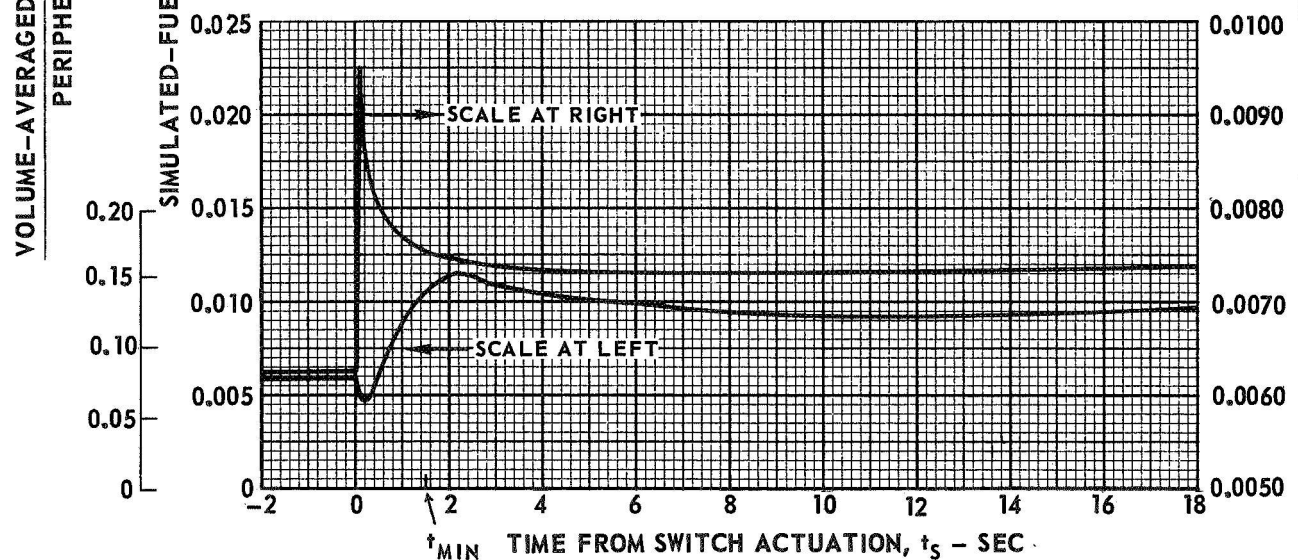
EFFECT OF STEP CHANGE IN SIMULATED-FUEL WEIGHT FLOW ON CONTAINMENT FOR A BYPASS RATIO OF 46 PERCENT IN A 10-IN.-DIA VORTEX TUBE

PERIPHERAL-WALL BUFFER-GAS INJECTION
END-WALL SIMULATED-FUEL INJECTION, ($r/r_1 = 0.8$)
NITROGEN/IODINE SIMULATED FUEL
SEE TABLE VII FOR RANGE OF FLOW CONDITIONS
CONSTANTS: $Re_J = 1.6 \times 10^5$; $Re_r = 123$
 $P_1 = 0.935$ ATM

(a) DECREASING SIMULATED-FUEL WEIGHT FLOW (FROM FIG. 36)



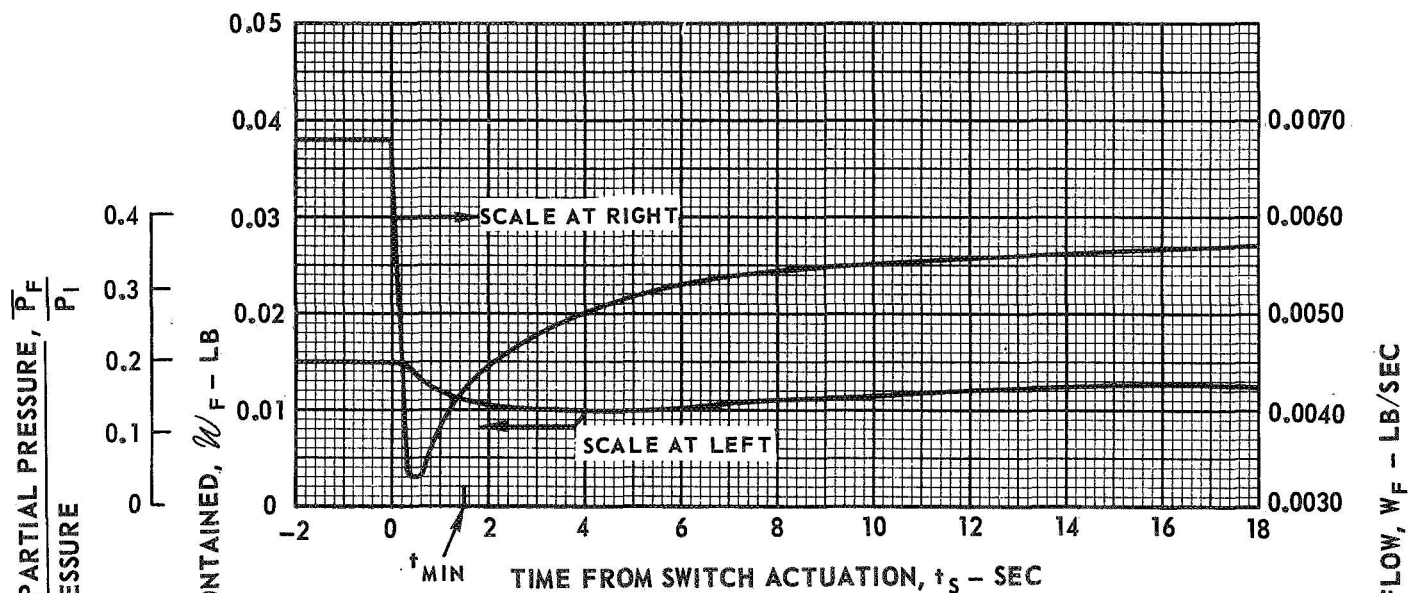
(b) INCREASING SIMULATED-FUEL WEIGHT FLOW (FROM FIG. 36)



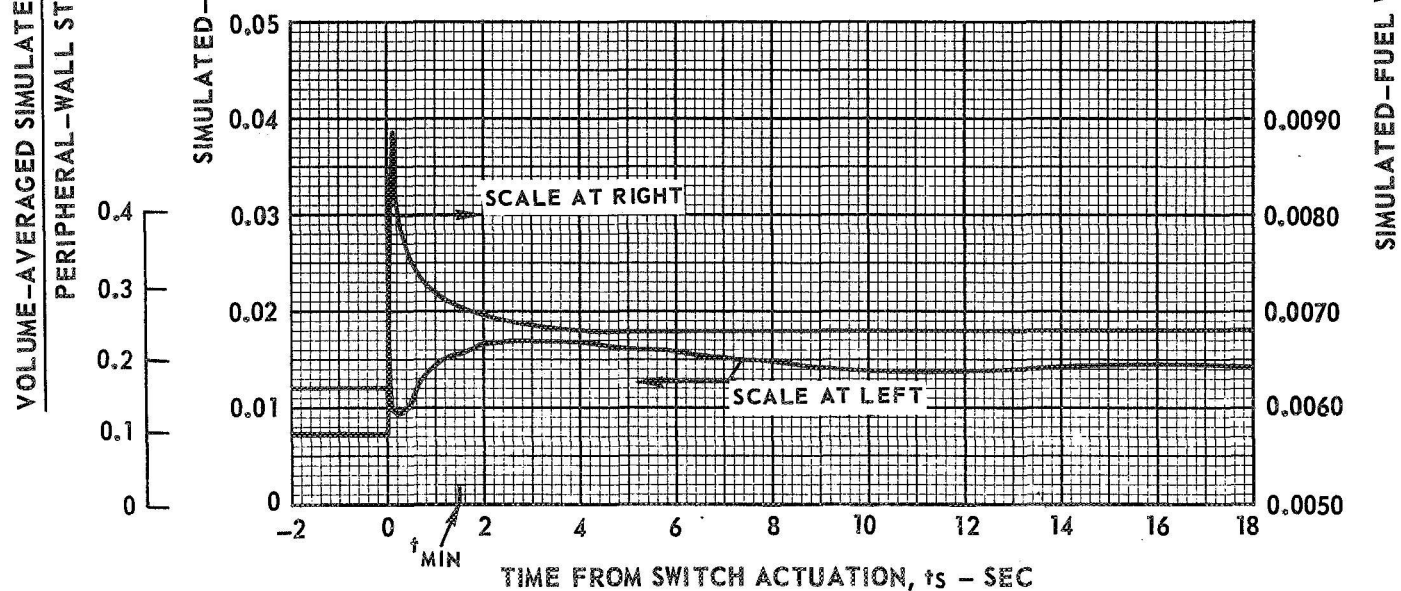
EFFECT OF STEP CHANGE IN SIMULATED-FUEL WEIGHT FLOW ON CONTAINMENT FOR A BYPASS RATIO OF 85 PERCENT IN A 10-IN.-DIA VORTEX TUBE

PERIPHERAL-WALL BUFFER-GAS INJECTION
 END-WALL SIMULATED-FUEL INJECTION ($r/r_1 = 0.8$)
 NITROGEN/IODINE SIMULATED FUEL
 SEE TABLE VII FOR RANGE OF FLOW CONDITIONS
 CONSTANTS: $Re_J = 1.6 \times 10^5$; $Re_r = 84$, $\beta_t = 58.8$
 $P_1 = 0.938 \text{ ATM}$

(a) DECREASING SIMULATED-FUEL WEIGHT FLOW



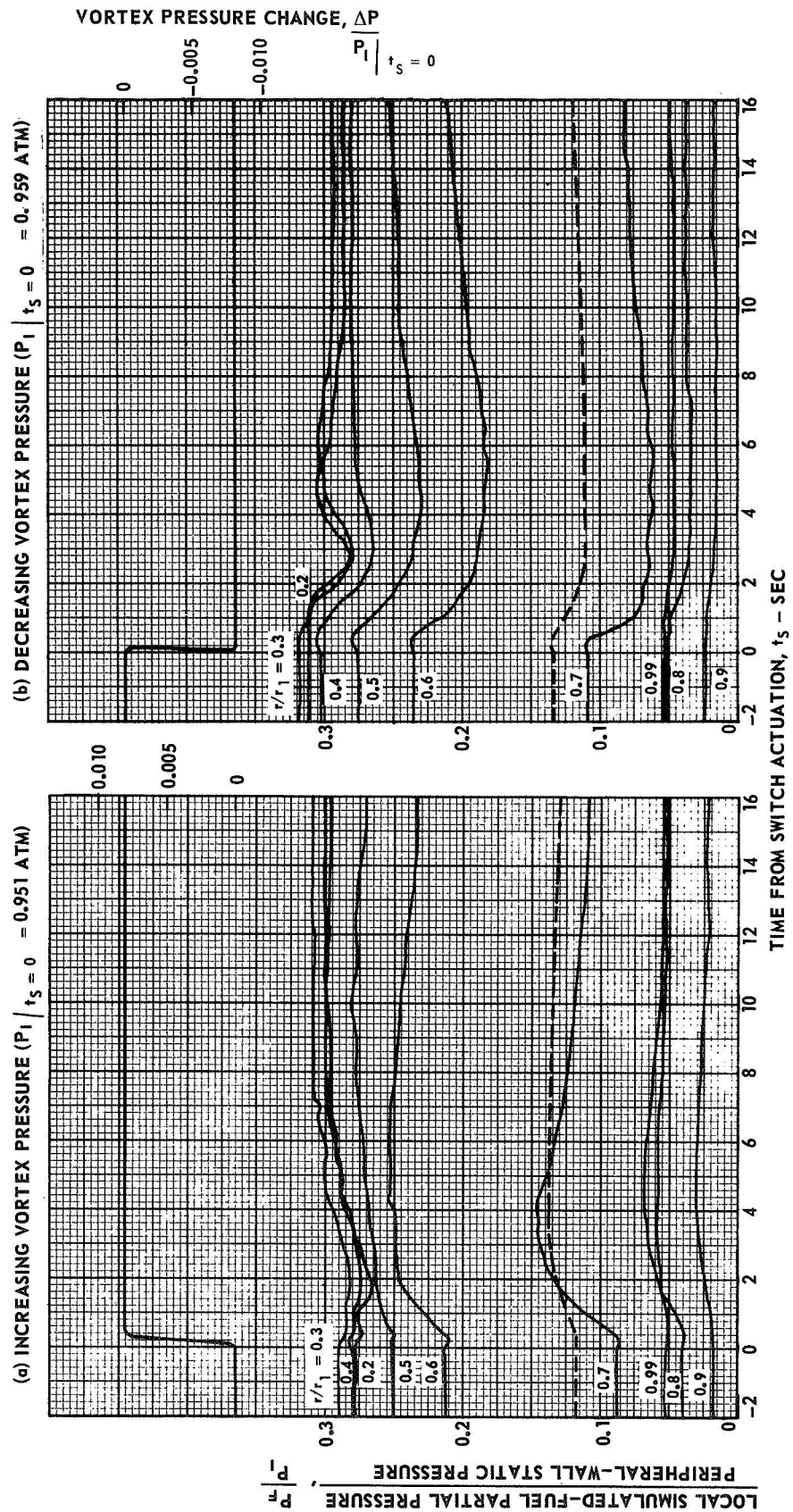
(b) INCREASING SIMULATED-FUEL WEIGHT FLOW



EFFECT OF STEP CHANGE IN VORTEX PRESSURE ON LOCAL PARTIAL PRESSURE RATIO FOR A BYPASS RATIO OF 46 PERCENT IN A 10-IN.-DIA VORTEX TUBE

PERIPHERAL-WALL BUFFER-GAS INJECTION
 END-WALL SIMULATED-FUEL INJECTION ($r/r_1 = 0.8$)
 NITROGEN/IODINE SIMULATED-FUEL
 SEE TABLE VII FOR RANGE OF FLOW CONDITIONS
 CONSTANT: $W_F = 7.4 \times 10^{-3}$ LB/SEC

DASHED LINES INDICATE VOLUME-AVERAGED PARTIAL PRESSURE RATIO - \bar{P}_F/P_1



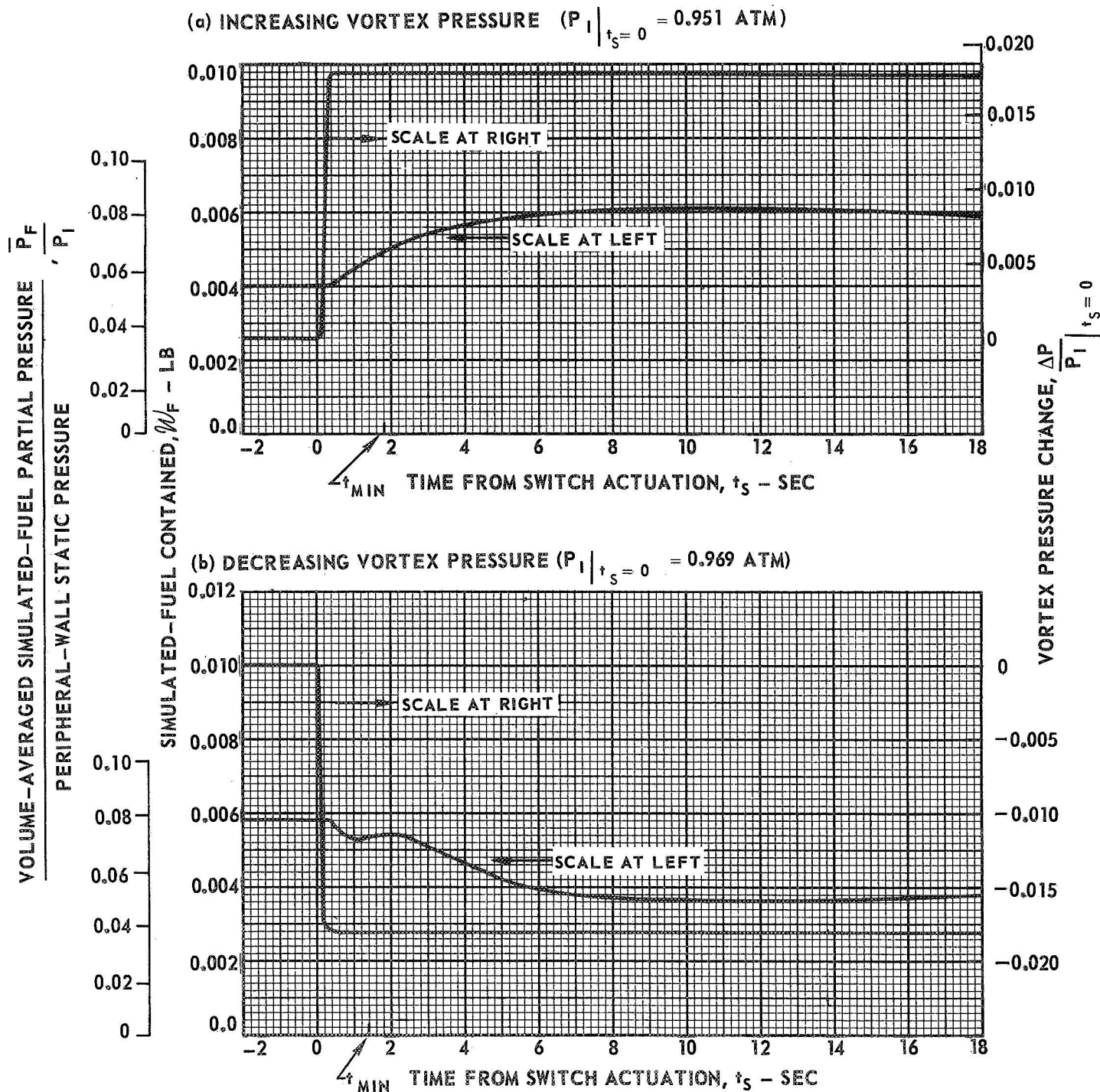
EFFECT OF STEP CHANGE IN VORTEX PRESSURE ON CONTAINMENT FOR A BYPASS RATIO OF 0 PERCENT IN A 10-IN.-DIA VORTEX TUBE

PERIPHERAL-WALL BUFFER-GAS INJECTION
END-WALL SIMULATED-FUEL INJECTION ($r/r_1 = 0.8$)

NITROGEN/IODINE SIMULATED FUEL

SEE TABLE VII FOR RANGE OF FLOW CONDITIONS

CONSTANT: $W_F = 8.0 \times 10^{-3}$ LB/SEC



EFFECT OF STEP CHANGE IN VORTEX PRESSURE ON CONTAINMENT FOR A BYPASS RATIO OF 46 PERCENT IN A 10-IN.-DIA VORTEX TUBE

PERIPHERAL-WALL BUFFER-GAS INJECTION

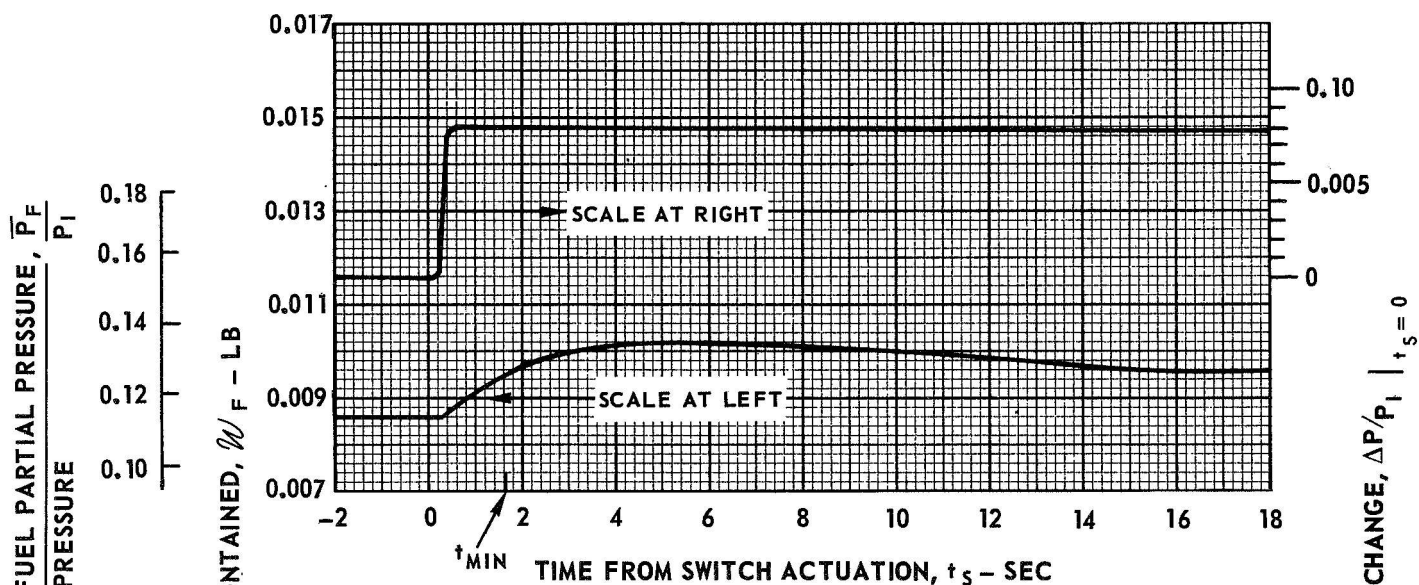
END-WALL SIMULATED-FUEL INJECTION ($r/r_1 = 0.8$)

NITROGEN/IODINE SIMULATED FUEL

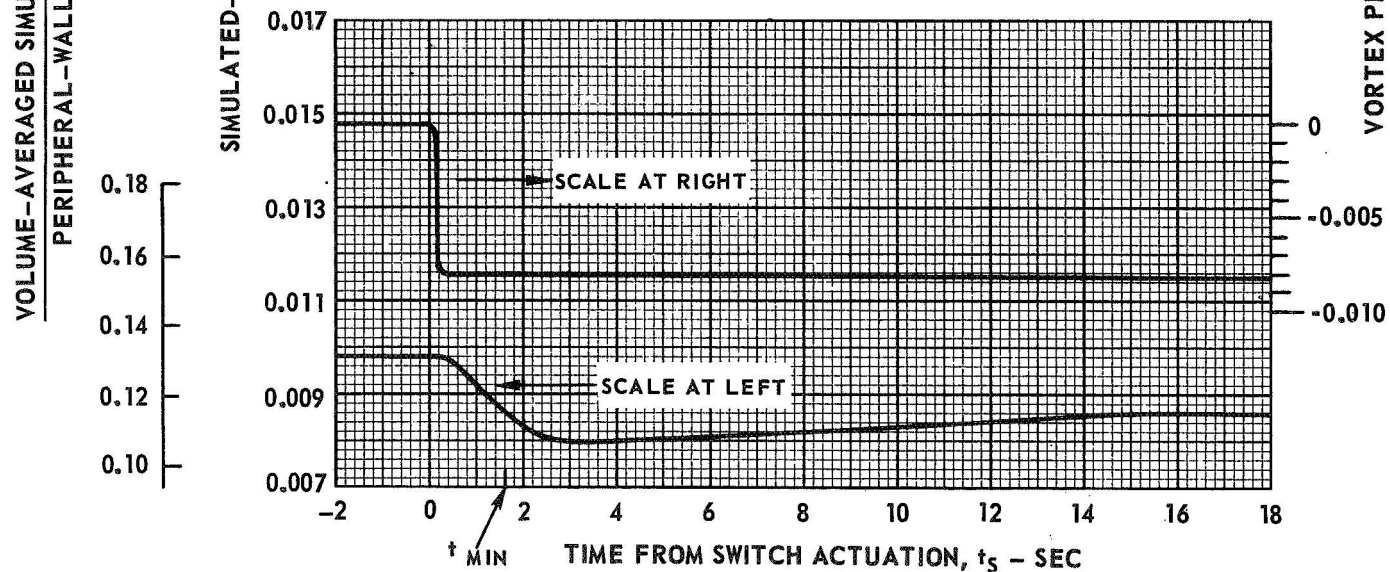
SEE TABLE VII FOR RANGE OF FLOW CONDITIONS

CONSTANT: $W_F = 7.4 \times 10^{-3}$ LB/SEC

(a) INCREASING VORTEX PRESSURE ($P_1|_{t_s=0} = 0.951$ ATM)
(FROM FIG. 40)



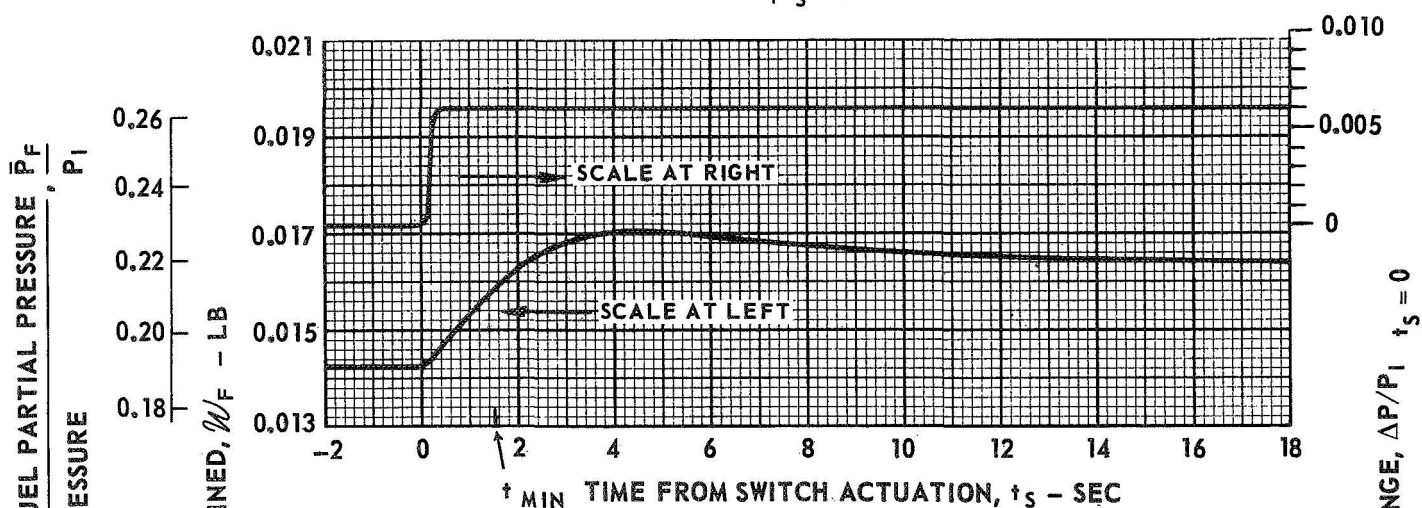
(b) DECREASING VORTEX PRESSURE ($P_1|_{t_s=0} = 0.959$ ATM)
(FROM FIG. 40)



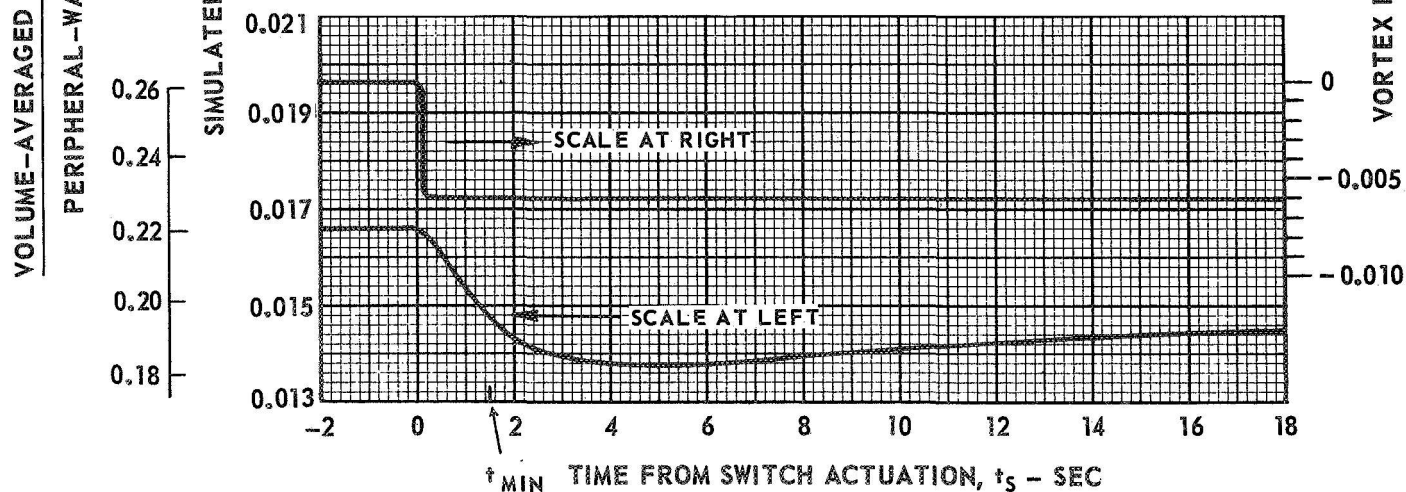
EFFECT OF STEP CHANGE IN VORTEX PRESSURE ON CONTAINMENT FOR A BYPASS RATIO OF 85 PERCENT IN A 10-IN.-DIA VORTEX TUBE

PERIPHERAL-WALL BUFFER-GAS INJECTION
 END-WALL SIMULATED FUEL INJECTION ($r/r_1 = 0.8$)
 NITROGEN/IODINE SIMULATED FUEL
 SEE TABLE VII FOR RANGE OF FLOW CONDITIONS
 CONSTANTS: $W_F = 6.8 \times 10^{-3}$ LB/SEC

(a) INCREASING VORTEX PRESSURE ($P_1|_{t_s=0} = 0.950$ ATM)

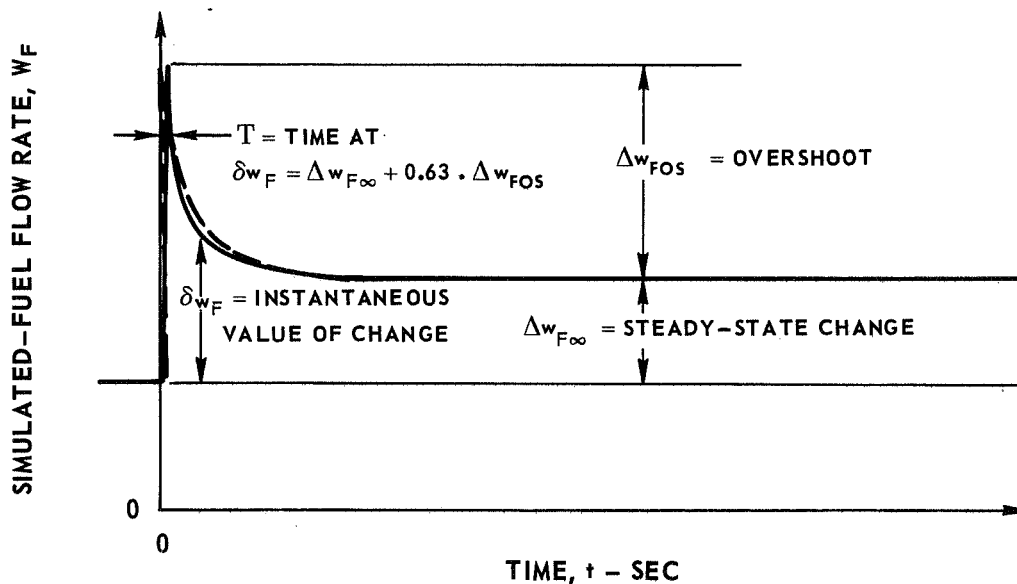


(b) DECREASING VORTEX PRESSURE ($P_1|_{t_s=0} = 0.956$ ATM)



NOMENCLATURE USED IN ANALYSIS OF VORTEX TRANSIENT RESPONSE DATA

———— DATA TRACE
 --- -- -- TRANSFER FUNCTION

(a) RESPONSE OF SIMULATED-FUEL FLOW RATE, δw_F (b) RESPONSE OF SIMULATED-FUEL CONTAINED, δw_F 